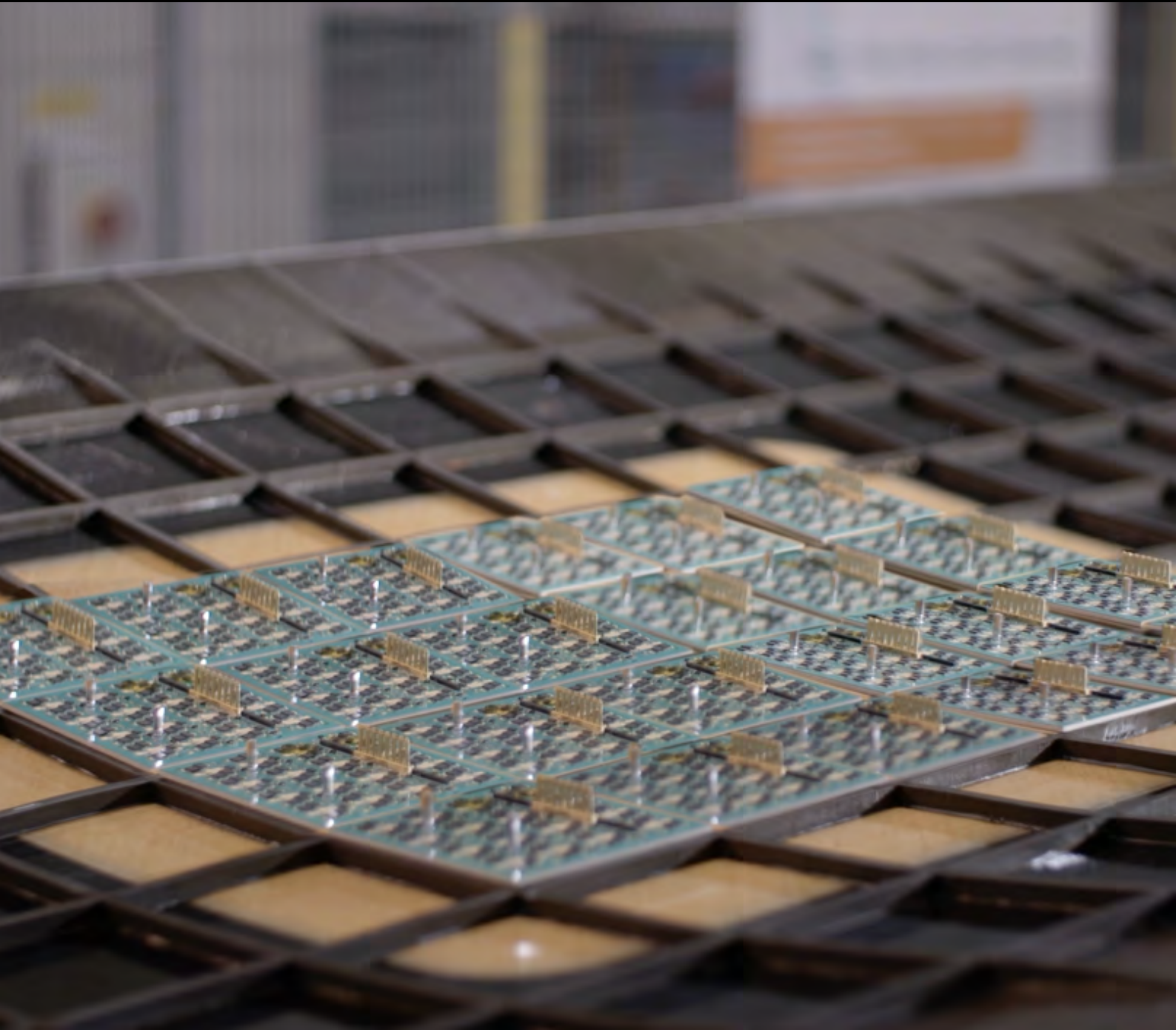


European Conference on Multifunctional Structures

EMuS 2020

17 - 18 November, 2020

Dr. Johan Kos, Prof. Xavier Martinez and Dr. Harmen Schippers



European Conference on Multifunctional Structures

EMuS 2020

17 - 18 November, 2020

congress.cimne.com/emus2020/

A publication of:

**International Centre for Numerical
Methods in Engineering (CIMNE)**

Barcelona, Spain



ISBN: 978-84-121101-6-6

Printed by: Artes Gráficas Torres S.L., Huelva 9, 08940 Cornellà de Llobregat,
Spain

TABLE OF CONTENTS

Preface	7
Supporting Organizations	9
Scientific Committee	11
Contents	13
Lectures	15
Authors Index	109

PREFACE

This E-book contains the papers accepted for presentation at the **European Conference on Multifunctional Structures (EMuS2020)**, an online event that took place from the **17th to the 18th of November 2020**.

The main aim of these Conferences on Multifunctional Structures is to share among the scientific and the industrial communities the recent advances made on mechanical structures with multiple functions. Recent advances in material technology have improved the additional capacities of such structures. It appears that the added functionalities can be as important as their mechanical performance.

Multifunctional structures integrate multiple functionalities in one single structure, thus achieving benefits compared to separated installation of these functionalities. Such benefits include reduced product weight or volume and more efficient manufacturing processes.

The large amount of possibilities offered by multifunctional structures make them very valuable in all engineering fields, being of special relevance to the transport sector, in all its forms: airplanes, spacecraft, automobiles, ships and yachts, etc.

The need for multifunctional structures has been addressed in the Strategic Research & Innovation Agenda of ACARE (the Advisory Council for Aeronautics Research in Europe) and in Horizon2020 programme of the European Commission, in particular, in the programme for Smart, Green and Integrated Transport. One of the goals set is that in 2050 technologies and procedures should be available that allow a **75% reduction in CO₂ emissions** per passenger kilometre and a **90% reduction in NO_x emissions**.

It is obvious that CO₂ and NO_x emissions of international air traffic must be reduced, so that aviation becomes more sustainable. This requires innovative technologies that reduce aircraft fuel consumption. This can be achieved:

- by improving the aerodynamic performance,
- by facilitating the introduction of fuel-efficient engines
- and by decreasing the weight of aircraft.

At the conference a wide range of papers were presented about multi-functional structural systems serving different purposes. The contributions dealt with the following topics:

- The Next Generation Multifunctional Fuselage Demonstrator – Leveraging Thermoplastics for Cleaner Skies
- New Multifunctional structures for Aerospace Applications
- New Lining Panel with Integrated Active Acoustic Control
- New Challenges: Integration of Antennas in Load-Bearing Aerostructures

Within these different topics, there were **4 keynote presentations**:

- “The Multifunctional Fuselage Demonstrator – An overview” by Mr. Ralf Herrmann (Airframe Research & Technology Typical Fuselage, Airbus, Germany).
- “Technological Aspects of Multi-Functional Structures for Orbital Space Applications” by Dr. Athanasios Dafnis (RWTH Aachen, Germany).

- "Symbiotic Mechatronics - The evolution of mechatronics in the context of digitalization on the way from components to integrated mechatronic systems" by Dr. Manfred Nader (Linz Center of Mechatronics, Austria).
- "Challenges of EM Simulation in Aeronautical Antenna Design" by Dr. Marta Martinez-Vazquez (Senior Antenna Engineer, IMST, Germany).

This E-book contains the latest research and development results made by scientists from multiple institutions and disciplines in the abovementioned fields, being of special relevance the contribution made by researchers working in the Horizon2020 ACASIAS project as well as in the CleanSky2 STUNNING consortium in the next generation Multifunctional Fuselage Demonstrator project. All papers in this E-book have been peer-reviewed by the members of the scientific committee.

To reduce **Energy consumption of aircraft and to reduce environmental impact of aviation** the Horizon2020 programme **Mobility for Growth** called in 2016 for proposals to develop and to demonstrate integrated aero-structures with self-sensing, morphing or multi-functional capabilities towards reduced weight and better aerodynamic performance as well as decreased manufacturing and operational cost.


As a result of this call several Horizon2020 projects were launched. One of these projects is the Horizon2020 ACASIAS project, with participation of 11 companies from 6 countries. ACASIAS develops novel concepts for aero-structures with integrated functionalities, such as aircraft structures with conformal integrated antennas for communication and fuselage linings with active acoustic damping to reduce engine noise inside the cabin.

The European Clean Sky research programme is developing innovative, cutting-edge technology aimed at reducing CO₂, gas emissions and noise levels produced by aircraft. One of the projects launched in this programme is the next generation Multifunctional Fuselage Demonstrator. This project aims to enable production rates of at least 60 large passenger aircraft per month, while reducing fuselage weight by 1 ton with a reduction of recurring costs. This in turn would bring significant fuel-burn reductions – and therefore reduction in the CO₂ and NO_x footprint. This will be achieved by the greater integration of fuselage, systems, cargo and cabin elements.

The EMuS2020 conference received co-funding from European Union's Horizon 2020 research and innovation programme under grant agreement No 723167 and from the Clean Sky 2 Joint Undertaking (JU) under grant agreement No 945583. The JU receives support from the European Union's Horizon 2020 research and innovation programme and the Clean Sky 2 JU members other than the Union.



Dr. Johan Kos
Principal R&D Engineer
Royal Netherlands Aerospace
Center (NLR)
Netherlands



Prof. Xavier Martinez
Scientist at CIMNE
Professor at Universitat
Politècnica de Catalunya (UPC)
Spain



Dr. Harmen Schippers
Senior Scientist
Royal Netherlands Aerospace
Center (NLR)
Netherlands

SUPPORTING ORGANIZATIONS



Advanced Concept for Aero-Structures with Integrated Antennas and Sensors (ACASIAS)



Next generation Multifunctional Fuselage Demonstrator in Clean Sky 2



International Center for Numerical Methods in Engineering (CIMNE)



Royal Netherlands Aerospace Centre (NLR)



L-UP



Funded by the Horizon 2020 Framework Programme of the European Union

Horizon 2020

SCIENTIFIC COMMITTEE

The Scientific Committee of the conference was constituted by:

- Dr. Stephan Algermissen, German Aerospace Center (DLR), Germany.
- Mr. Jens Bachmann, German Aerospace Center (DLR), Germany.
- Dr. Malte Misol, German Aerospace Center (DLR), Germany.
- Dr. Fermin Otero, CIMNE, Spain.
- Mr. Robert Sekora, Airbus Defence and Space, Germany.
- Prof. Constantinos Soutis, University of Manchester, United Kingdom.
- Dr. Jan-Joris van Es, Royal Netherlands Aerospace Centre NLR, Netherlands.
- Dr. Bas Veldman, Fokker Aerostructures, Netherlands.
- Mr. Jaco Verpoorte, Royal Netherlands Aerospace Centre NLR, Netherlands.

The Scientific Committee has conducted the peer review of the papers in this E-book.

CONTENTS

New Challenges: Integration of antennas in load-bearing aerostructures

GNSS Antenna Integrated Into a Classical Fibre Metal Laminate Fuselage Panel	17
<i>Y. Konter, C. Heuts, C. van Hengel and J. Verpoorte</i>	
RF Analyses of Integrated Ku-band Antenna	23
<i>J. Verpoorte, A. Hulzinga, M. Martínez-Vázquez, J. Leiss and M. Willemsen</i>	
Structural Analyses of GLARE-GFRP Transition for Integrated VHF Antenna on a Fuselage Panel	29
<i>F. Turon, F. Otero and X. Martinez</i>	
Structural Assessment of FML Aerostructures With Integrated Electromagnetic Features	35
<i>J. de Freitas, C. van Hengel and P. Homola</i>	
VHF Antenna Integrated Into a Classical Fibre Metal Laminate Fuselage Panel	43
<i>J. Lansink Rotgerink, C. Heuts, J. Verpoorte and C. van Hengel</i>	
VHF Communication Antenna Integrated Into an Aircraft Winglet	50
<i>M. Martínez-Vázquez, Z. Řezníček, S. Steeger, P. Vrchota and V. Lungaho</i>	

New lining panel with integrated active acoustic control

Experimental Analysis of the ACASIAS Active Lining Panel	56
<i>S. Algermissen and M. Misol</i>	
Noise Reduction Results of the ACASIAS Active Lining Panel	68
<i>M. Misol and S. Algermissen</i>	

New Multifunctional Structures for Aerospace Applications

A Technology to (Re-)Connection of Optical Fibres Embedded in Composite Structures	74
<i>J. Windels, J. Missinne, E. Voet, G. van Steenberg and G. Luyckx</i>	
System Development of Transmitting Conformal SATCOM Array Antenna Structures(CSAAS)	84
<i>M.-S. Kim and J.-W. Seo</i>	

The next generation Multifunctional Fuselage Demonstrator — leveraging thermoplastics for cleaner skies

Development of a Numerical Framework for Virtual Testing to Support Design of a Next Generation Thermoplastic Multifunctional Fuselage	90
<i>B.H.A.H. Tijs, K.S. van Dooren and C. Bisagni</i>	
Influence of the Angle Between Adherends on Ultrasonic Welding of Thermoplastic Composites	96
<i>C.B.G. Brito, J. Teuwen, C. Dransfeld and I. Fernandez Villegas</i>	
Multifunctional Fuselage Demonstrator: Thermoplastic Composite Skin Manufacturing Developments	102
<i>W.M. van den Brink, W.J. Vankan, J. de Kruijk, S.L. Veldman and R. Herrmann</i>	

LECTURES

GNSS ANTENNA INTEGRATED INTO A CLASSICAL FIBRE METAL LAMINATE FUSELAGE PANEL

EMuS 2020

Y. KONTER*, C. HEUTS[†], C. VAN HENGEL[‡], J. VERPOORTE*

* Royal Netherlands Aerospace Centre (NLR)
Voorsterweg 31, 8316 PR Marknesse, Netherlands
e-mail: Yuri.Konter@nlr.nl, web page: <https://www.nlr.nl>

[†] GKN Fokker Elmo
Aviollandalaan 33, 4631 RP, Netherlands
e-mail: Charly.Heuts@fokker.com, web page: <http://www.gknaerospace.com>

[‡] GKN Fokker Aerostructures
Industrieweg 4, 3351 LB Papendrecht, Netherlands
e-mail: Cees.vanHengel@fokker.com, web page: <http://www.gknaerospace.com>

Key words: Integrated Antenna, GLARE, GNSS double patch antenna

Abstract. Fibre Metal Laminate materials, like Glass Laminate Aluminum Reinforced Epoxy (GLARE), provide a unique opportunity to integrate patch antennas directly into the fuselage of aircraft. This integration will contribute to the reduction of carbon emissions of aircraft due to the reduction of aerodynamic drag. This paper discusses the integration of a double patch GNSS antenna directly into a classical Fiber Metal Laminate. A demonstrator of the antenna was manufactured and measured. The antenna has a flush finish on the outside of the fuselage. The preliminary results of these measurements show promising antenna performance, but more measurements are required to fully characterize this integrated antenna.

1 INTRODUCTION

The goal of the European Union Horizon2020 ACASIAS project is to reduce the environmental impact of aircraft by improving aerodynamics and reduction of the weight of the aircraft. The aerodynamic drag and the weight of the aircraft are being reduced by integrating antennas and sensors in the structure of the aircraft. Conventional antennas are installed as protruding elements on the exterior of fuselages. These protruding elements increase the aerodynamic drag of an aircraft. Fibre Metal Laminate materials (FML) provide an opportunity to realize integrated antenna designs that can eliminate the requirement for protruding antennas.

This paper will address the integration of a Global Navigation Satellite System (GNSS) antenna in the FML skin of the aircraft. GNSS radiation in the L1 and L5 bands is realized using two concentric circular radiating patches. Good axial ratio is achieved by feeding the patches with four probes [1]. The four probes are combined on the inside of the fuselage using a hybrid coupler printed circuit board. The resulting integrated antenna element is flush on the outside of the fuselage.

A demonstrator of the FML panel with integrated GNSS antenna has been made and measured. These measures will be discussed. Simulation and measurement results of the integrated GNSS antenna will be discussed.

2 DESIGN OF THE DOUBLE BAND INTEGRATED GNSS ANTENNA

The integrated GNSS antenna is created by modifying a standard GLARE panel in order to accommodate the electrical elements required by the antenna. The Fibre Metal Laminate (FML) GLARE is build-up of 0.3 mm thick aluminium and 0.13 mm thick glass-fibre layers. The integrated GNSS antenna is designed using the same GLARE materials. This allows the antenna patches to align with the GLARE aluminium panels.

The antenna is designed as a stacked patch antenna using circular conducting patches as radiating elements. Two patches are used which are tuned to radiate in the L1 and L5 GNSS bands. The patches are stacked concentrically as shown in Figure 1 A. The L5 patch is made of aluminium, similar to remaining GLARE panel. The smaller L1 patch is made of copper in order to allow galvanic connection of feeds to the patch.

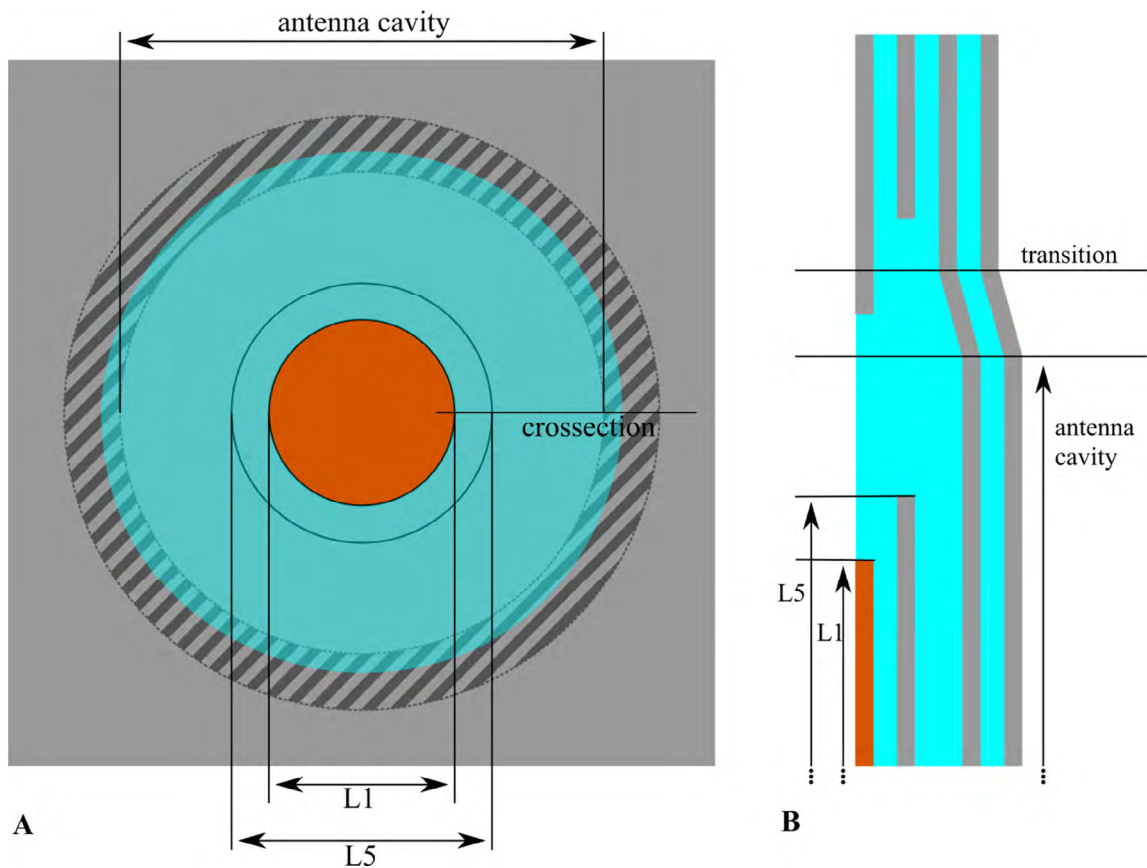
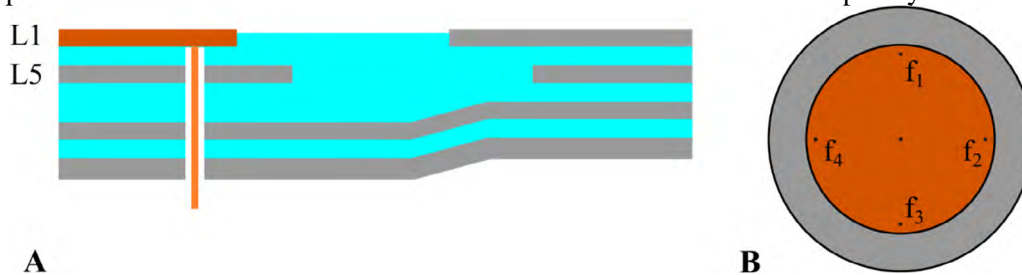


Figure 1: Schematic of the integrated GNSS design. **A** shows the top view of the GNSS antenna. The two circular antenna patches L1 (orange) and L5 (grey) and the resin window (blue). The transition from the antenna cavity into regular GLARE is shown by the hatched area. **B** shows a cross-section of the FML panel, indicating how the layers of material are stacked to create the cavity for the GNSS antenna.

The antenna ground-plane is realized as a circular dent in the inner aluminium layer. A transition area is introduced (Figure 1 B) in order to fully integrate the antenna in a regular GLARE panel.

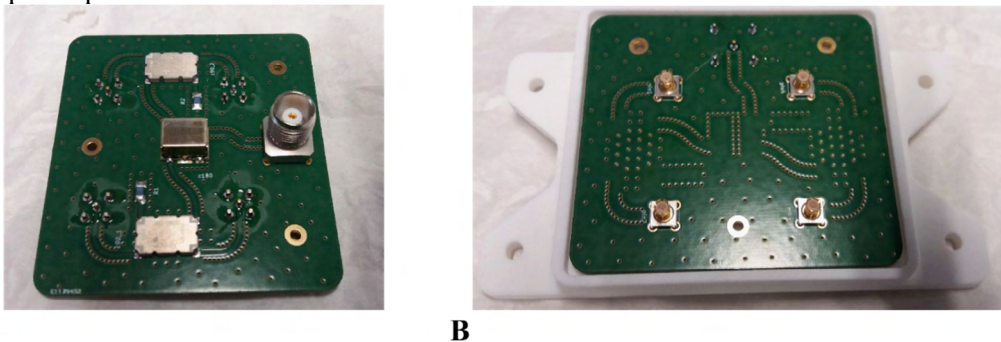
2.1 Antenna Feed

The L1 patch of the dual band antenna is fed with four probes. This feed method, combined with the circular radiating patches, has been shown to give good axial ratio performance for a wide frequency-band [1]. The location of the feeds is shown in Figure 2 B. The L5 patch is capacitively coupled to the L1 patch, therefore a hole is drilled to avoid a galvanic connection between the feed probes and the L5 circular patch. The feeds are positioned such that the input impedance of the feeds is closest to 50Ω for both the L1 and the L5 frequency bands.



A **B**
Figure 2: Schematic showing how the integrated antenna is fed. **A** shows how the probe is connected to the L1 patch. A hole is drilled through the remaining laminate in order to avoid galvanic contact of the feed with the aluminium layers. **B** shows the location of the four feeds on the double patch antenna.

RHCP radiation is achieved by feeding the four probes $f_{1...4}$ with a relative phase difference of $0, 90, 180$ and 270° respectively. These phase differences are achieved using a feed network connected on the inside of the fuselage. The feed network is designed on a PCB shown in Figure 3. The feed network combines a 180° hybrid coupler with two 90° hybrid couplers to achieve the required phase differences.



A **B**
Figure 3: PCB with feed network to achieve phase difference for the four probes. **A** shows the three surface mount devices used to achieve the phase differences. It also shows the single output connector for the antenna signal. **B** shows the four connectors used to attach the PCB to the inside of the fuselage.

Finally, a grounded via is added in the centre of circles to prevent the build-up of static charge on the two antenna patches. This via is galvanically connected to both the L1 and the L5 patches.

3 RF PERFORMANCE OF THE GNSS ANTENNA DEMONSTRATOR

A demonstrator of the integrated antenna was manufactured in a 400 by 400 mm GLARE panel. The antenna patches were placed in the autoclave together with the materials for the GLARE panel. The resulting integrated antenna is shown in Figure 4.

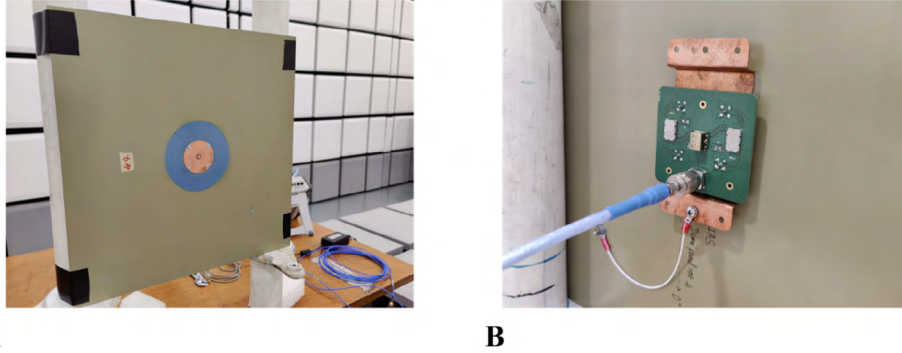


Figure 4: Two images of the integrated GNSS antenna demonstrator. **A** shows the antenna as seen from the outside of the fuselage. **B** shows the antenna feed network connected to the integrated antenna on the inside of the fuselage.

The antenna is fully integrated in the GLARE panel and has a flush finish on the outside of fuselage. The copper patch used for the L1 radiation is visible from the outside of the fuselage, together with the glass fibre window. The feed network PCB is mounted on the inside of the fuselage as shown in Figure 4 B. The antenna cavity is not visible from the inside of the fuselage.

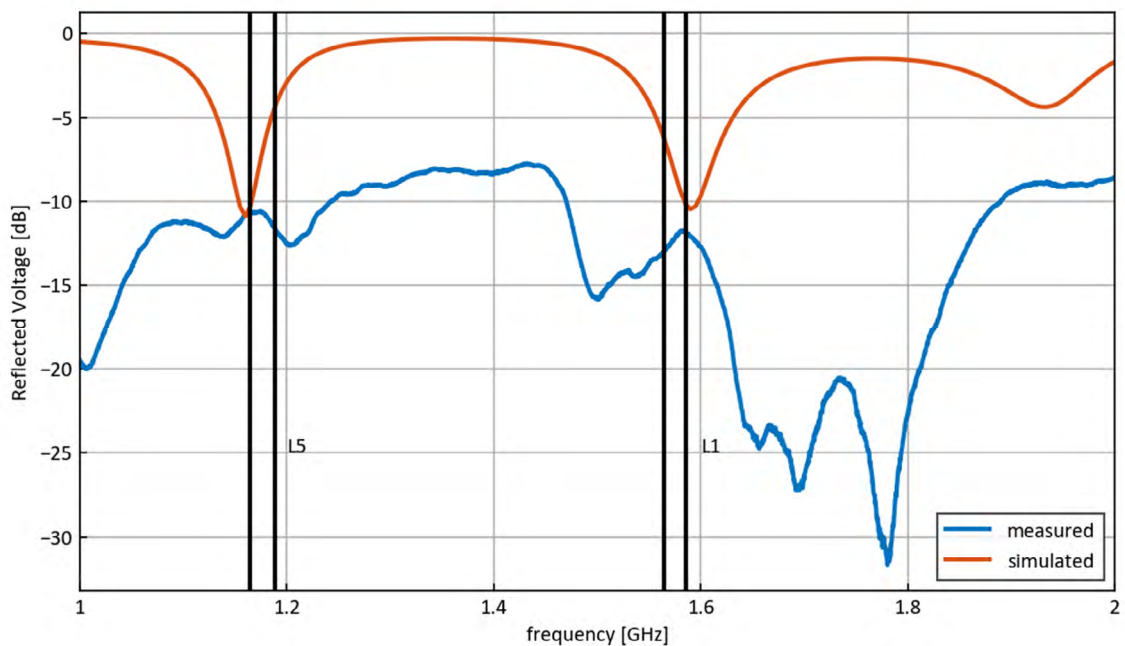


Figure 5: Simulated and measured reflected voltage of the antenna demonstrator. The L1 and L5 GNSS frequency bands are indicated by the black vertical lines.

3.1 Reflected voltage

The reflected voltage of the antenna demonstrator was measured using the vector network analyser. The measurement results are shown in Figure 5. The measured reflected voltage is lower than the required -10 dB target within the L1 and L5 GNSS frequency bands. This indicates that the antenna will work within these frequency bands.

Notably, the measured reflected voltage does not correspond well with the simulations performed in HFSS. The similarity between results can likely be improved if the reflected voltage of the demonstrator antenna is measured without the feed network. This was not possible at the time of writing due to missing parts required to perform this measurement.

Moreover, shifts in resonance frequency are likely caused by uncertainty of the electromagnetic properties of the glass fibre layers used in the GLARE panel or by fabrication inconsistencies of the demonstrator panel. More measurements are required to identify the nature of the frequency shifts.

3.2 Radiation pattern

The radiation pattern of the antenna was also measured for the L1 GNSS frequency band. The measurement setup is shown in Figure 6. The setup was used to measure the angular dependence of the antenna gain. These gains are shown in Figure 7.



Figure 6: Measuring setup used in measuring the radiation pattern of the antenna demonstrator. A Right Handed Circular Polarized (RHCP) antenna or a Left Handed Circular Polarized (LHCP) antenna is placed on the far side of the room. The antenna demonstrator is rotated from -90 to 90 degrees.

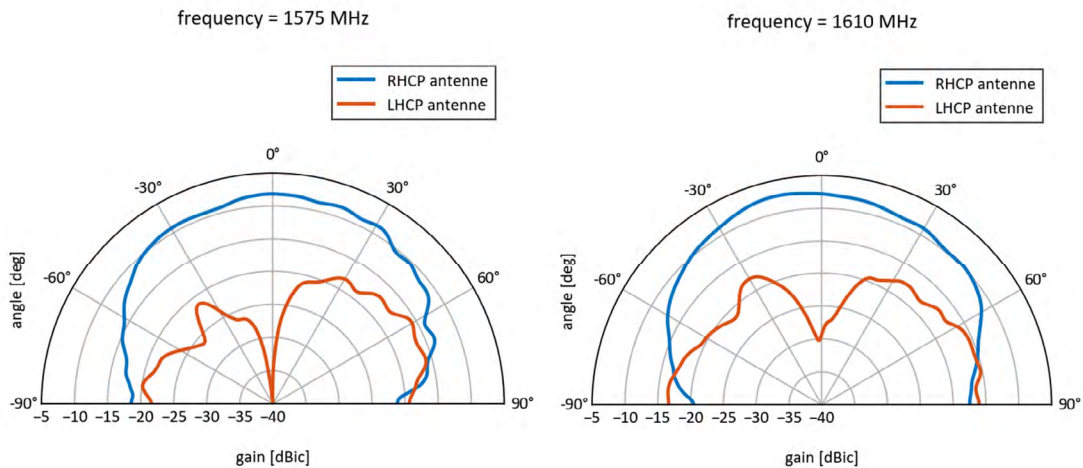


Figure 7: Measured RHCP and LHCP gain of the integrated GNSS antenna demonstrator at 1575 and 1610 MHz.

The measurements show good RHCP gain for a broad viewing angle. However, the total gain of the antenna is lower than expected. This could be either due to additional losses in the GLARE materials, or due to issues with the feed network. More measurements are required to pinpoint the exact cause of these losses. Nevertheless, the (LHCP) radiation graphs show good rejection of cross polar radiation. This indicates good polarization purity of the antenna demonstrator.

4 CONCLUSIONS

A GNSS antenna was manufactured directly into a classical GLARE FML panel. The resulting antenna has a flush finish on the outside of the fuselage panel and has little impact on the inside of the fuselage panel. A feed network, required for RHCP radiation, was designed on a PCB and mounted on the inside of the fuselage panel. Measurements of the antenna with the feed network show lower than -10 dB reflected voltage for a broad frequency range. However, additional measurements are required to fully characterize the antenna.

The radiation pattern of the L1 GNSS frequency band was also measured. The RHCP and LHCP radiation patterns indicate good radiation purity in the L1 band. However, the gain of the antenna is lower than expected. More measurements are required to identify the cause of these losses.

5 ACKNOWLEDGEMENTS

This project has received funding from the European Union's Horizon2020 research and innovation programme under grant agreement No.723167.

REFERENCES

- [1] K. A. Yinusa, "A Dual-Band Conformal Antenna for GNSS Applications in Small Cylindrical Structures," *IEEE Antennas Wirel. Propag. Lett.*, vol. 17, no. 6, pp. 1056–1059, Jun. 2018, doi: 10.1109/LAWP.2018.2830969.

RF ANALYSES OF INTEGRATED KU-BAND ANTENNA

EMUS 2020

J. VERPOORTE*, A. HULZINGA*,
M. MARTINEZ VÁZQUEZ†, J. LEISS†, M. WILLEMSSEN†,

* Royal Netherlands Aerospace Centre (NLR)
Voorsterweg 31, 8316 PR Marknesse, The Netherlands
e-mail: {Jaco.Verpoorte, Adriaan.Hulzinga}@nlr.nl, web page: <http://www.nlr.nl>

† IMST GmbH
Carl-Friedrich-Gauss-Str. 2-4, 47475 Kamp-Lintfort, Germany
e-mail: {Martinez, Leiss, Willemsen}@imst.de, web page: <http://www.imst.de>

Key words: Phased array antenna, integration, simulation, measurement.

Abstract. In the ACASIAS project an integrated antenna for Ku-band satellite communication has been developed. The design of this integrated antenna has to meet structural, electromagnetic and thermal requirements. This paper addresses the electromagnetic performance of the antenna both by design and by measurement. For the design of the antenna, the electromagnetic interaction of the antenna with the conducting Carbon Fibre Reinforced Plastic (CFRP) ribs of the orthogrid and the interaction with the Glass Fibre Reinforced Plastic (GFRP) skin of the panel have been analysed. In addition, the influence of potential lightning diverters on the antenna performance has been analysed. The radiation pattern of a single antenna tile and the radiation pattern of an antenna tile integrated in the orthogrid fuselage panel were measured. The results of the antenna measurements are compared with the results of the simulations carried out for the design of the antenna.

1 INTRODUCTION

The ACASIAS project focuses on four innovative solutions, which aim at reduction of fuel consumption and reduction of CO₂ and NO_x emissions. One of these innovations concerns the integration of a Ku-band antenna array in the fuselage of the aircraft. The integrated Ku-band antenna will enable airborne satellite communication. The antenna array consists of 24 antenna tiles, which will be fully integrated in an orthogrid fuselage panel. The design bandwidth of the antenna is 2 GHz for the RX (receive) antenna and 0.5 GHz for the TX (transmit) antenna. The antenna elements consist of stacked patches to obtain this bandwidth. The design of this integrated antenna has to meet structural, electromagnetic and thermal requirements. This paper addresses the electromagnetic performance of the antenna both by design and by measurement.

For the design of the antenna, the electromagnetic interaction of the antenna with the conducting CFRP ribs of the orthogrid and the interaction with GFRP skin of the panel were analysed [1,2]. In addition, the influence of potential lightning diverters on the antenna performance was determined. The demonstrator antenna array will consist of 2 TX tiles

combined with 22 dummy tiles or 2 RX tiles combined with 22 dummy tiles. The TX and RX antenna tiles each consist of 8x8 antenna elements. Manufacturing of a full array of 24 active tiles was not possible in the scope of this project because of significant costs of the hardware. The dummy tiles are being used to investigate the thermal control of a full array of 24 tiles. The dummy tiles have the same thermal characteristics as the TX tiles. The antenna does not have a beamsteering network because the focus of the research was primarily on the integration aspects (electromagnetic interaction, thermal control). The antenna tiles were manufactured and afterwards subjected to electromagnetic and thermal tests. The electromagnetic tests comprise measurement of the radiation patterns. The radiation pattern of a single antenna tile and the radiation pattern of an antenna tile integrated in the orthogrid fuselage panel were measured. In this paper the results of the antenna measurements are compared with the results of the simulations carried out for the design of the antenna.

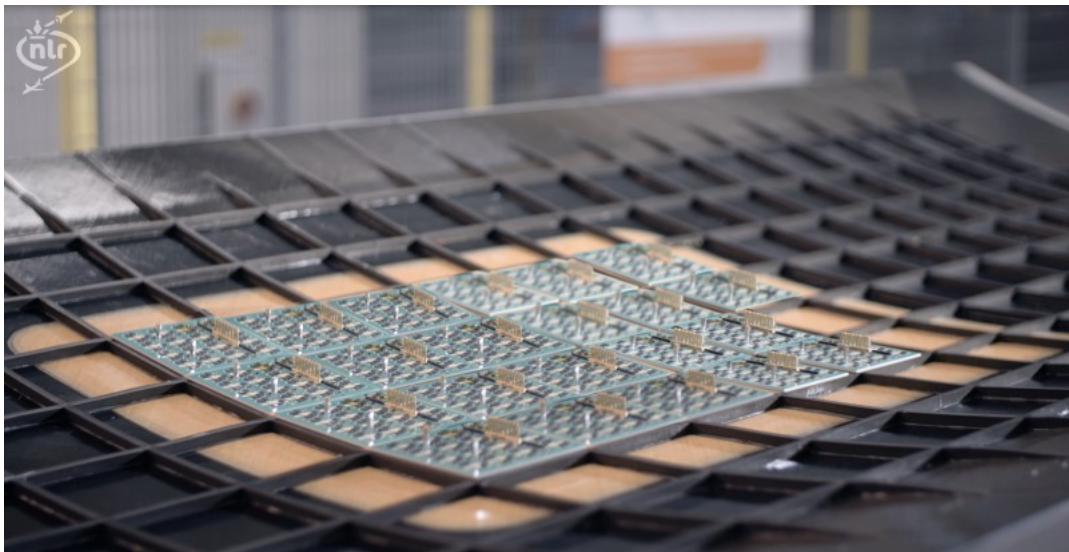


Figure 1: Ku-band antenna tiles integrated in a full-scale fuselage panel consisting of a CFRP orthogrid. The skin of the panel is also made of CFRP but in the center of the panel the skin is made of GFRP which is transparent for the electromagnetic waves.

2 SIMULATION OF INTEGRATED ANTENNA PERFORMANCE

For the design of the integrated antenna array several simulations were carried out to assess the influence of the orthogrid and skin on the antenna performance (the input impedance and radiation pattern). Also the potential influence of lightning diverters was assessed.

2.1 Influence of CFRP orthogrid and GFRP skin

The radiation patterns of a single antenna tile (non-integrated and integrated) are shown in Figure 2 and Figure 3. These patterns were calculated by using EMPIRE XPU™. The 8x8 array has a null-to-null beamwidth of about 28° and a first sidelobe level at -13.5 dB as expected for a rectangular array of 8x8 antenna elements with uniform amplitude distribution. The cross-polarization level is about -16 dB. Figure 3 shows the effect of integrating the

antenna in a conductive orthogrid with GFRP skin. For this simulation the distance between antenna tile and GFRP skin was 6 mm. The simulations show a reduced level of the sidelobes, for both co-polar and cross-polar. The effect on the main lobe is not significant.

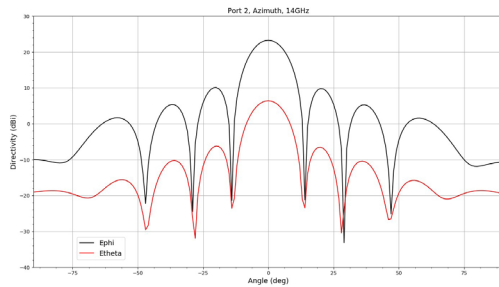


Figure 2: Radiation pattern of a single antenna tile (polarization 2, azimuth scan at 14 GHz).

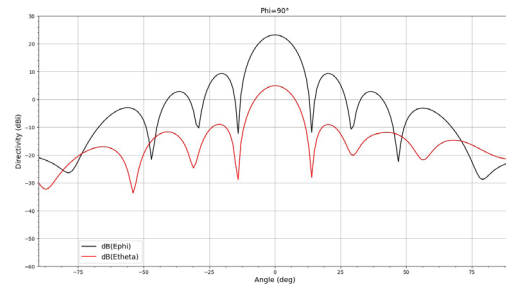


Figure 3: Radiation pattern of an integrated antenna tile (polarization 2, azimuth scan at 14 GHz) for 6 mm distance between the antenna tile and the skin.

In [1] and [2] the influence of the tile separation on the radiation pattern was described. The antenna tiles have a separation of 7 mm due to the thickness of the ribs of the orthogrid. This separation is in the order of a quarter of the wavelength and therefore this gap will have an influence on the radiation pattern. Due to the tile separation there is an increase in sidelobes (Figure 4). In order to comply with limits for the radiation pattern of transmit antennas for Ku-band satellite communication [4][5], these sidelobes will have to be suppressed. This can be done applying amplitude tapering to the array. However, this will add additional complexity and the overall efficiency of the antenna will decrease.

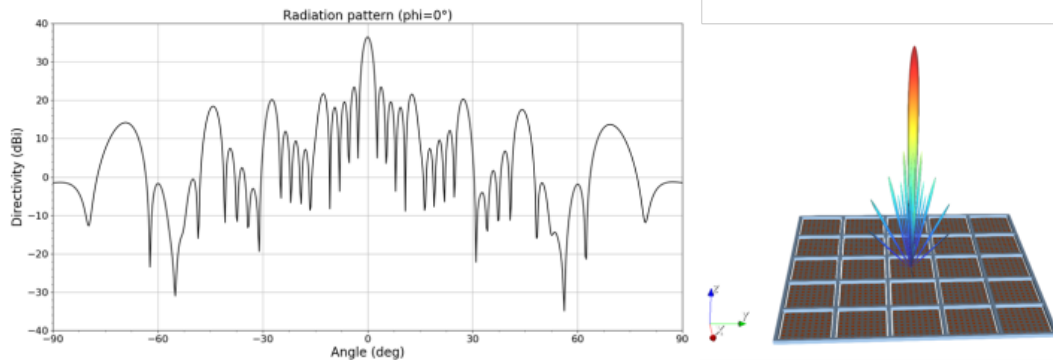


Figure 4: Radiation pattern of the full 40*40 elements array (gap between 8*8 tiles: 7 mm).

The influence of the thickness of the GFRP skin was also addressed in [1]. For structural strength and stiffness purposes the GFRP skin thickness has a thickness of 2.1 mm. This is not ideal for electromagnetic purposes. Either a thin (1 mm or less) or a half-wavelength thick skin would be the most optimum.

In addition the distance of the tile to the skin is of influence on the antenna performance. Simulations have shown that, to minimize the influence of the skin on the input impedance of the antenna elements, the antenna should have a certain minimum distance to the skin (in the order of 6 mm). This behavior is confirmed by measurements (section 3.1).

2.2 Influence of metal lightning diverters

The antenna array will have lightning protection on two levels: for protection against direct lightning effects lightning diverter strips will be used and for protection against indirect lightning effects the top patch of the stacked patch antenna elements will be grounded (this also protects against electrostatic discharge). The lightning diverter strips will be installed only above the ribs of the orthogrid in order not to disturb the radiation pattern of the antenna tiles. The analysis described in [1] showed that the influence of the lightning diverters is visible but the effect is negligible and the radiation pattern is still acceptable.

3 MEASUREMENT OF INTEGRATED ANTENNA PERFORMANCE

3.1 Influence of CFRP orthogrid and GFRP skin

To assess the influence of the orthogrid and skin on the antenna performance, radiation pattern measurements were carried out on a single TX antenna integrated in an aluminium orthogrid with GFRP skin (Figure 5). The aluminium ribs of the orthogrid are more conductive than the CFRP ribs of the full-scale fuselage panel but the influence on the antenna performance is similar.

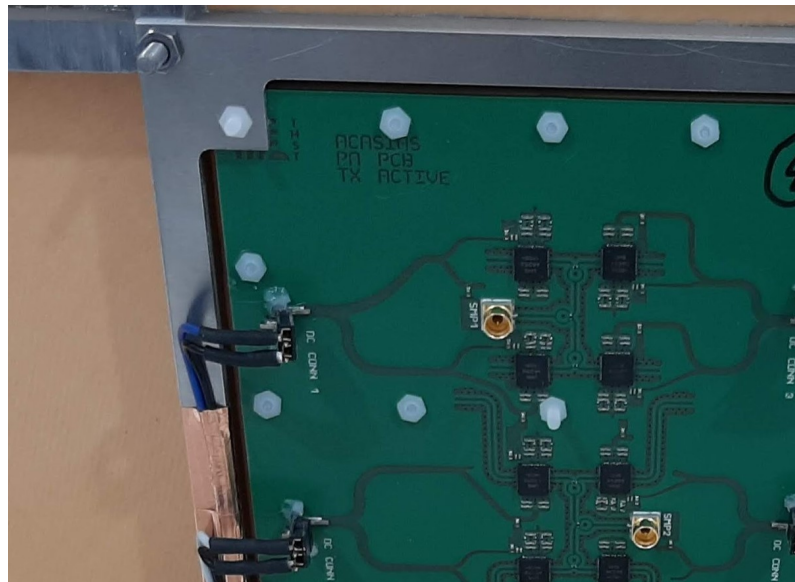


Figure 5: Single TX antenna tile integrated in aluminium orthogrid with GFRP skin.

The results of the measurements are shown in Figure 6 and Figure 7. The figures show the measured antenna gain normalized to the gain of the non-integrated antenna tile at 14 GHz. Measurements were carried out with and without orthogrid. In addition the distance between the antenna tile and the skin was varied by using a metal bracket. The results of the co-polar measurements of a single linear polarization are shown in Figure 6 for several distances between skin and antenna tile. The distance between the skin and the tile has a significant influence on the received power. The highest gain of an integrated antenna tile is achieved for

a distance of 6 mm. At that distance the gain is about the same as for the antenna tile which is not integrated. For shorter distances the gain decreases and the sidelobes increase. The sidelobe level for the case of the non-integrated antenna is higher than predicted (-7 dB versus -13.5 dB). This is probably caused by small differences between the amplifiers, splitters and traces used in the antenna. In the simulations ideal components were used.

Figure 7 shows the results of the co-polar and cross-polar measurements of the TX antenna tile integrated in the panel (with a distance of 6 mm to the skin). In the main lobe the ratio between the co-polarization and the cross-polarization is about 15 dB. This is close to the predicted level.

As soon as the RX tiles are available, the same measurements will be carried out on the RX tiles as on the TX tiles. It is expected that the behavior of the RX tiles is similar to the that of the TX tiles. Finally, also the thermal behavior of the integrated tiles will be measured.

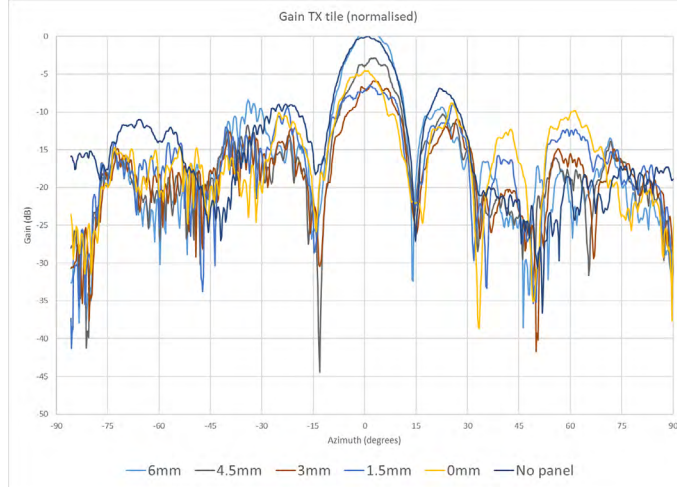


Figure 6: Normalised antenna gain of TX tile (measured) for several distances between the skin and the tile aperture and for the case of a single antenna not integrated in the fuselage panel.

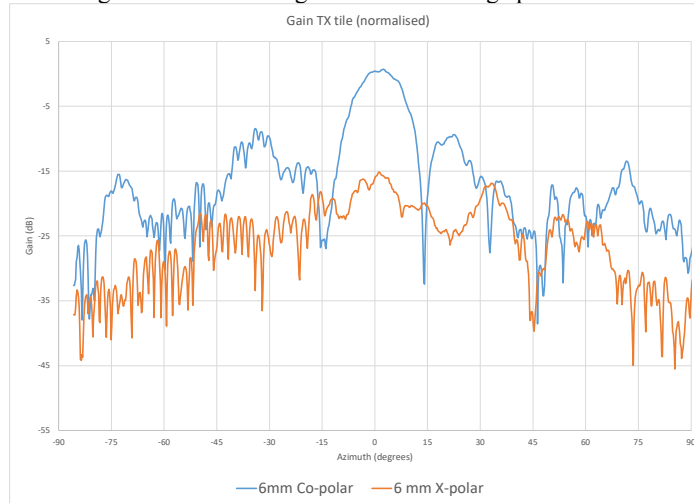


Figure 7: Normalised antenna gain of TX tile (measured) for co-polarisation and cross-polarisation. In both cases the distance between the antenna tile and the skin is 6 mm.

4 CONCLUSIONS

During the design of the integrated antenna tile the influence of the CFRP orthogrid and GFRP skin on the antenna performance was analyzed. The orthogrid and skin have an influence on the performance of the antenna but the effects are either acceptable or can be compensated (application of tapering to reduce sidelobe level). The effect on the antenna performance of lightning diverters added to the skin of the panel is negligible. The measurements on an integrated antenna tile confirm the influence of the GFRP skin. The best antenna performance is obtained for a distance of 6 mm between antenna and skin. The measurements on an integrated antenna tile confirm the predicted ratio between the co-polar and the cross-polar level in the main beam. The measurements show that integration of a Ku-band antenna tile in a composite structure is feasible without significant loss of performance.

ACKNOWLEDGMENT

All work described in this paper has received funding from the European Union's Horizon 2020 research and innovation programme under grant agreement No. 723167, ACASIAS project. The authors want to acknowledge the contribution of all the partners in the ACASIAS project.

REFERENCES

- [1] "Structural Integration of Ku-band SatCom Antenna into novel Fuselage Panel", J. Verpoorte and A. Hulzinga, EMuS 2019 Conference.
- [2] "Advanced Concepts for Aero-Structures with Integrated Antennas and Sensors (ACASIAS)", Yuri Konter, Jaco Verpoorte, Adriaan Hulzinga, Marta Martínez Vázquez, ESA Antenna Workshop 2019.
- [3] "Structurally integrated phased array antennas for aeronautical SatCom applications", Marta Martínez-Vázquez, Jaco Verpoorte, Jens Leiß, Maren Willemsen, Adriaan Hulzinga, Zdeněk Řezníček, submitted for EuCAP 2021.
- [4] ITU recommendation S.1428-1 "Reference FSS earth-station radiation patterns for use in interference assessment involving non-GSO satellites in frequency bands between 10.7 GHz and 30 GHz"
- [5] ETSI 302 186 "Harmonised Standard for satellite mobile Aircraft Earth Stations (AESs) operating in the 11/12/14 GHz frequency bands"

STRUCTURAL ANALYSES OF GLARE-GFRP TRANSITION FOR INTEGRATED VHF ANTENNA ON A FUSELAGE PANEL

EMUS 2020

F. TURON^{*}, F. OTERO^{*} AND X. MARTINEZ^{**†}

^{*} International Center for Numerical Methods in Engineering (CIMNE)
Universidad Polit cnica de Catalu a
Campus Norte UPC, 08034 Barcelona, Spain
e-mail: congress@cimne.upc.edu, www.cimne.com

[†] Departamento de Ciencia e Ingenieria Nautica (FNB)
Technical University of Catalonia (UPC)
Pla de Palau 18, 08003 Barcelona, Spain
email: semni@cimne.upc.edu, www.semni.org

Key words: Smart fuselage panel, composite materials, serial-parallel mixing theory, constitutive modelling, finite element methods

Abstract. The objective of this paper is to describe the numerical simulation of the transition zones in the multifunctional fuselage panel design to integrate a VHF (Very High Frequency) antenna. The panel is made of GLARE (Glass Laminate Aluminium Reinforced Epoxy) with a central window of GFRP (Glass Fibre Reinforced Polymer). The structural analyses of the transition GLARE/GFRP is presented along with its experimental validation. The numerical simulations showed a very high level of correlation with the experimental tests, both in the longitudinal load vs displacement curves and deformations captured with strain gauges and DIC (Digital Image Correlations).

1 INTRODUCTION

Providing composite structures with new functionalities often involve merging different material configurations, including layups and components, into a single continuous structure. This can produce transition zones with complex interactions between layers that must be studied in detail by simulations. Moreover, numerical simulations can also assist in the design process of this new composites structures.

This approach is put in practice during the procedure exposed on this paper, from the initial phase of assisted design to the experimental verification. The resultant GLARE/GFRP transition archived is broadly analysed with both, an experimental campaign and its equivalent numerical analysis. Most relevant results for the two representative orientations of final layout are presented. These are, the optimal and more demanded layout properly oriented i.e. Section BB in Figure 1, which is referred as MST-B (Mechanical Static Test) and secondly its complementary orientation MST-C in which the fibres are rotated 90 degrees. This second configuration is placed in less demanded direction.

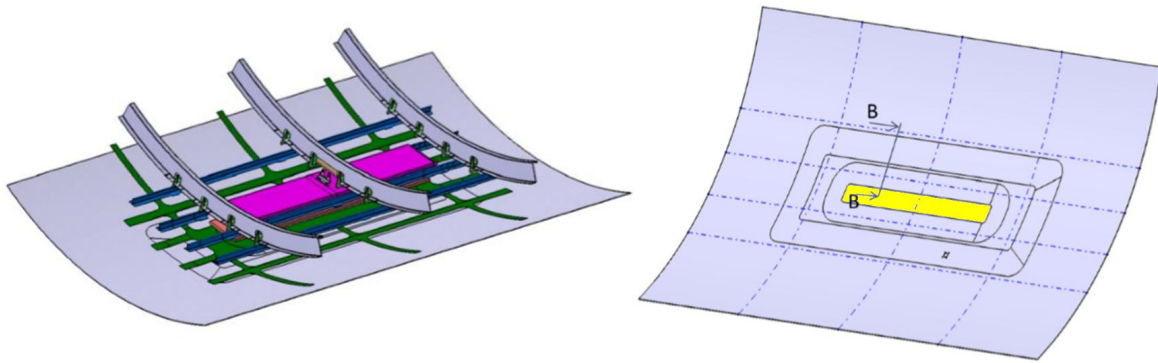


Figure 1: Integrated VHF Antenna in fuselage structure.

Design procedure.

The design procedure carried out to find the best transition to join the GLARE laminate with the GFRP windows located at the centre of the fuselage panel (shown in yellow at Figure 1) began with the numerical simulation of a predesign. The procedure shows some critical spots between the end of the aluminium sheets, proceeding from the GLARE laminate, and the beginning of the GFRP layers replacing them.

A better response was achieved when orientating the fibres of these GFRP layers following (parallel) the edge of the aluminium sheets as shown in Figure 2. Otherwise the high rigidity of the glass caused a sudden separation between the GFRP layers and the aluminium sheets that resulted in a quicker expansion of the damage to the surrounding layers. Despite not being structurally critical, the prevention of this micro damage could improve the structural long-term performance.

Finally the long fibres are placed just above and below the aluminium sheets, in addition a small resin gap is added between the parallel GFRP and the aluminium layers next to them leading to an optimal layout shown in Figure 2.

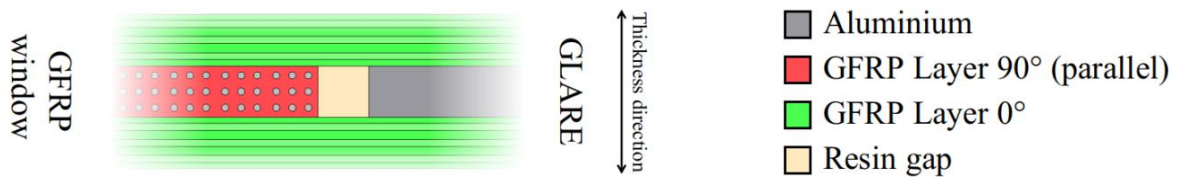


Figure 2: Critical spot from optimal orientation layout configuration for transition cross section BB.

In this way the stresses of the aluminium sheets are transferred to the surrounding long fibres across its whole upper and lower contact surfaces and the epoxy matrix of the parallel layers benefits from the high stiffness and low deformation of these. The resulting transition geometry manage to stream the stresses between its ends gradually, minimizing the areas of stress concentrations. Therefore, reducing the critical points that can lead to intralaminar fracture and delamination phenomena. The whole final layout of the transition are confidential and can not be shown on this publication.

1.1 GEOMETRY AND TEST SETUP OF THE SPECIMEN

The dimensions of the tested specimens are 700 mm length and 100 mm width, the free length between jaws is 580 mm (See Figure 3). In Figure 3 the location of the strain gauges i.e. 1 and 3 on the inner side and 2 and 4 on the outer side (see red cross points) are shown.

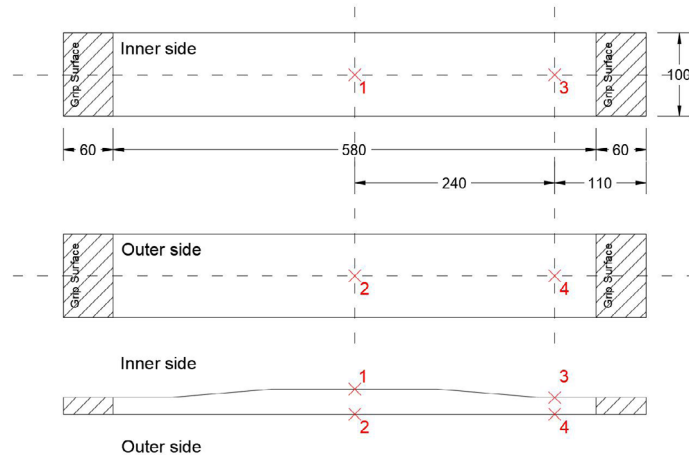


Figure 3: Generic size of specimens [mm]

In the experimental test, a displacement is imposed by means of a piston that slowly displaces one jaw meanwhile the other remains steady. The reaction of the specimen and the imposed displacement are recorded. Moreover, deformations are measured using the four strain gauges together with a Digital Image Correlation (DIC) equipment.

1.2 NUMERICAL MODEL

The numerical model developed reproduces the geometry of the laminate layer by layer along the whole transition, including the small resin gaps located between layers. Each of the GFRP layers are discretized with an element in the direction of thickness, while two elements are used in the aluminium sheets. Then, it allows to analyse the stress-strain state of each layer individually. The finite element mesh has approximately 250.000 hexahedral linear elements with 8 nodes and 8 Gauss points.

GFRP is simulated using the mixing theory Serial-Parallel [1][2][3] already used in the analysis of a multifunctional Orthogrid Panel [4]. It together with the non-linear constitutive models used in the the fibres and matrix, it is able to monitor the onset and evolution of damage and plasticity, On the other hand, the aluminium material is characterized with a plastic constitutive law, which reproduces accurately the non-linear behaviour of GLARE.

The numerical simulation takes advantage of the symmetry of the specimen and its layout and only a quarter of the total geometry is simulated. The effect of the clamp is implemented by imposing a displacement in the Y direction and restricting movement also in the X direction on all nodes under the grip area.

Experimentally it was proved that the displacements out of the plane were low and their impact could be neglected. For these reasons the analysis were made within the small deformations paradigm, but in order to prevent fictitious bending was necessary restrict movement in the Z direction on the entire outer face of the panel.

3 NUMERICAL RESULTS

In the present section the comparison of the numerical vs experimental results is presented for the two configuration studied. The loads and displacement from the piston test machine, as well as the strains measured with the strain gauges and captured with the DIC are used for the comparison.

3.1 LAYOUT CONFIGURATION MST-B

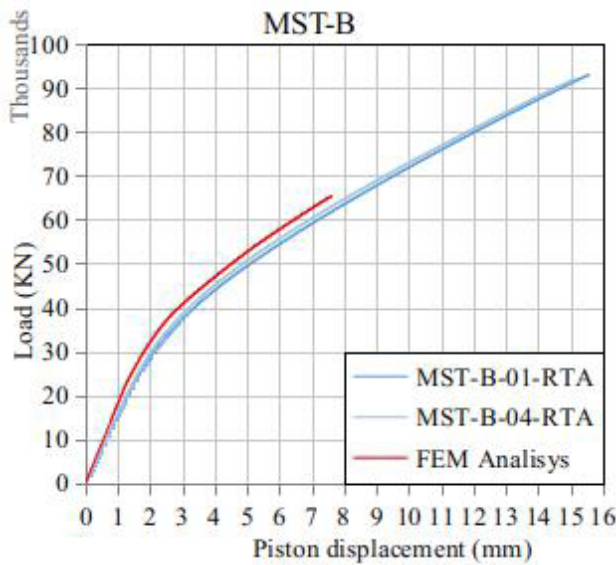


Figure 4: MST-B Load vs Displacement

Figure 4 shows the load vs displacement curve for configuration MST-B.

The initial stiffness obtained in the experimental test is very similar in comparison with the numerical analysis. When one-millimetre displacement is reached, the experimental results show a progressive loss of stiffness. The numerical simulation also shows accurately this stiffness loss. However the overall stiffness is slightly higher.

The load vs strain curves obtained with the strain gauges and DIC show a good correlation between the experimental and numerical results (See Figure 5). It can be seen in both graphs how the rigidity of the central zone (SG2) is constant with a very good approximation by the numerical

analysis. The response in the GLARE is not that high and it suffers a loss of stiffness between 4000 and 5000 micro strains. This drop is more abrupt in the numerical analysis although the two graphs behave similarly.

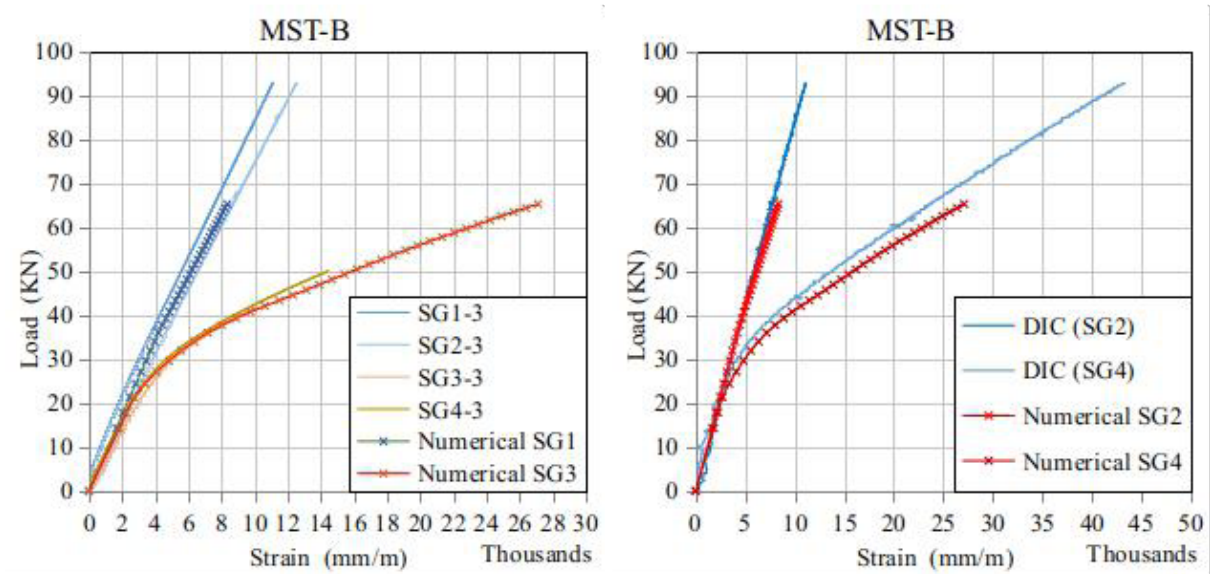


Figure 5: Resultant Load vs Strain curves of B configuration (strain gauges - DIC)

3.2 LAYOUT CONFIGURATION MST-C

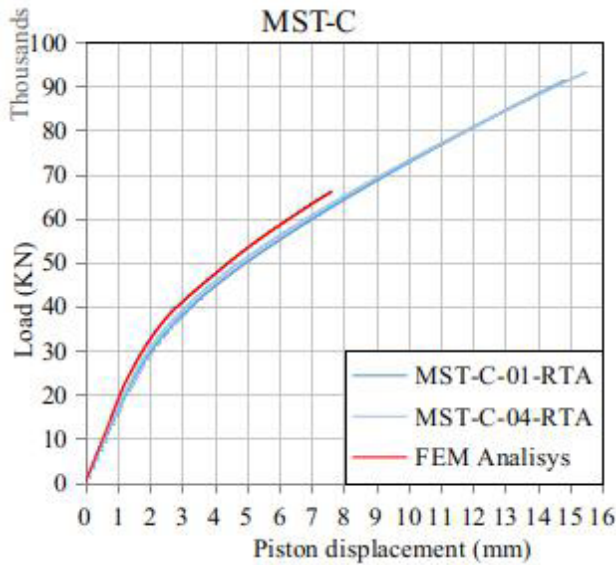


Figure 6: MST-B Load vs Displacement

Despite being poorly oriented the experimental overall response of configuration MST-C is almost identical to that measured in configuration MST-B. In addition the numerical analysis shows a extremely similar behaviour (see Figure 6).

The numerical analysis also shows a good correlation with the deformation recorded in the central strain gauge as well as in the GLARE sections as can be seen in Figure 7.

However, due to the non-optimal orientation of the fibres adjacent to the aluminium sheets, more and more damage zones are registered in the resin that joins them, as well as in the resin of the perpendicular GFRP layers located

immediately above and below.

These small matrix micro damage zones do not impact globally the performance of the structure in comparison to the optimally oriented configuration, but it is still necessary to reduce their occurrence in order to prevent future delamination,.

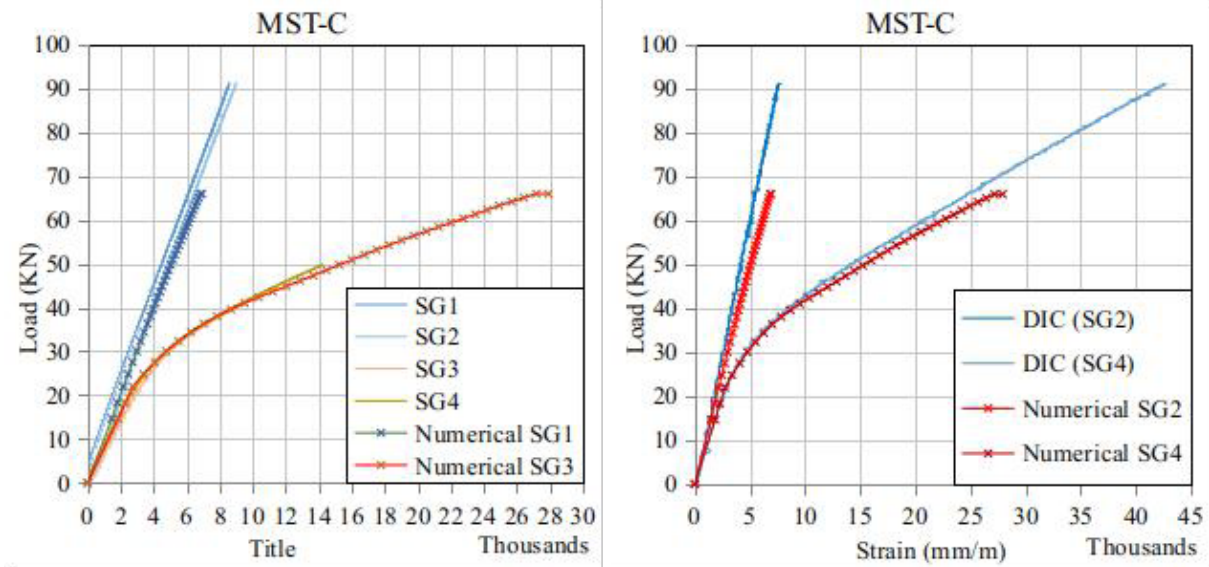


Figure 7: Load vs strain of Test MST, for Layout C

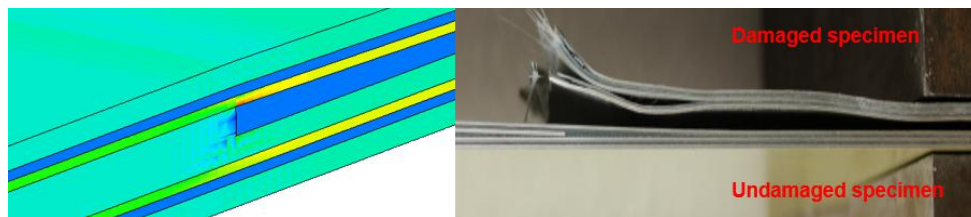


Figure 8: Breakage area

Finally, it can be observed in Figure 8 how the breakage zone in the experimental test coincides with the zone with the highest stresses found in both numerical simulation, configuration B and C. In this area, the stresses in the fibres orientated in longitudinal direction reach the ultimate tensile strength causing the overall failure of the sample.

4 CONCLUSIONS AND FINAL REMARKS

- The numerical simulation shows a predicted initial stiffness in good agreement with the experimental results. The global response of both configurations tested starts with a non-linear behaviour around 0.8 mm of piston displacement as it can be observed in the load vs displacement experimental curves (see Figures 4 and 6). The numerical results follow a very similar behaviour but with a slightly higher stiffness. After that, both curves, i.e. experimental and numerical, remain parallel with the same slope.
- The load vs strain curves of the both configurations reflect a good simulation at the microscopic level, with deformation curves that are very close to the experimental ones. It can therefore conclude that the constitutive level is simulated correctly
- The great similarity in the behaviour of both configurations indicates a good balance in the orientation of layers which reaches to a laminate with correct orthotropic behaviour.
- The failure zone in the experimental test coincides with the point with the highest stress concentration in the numerical simulations. The strain recorded just before the break matches the ultimate strain of the glass fibres defined in its constitutive behaviour,

REFERENCES

- [1] Rastellini F. and Oller S. and Salomón O. and Oñate, E. Composite materials non-linear modelling for long fibre-reinforced laminates continuum basis, computational aspect and validations. *Computers and Structures*. (2008) 86:879-896.
- [2] Car E. and Oller S. and Oñate, E. An anisotropic elastoplastic constitutive model for large strain analysis of fiber reinforced composite materials. *Computer Methods in Applied Mechanics and Engineering*. (2000) 185:245-277.
- [3] Martinez X. and Oller S. Numerical simulation of matrix reinforced composite materials subjected to compression loads. *Archives of computational methods in engineering*. (2009) 16:357-397.
- [4] Francesc Turon, Fermin Otero And Xavier Martinez. *Structural Analyses Of Orthogrid Fuselage Panel For Integrated Ku-Band Satcom Antenna – Emus 2019*

Acknowledgements: This work has been supported by the European Union's Horizon 2020 research and innovation programme under grant agreement No. 723167 (ACASIAS project).

STRUCTURAL ASSESSMENT OF FML AEROSTRUCTURES WITH INTEGRATED ELECTROMAGNETIC FEATURES

EMUS 2020

J.F. de FREITAS*, C. van HENGEL*, P. HOMOLA†

* GKN Fokker Aerostructures
Industrieweg 4, 3351 LB Papendrecht, The Netherlands
Email: joao.defreitas@fokker.com; Email: cees.vanhengel@fokker.com
Webpage: <http://www.gknaerospace.com>

† VZLU Aerospace Research and Test Establishment
Beranových 130, 190 05 Praha - Letnany, Czech Republic
Email: homola@vzlu.cz
Webpage: <https://www.vzlu.cz>

Key words: Structural behavior, GLARE, integrated slot antenna, structural element testing

Abstract. A substantial contribution to reduce the aerodynamic drag and consequent CO₂ and NO_x emissions is to integrate communication antennas in the aircraft structure. This paper presents a GLARE fuselage panel design for an integrated VHF slot antenna and discusses the results of a mechanical experimental campaign on a structural element level, in quasi-static tensile conditions. The tested specimens showed small variability in terms of stiffness and strength (typical for GLARE), little dependence on the ambient conditions, damage presence, and layup configurations and good agreement with early numerical simulations. In addition, stiffness and strength predictions, based on empirically found design values seem to correlate well with the found test values.

1. INTRODUCTION

Conventional aircraft VHF communication and GNSS antennas are (fin- and teardrop-shaped, respectively) protruding structures, containing electromagnetic equipment, typically assembled on top of the aircraft fuselage. These structures disturb the airflow around the fuselage, increasing the aerodynamic (friction and pressure) drag, which ultimately translates into a greater fuel consumption.

In an effort to mitigate this undesired effect, the ACASIAS project develops innovative integrated antenna solutions in the aerostructures. In this context, GLASS fiber REinforced aluminium laminate (GLARE) offers a large design freedom in tailoring the material to very specific electromagnetic, structural and manufacturing requirements. Most importantly, GLARE provides a unique material opportunity for a slot antenna application.

A slot antenna works under the principle of electromagnetic wave radiation around the slot by an induced radio frequency current. The optimal length for an air-filled slot antenna is half a wavelength [1]. However, for electromagnetic (for higher permittivity) and structural integrity (for higher load carrying capacity and durability) reasons, the selected solution for the slot is similar to a ‘patch-repair’ but with the Glass Fiber Reinforced Epoxy (GFRE) layers interspersed with the aluminium sheets [Figure 1 c)] allowing smooth load paths, thus avoiding pronounced stress concentrations.

This paper aims to assess the structural behavior of the integrated slot antenna solution in a GLARE panel, through an experimental approach backed by simple stiffness and strength predictions. The article is structured as follows: section 2 elaborates on the structural design of the integrated antenna, motivating its design and material choices, where the mechanical properties of GLARE are examined. Section 3 briefly sets the experimental methodology for the quasi-static testing of the structural elements, including the instrumentation used. In section 4, results are presented and discussed. Section 5 draws the conclusions from this study.

2. STRUCTURAL DESIGN OF AN INTEGRATED VHF ANTENNA

2.1 Geometry and size

The length of the slot affects the resonance frequency of the antenna. In addition, the shape of the antenna influences the radiation pattern. The optimal length for an air-surrounded slot antenna is half a wavelength. However, because a higher permittivity epoxy-filled Parallel Plate Resonator (PPR) was coupled inside the fuselage to reflect back the radio waves to the exterior of the aircraft¹, the optimum length of the slot had to be found through simulations carried out by the NLR [1].

The proposed design for the integrated VHF slot antenna in a fuselage panel comprises a smooth transition from a 1.4mm thick GLARE 3 (in light blue - Figure 1) to a 3.5mm thick full-S2/ GFRE (in orange –Figure 1). The ring region in between these two materials consists of plydrop transitions (in green - Figure 1) designed to mitigate pronounced stiffness differences and consequent undesirable stress concentrations.

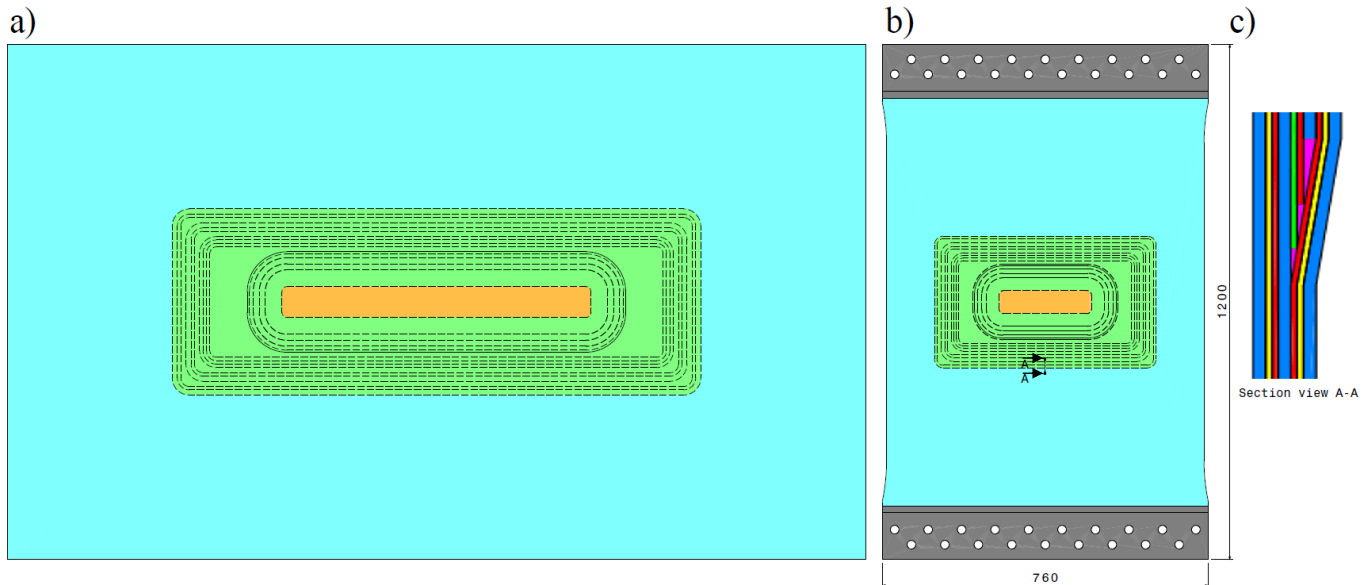


Figure 1: Panel drawings: a) demonstrator panel; b) test panel; four different regions and corresponding materials are color coded: GLARE 3 in light blue, S2/GFRE in orange, GLARE 3 – GFRE transition in green and aluminium bonded tabs in gray c) section view A-A: ply drop detail.

2.2 Material properties and layup configurations

GLARE is a Fiber Metal Laminate (FML) material for advanced aerospace applications, composed of thin 2024-T3 aluminium alloy sheets interspersed with unidirectional layers of

¹ These waves would otherwise propagate to the interior of the aircraft.

GFRE prepreg, where the epoxy resin bonds the metal sheets and the glass fiber layers together (Figure 2). This material exhibits unique features, namely: exceptional fatigue properties [2], specifically due to slower crack growth behavior (through fiber bridging phenomenon - Figure 3 - that reduces the stress intensity at the crack tip in the aluminium layers) [3] and high impact-, corrosion- and fire-resistances [2].

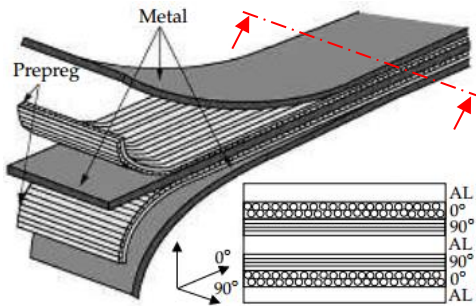


Figure 2: FML material diagram.

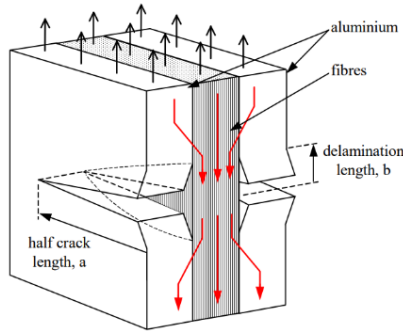


Figure 3: Fiber bridging in GLARE. Reproduced from [3], 2006

Table 1: Material properties of GLARE 3.

Material	Ply level				Laminate level	
	Al 2024-T3	SRC	FM94-27% - S2 GFRE	SRC	GLARE 3 - 3/2 - 0.3	SRC
t [mm]	0.3		0.125		1.4	
ρ [g/mm ³]	2.77E-03	TH	1.97E-03	[4]	2.48E-03	CLT
E_1/E_2 [GPa]	72/ 72	TH	53.2/ 9.3	[4]	58.1/ 58.1	CLT
G_{12} [GPa]	27.07	TH	5.5	[4]	19.36	CLT
ν_{12} [-]	0.33	TH	0.28	[4]	-	
σ_{yL}/σ_{yT} [MPa]	352/ 323	TH	-		269.3/ 246.3*	TH
σ_{uL}/σ_{uT} [MPa]	476/ 458	TH	1989/ 36	TH	632.5/ 588.5*	TH

Symbol representation: t - ply thickness; ρ - material density; E_1/E_2 - longitudinal and transverse elastic modulus; G_{12} - shear modulus; ν_{12} - major Poisson ratio; σ_{yL}/σ_{yT} - longitudinal and transverse yield strength; σ_{uL}/σ_{uT} - longitudinal and transverse ultimate strength; SRC- source; TH-Fokker Technical Handbook [5]; CLT - Classical Laminate Theory calculations.

The grade used was GLARE 3-3/2-0.3, composed by the layout: [Al/90/0/Al/0/90/Al], with three 0.3mm thick aluminium sheets, intercalated with two glass fiber layers. The GFRE constituent material is made of FM94 epoxy resin, that cures at 120°C, reinforced by unidirectional high strength S2 glass fibers with a fiber volume content between 52% and 72% [5]. Table 1 presents the material properties of the constituents of GLARE, on a ply-level and of GLARE 3-3/2-0.3, on a laminated level. This material shows a longitudinal membrane stiffness (A_{11}) of 88.56 GPa.mm. The stiffness and strength of GLARE is therefore tailored by the type of prepreg material, composition, stacking sequence and thickness of the laminate.

Typically, the failure mechanism of GLARE 3, under quasi-static tensile loading and assuming isostrain conditions, is as follows: at an engineering strain of ~0.5%, the aluminium starts to plastically deform and to redistribute the stresses to the adjacent GFRE plies. For an increasing applied load, damage will eventually start as matrix cracking that may coalesce into delaminations; further increasing the load will lead to the ultimate failure of the laminate, at a strain of ~4.5% [6], due to glass fiber breakage of the 0° oriented layers.

Three 3.5mm thick layup configurations, each containing 28 GFRE plies, were structurally assessed for panel design (specifically in the slot region). The following list presents their layup configurations together with the longitudinal membrane stiffness and elastic modulus values:

- A: [90/0/90/0/90/0/90/0/90/0/90/0]s; A_{11_A} = 110.9 GPa.mm; E_{m1_A} = 31.47 GPa;
- B: [0/90/90/0/90/0/90/90/0/90/0/90]s; A_{11_B} = 99.8 GPa.mm; E_{m1_B} = 28.31 GPa;
- C: [90/0/0/90/0/90/0/0/90/0/90/0]s; A_{11_C} = 122.0 GPa.mm; E_{m1_C} = 34.61 GPa.

3. MECHANICAL STATIC TESTING OF STRUCTURAL ELEMENTS

The structural behavior and strength of aerostructures is assessed through a series of tests of increasing size, cost, time and complexity, represented by the ‘building block’ approach (also known as ‘testing pyramid’- Figure 4). This comprehensive and systematic methodology sets a logical framework for airworthiness qualification and structural integrity demonstration. In other words, it is the backbone of aerostructures certification [7].

For the ACASIAS project, the first three levels of the pyramid were considered:

- 1) Coupon - material properties such as strength values and elastic properties are extracted and used to calibrate the material model;
- 2) Structural elements - empirical ‘knock-down factors’ are derived, related to environmental, scatter and damage effects; in addition, the global structural behavior and strength data are determined and can be used as design values;
- 3) Details [see test panel - Figure 1 b)] - the structural performance of the FEA predictions are compared against experimental tests of a much representative test specimen and a thorough structural understanding is reached. Testing at panel level is currently ongoing and will be reported in a future paper.

The present article will solely focus on the Mechanical Static Testing (MST), at the structural element level, in tensile conditions. All tests were performed at VZLU in Prague.

3.1 Test description and test matrix

The structural elements were tested in displacement-controlled conditions at a rate of: 1mm/min (*i.e.* in quasi-static conditions), thus avoiding time-dependent effects.

Three layup configurations (A, B and C) were tested in different ambient conditions (Table 2): a) Room Temperature Ambient (RTA, at ~23.5°C); b) Cold Temperature Ambient (CTA, at -55°C); c) Hot Temperature (dry) Ambient (HTA, at 60°C and 80°C); d) Hot Temperature Wet (HTW, at 60°C and 80°C in water saturated conditions). Additionally, for some ambient settings, the effect of damage was investigated by applying, in the designated specimens, a 30J impact at a multiple ply-drop location (Figure 5).

Table 2 also mentions structural elements that included an integrated Flexible Printed Circuit Board (Flex-PCB) to assess its effects in the structural performance of the specimens and the repercussions of high load introduction in the electrical continuity of the wires. However, the scope of the present article does not encompass those results.

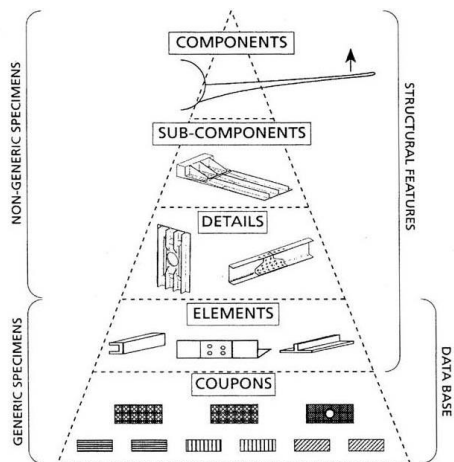


Figure 4: Aerostructures testing pyramid.

Table 2: Structural element test matrix.

Conf.	RTA [~23.5°C]		CTA [-55°C]		HTA[60°C]		HTW[60°C]	
					HTA[80°C]		HTW[80°C]	
	Pris.	Imp.	Pris.	Imp.	Pris.	Imp.	Pris.	Imp.
A	2	1	2	-	1	-	1	1
					1	-	1	1
B	2(1)	1(1)	2	-	1	-	1	1
					1(1)	-	1	1
C	2(1)	1(1)	2	-	1	-	1	1
					1(1)	-	1	1
Total	6(2)	3(2)	6	-	6(2)	-	6	6

Note: PCB-integrated structural element indicated in parentheses.
Pris. stands for Pristine and Imp. stands for impacted.

3.2 Structural element specimens and instrumentation

The structural element specimens were 700mm long by 100mm wide (Figure 5). The effective length of the specimen was 590mm, provided that the gripping length on each end was 55mm long.

Global load-displacement and localized strain data were acquired by the use of the instrumentation contained and described in Table 3. The exact location of the strain gauges is shown in Figure 5.

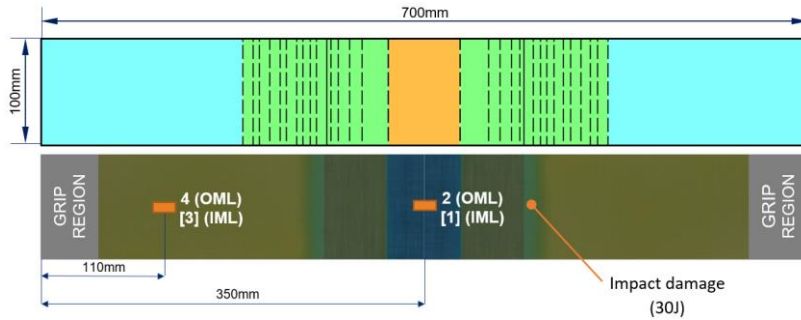


Figure 5: Structural element test specimen - OML view: drawing showing material regions (top) and photo with specified strain gauge, grip and impact locations (bottom).

Table 3: Instrumentation used in the MST.

Data description:	Sensor:
Applied load [N]	Load cell
Global displacement [mm]	Acting piston
Localized strains	4x Strain gauges (longitudinal) at specified locations
Inplane strain field and out-of-plane deflection	2x DIC cameras at OML surface
40,000 fps video of failure	High speed camera

4. RESULTS AND DISCUSSION

4.1 Structural element load-displacement for different ambient conditions

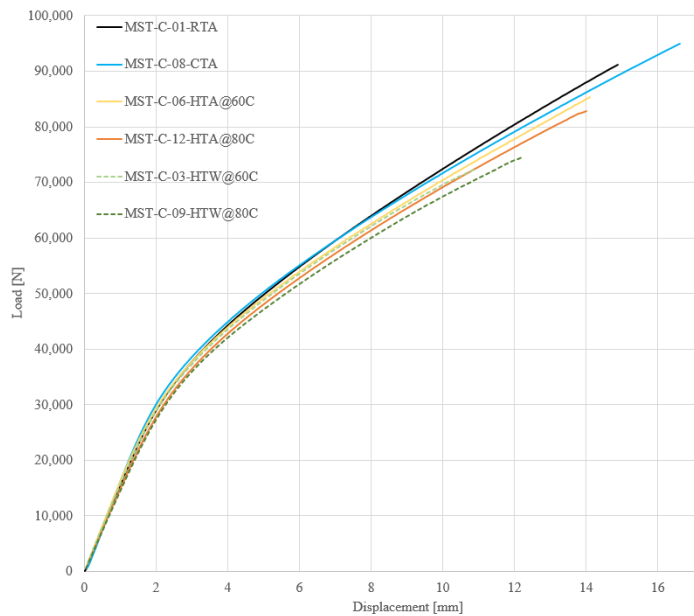


Figure 6: Load-displacement curves of C-configuration structural element specimens tested at different ambient conditions.

Figure 6 shows the load-displacement curves for C-layup configuration specimens in different ambient conditions. In the elastic region, the structural behavior was very similar in all cases, with small differences in stiffness (~13% between CTA and HTW@80°C). After the yielding point, the stiffness changes became slightly more noticeable, with a stiffer and stronger structural behavior for decreasing temperature and water content; except for the specimen in CTA, which showed to be more compliant than the specimen in RTA after yielding.

The global behavior and strength of the structural element is dominated (yet, not identical) by GLARE structural properties.

4.2 Experimental vs. numerical stress strain curves for GLARE and GFRE regions

Ongoing simulations² carried out by CIMNE [8] [in grey and in black, for GFRE and GLARE regions, respectively - Figure 7 a)] show a very good agreement with the strain gauge data and DIC results, particularly for GLARE. Differences between GFRE strain gauge readings on the OML and IML surfaces indicate that the specimen deflected due to bending. From DIC, the measured out-of-plane displacement in the center was of $\sim 1.45\text{mm}$ (in the positive normal direction of the OML plane). This secondary bending behavior originates due to the laminate's asymmetrical build-up, which induces load-path eccentricities.

GLARE 3 elastic modulus extracted by the DIC results was of $\sim 54.5\text{ GPa}$ which is $\sim 6.2\%$ lower than the theoretically determined, through Classical Laminate Theory (CLT) of 58.1 GPa (see Table 1). Yielding was determined by processing the DIC data and assuming the commonly used 0.2% offset strain as the criterion: the found yield value was of $\sim 259\text{ MPa}$, which is $\sim 3.8\%$ lower than the theoretical value of 269.3 MPa , calculated by using the rule of mixtures³ by combining the individual yield values present in the internal Technical Handbook (TH) [5].

Regarding the ultimate strength, the load cell measured a maximum value of 91.23 kN , which in terms of average engineering stress is equal to 651.6 MPa , *i.e.*, $\sim 3.0\%$ higher than the computed theoretical value of 632.5 MPa (using the same method as for the yielding - Table 1).

The longitudinal engineering strain field is presented in Figure 7 b), which shows a more compliant behavior of GLARE 3 against a much stiffer behavior of the thicker GFRE, justified by the lower longitudinal membrane stiffness of $88.56\text{ GPa}\cdot\text{mm}$ against $122.0\text{ GPa}\cdot\text{mm}$.

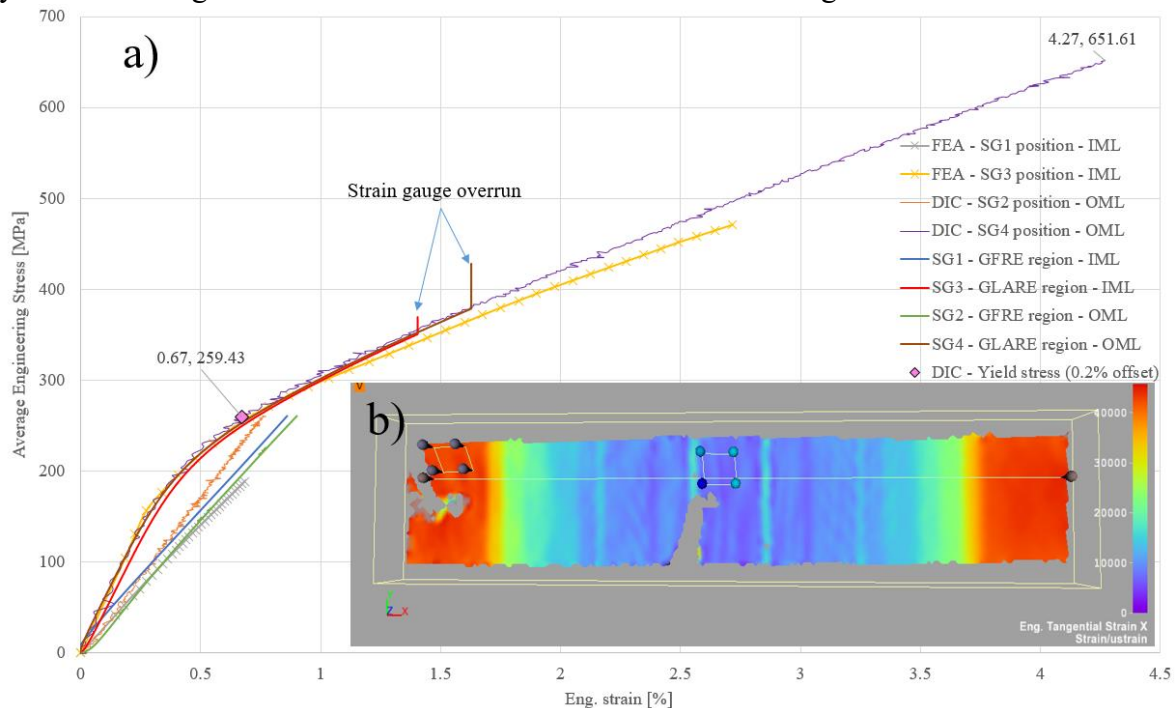


Figure 7: a) Stress-strain curves for: FEA predictions, DIC and strain gauge measurements; at GLARE and GFRE regions of test specimen MST-C-01; b) Longitudinal engineering strain field at maximum load.

² The last data point in CIMNE simulations does not represent failure, but an interrupted simulation due to lengthy convergence attempts.

³ The rule of mixtures rely on the assumption that the mechanical properties of the material can expressed by simple linear functions of the metal volume fraction.

4.3 Overview on the maximum loads and failure modes

Having the dry RTA condition as a reference, the maximum load bar chart (Figure 8) shows a ~11.8% strength decrease for a dry specimen tested at 80°C. The drop in strength due to saturated conditions was of ~12.2% and ~11.2% for specimens, at 60°C and 80°C, respectively, when directly compared to their dry counterparts. An impact of 30J did not seem to affect the strength of the tested samples, as the decrease in average strength was always lower than 1.5%.

Out of the 33 tested specimens, all failed in GLARE net cross-section: 16 of those failed at the first ply-drop (due to the stress concentration effect); seven, somewhere in thinnest GLARE region; and ten failed in the gripping region (including all six CTA specimens). This means that 70% of the specimens failed as intended, in the well-studied GLARE region. To mitigate the occurrence of the undesired gripping failure, subsequent tests will include tapered tabs.

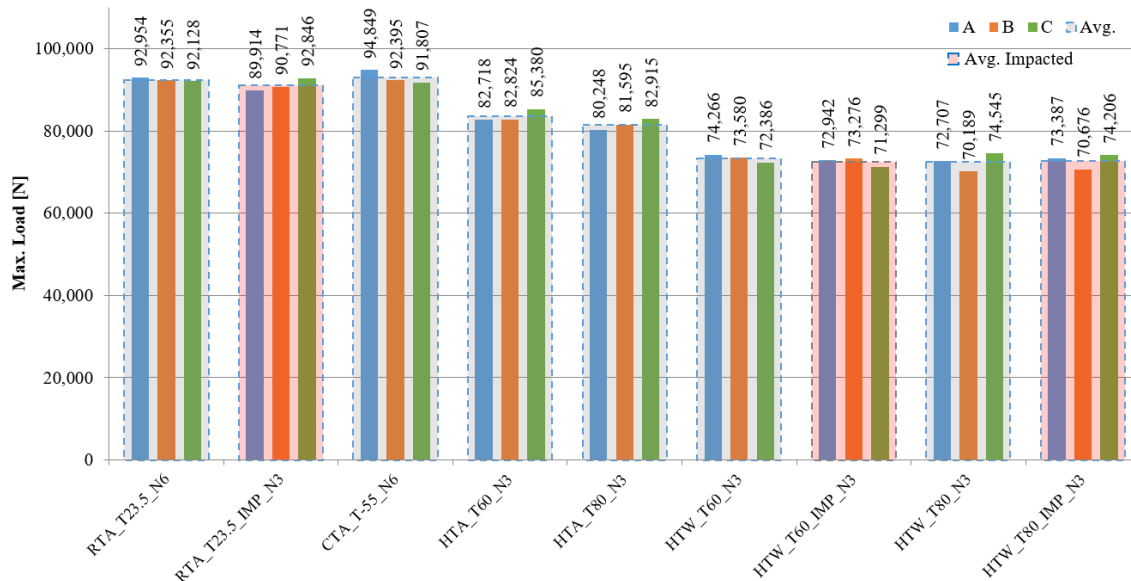


Figure 8: Maximum load for A, B and C layup configurations tested in different ambient conditions. Category coding: [Ambient conditions]_T[Temperature]_N[Sample size].

5. CONCLUSIONS

This paper aimed to assess the structural behavior of an integrated slot antenna in a GLARE fuselage panel. From the result analysis of an experimental campaign carried at the structural element level, in quasi-static tensile conditions, the following conclusions were drawn:

- Design values found in internal technical handbooks seem to predict very accurately (~2.9% lower) the found failure load in GLARE. Additionally, CIMNE early simulations seem to accurately predict the behavior of the structural elements. The following numerical stress analysis work should focus on predicting damage initiation and ultimate failure.
- The structural elements behavior is dominated by GLARE; moreover, the stiffness and strength of the structural elements are barely affected by layup configuration, impacting damage (<1.5% weaker than pristine counterparts), temperature (~11.8% weaker than RTA counterparts) and water content (~11.2% weaker than dry counterparts).
- The dominant failure mode was net-cross section in GLARE, particularly in the intended first ply-drop (16/33 specimens) due to the stress concentration. Provisions were taken to avoid gripping failure in next testing stages, as the inclusion of tapered tabs.

ACKNOWLEDGEMENTS

We thank our production colleagues from GKN-Fokker and VZLU for the dedication and provided support in the manufacturing and testing of the test specimens that made possible the obtainment of the presented results.

This project has received funding from the European Union's Horizon2020 research and innovation programme under grant agreement No.723167.

REFERENCES

- [1] J. Rotgerink, C. Heuts, J. Verpoorte and C. van Hengel, "VHF antenna integrated into a classical fibre metal laminate fuselage panel.," in *European Conference on Multifunctional Structures*, Barcelona, 2020.
- [2] G. Wu and J. Yang, "The Mechanical Behavior of GLARE Laminates for Aircraft Structures," *Journal of the Minerals, Metals and Materials Society*, pp. 72-79, 2005.
- [3] R. Alderliesten and J. Homan, "Fatigue and damage tolerance issues of Glare in aircraft structures.," *International Journal of Fatigue*, vol. 28, pp. 1116-1123, 2006.
- [4] R. Citarella, E. Armentani, R. Sepe and F. Caputo, "FEM Simulation of a FML Full Scale Aeronautic Panel Undergoing Static Load," *Industrial Engineering & Management*, vol. 3, no. 1, 2014.
- [5] Fokker Aerostructures, "TH3-305 - Material design values and mechanical properties of standard GLARE," Papendrecht, 2006.
- [6] M. Hagenbeek, "Characterisation of Fibre Metal Laminates under Thermo-mechanical Loadings," TU Delft, Delft, 2005.
- [7] University of Bristol, "Certification for Design - Reshaping the Testing Pyramid," UK Research and innovation, Swindon, 2020.
- [8] F. Turon, F. Otero and X. Martinez, "Structural analyses of GLARE-GFRP transition for integrated VHF antenna on a fuselage panel," in *European Conference on Multifunctional Structures*, Barcelona, 2020.

VHF ANTENNA INTEGRATED INTO A CLASSICAL FIBRE METAL LAMINATE FUSELAGE PANEL

EMUS 2020

J. LANSINK ROTGERINK^{*}, C. HEUTS[†], J. VERPOORTE^{*} AND C. VAN HENGEL[‡]

^{*} Royal Netherlands Aerospace Centre (NLR)
Voorsterweg 31, 8316 PR Marknesse, The Netherlands
e-mail: Jesper.Lansink.Rotgerink@nlr.nl, <http://www.nlr.nl>

[†] GKN Fokker Elmo
Aviollandalaan 33, 4631 RP Hoogerheide, The Netherlands
email: Charly.Heuts@fokker.com, <http://www.gknaerospace.com>

[‡] GKN Fokker Aerostructures
Industrieweg 4, 3351 LB Papendrecht, The Netherlands
Email: cees.vanhengel@fokker.com, web page: <http://www.gknaerospace.com>

Key words: Integrated slot antenna, VHF, parallel plate resonator, antenna miniaturization, bookleafing

Abstract. Replacement of protruding antennas by integrated alternatives will reduce the energy consumption and NO_x and CO₂ emissions of an aircraft. This paper proposes and integrated VHF cavity backed slot antenna that is suitable to replace blade antennas. To reduce the size of the cavity a parallel plate resonator is used. The slot is integrated into a fibre metal laminate fuselage panel. A bookleafing principle is used to reinforce the panel at the position of the slot, making sure the material quality is not reduced. Measurement results of a demonstrator antenna show the feasibility of the proposed antenna. Moreover, the paper discusses several electromagnetic and structural design trade-offs for this integrated antenna.

1 INTRODUCTION

Challenges set by the European Union to reach Flightpath 2050 climate goals require innovative solutions to reduce the energy consumption of aircraft. One of the focusses of the ACASIAS project is the replacement of protruding antennas on an aircraft by integrated alternatives. Specifically, this paper discusses replacement of a conventional blade antenna used for very high frequency (VHF) communications by slot antennas that are integrated in fibre metal laminate (FML) panels. Such integration of antennas in fuselage panels will reduce the aerodynamic drag and consequently the energy consumption of an aircraft.

The intention is to integrate a slot antenna into an FML fuselage panel. However, radiation of this slot antenna into the interior of the aircraft has to be prevented. Conventionally this is resolved by placing a cavity with a depth of a quarter wavelength behind the antenna. At the frequency band of the targeted blade antenna, centred around 125 MHz, this would imply an integrated antenna with a thickness up to 60 cm, which is unacceptable. Therefore, cavity miniaturization techniques are required to minimize the thickness of the antenna without

degrading the antenna performances. High-permittivity dielectric materials can be used, but these also generally have high mass densities. In [1]-[3] high impedance surfaces (HIS) are used to minimize the thickness of the antenna. The disadvantage of such a technique is the required space parallel to the fuselage to place the amount of HIS elements for the HIS to work properly [4]. At VHF frequencies this implies a HIS width that would not fit in between the stringers of an aircraft. Therefore, in this paper a parallel plate resonator (PPR) technique is used [5]. In a PPR the required quarter wavelength distance from the slot to a reflection plane is transformed into a folded waveguide structure, thereby reducing the thickness of the antenna. In contrast to the dual-resonator box in [5], in this paper a single-resonator PPR is used to further decrease the weight of the antenna. Several design trade-offs of such a PPR slot antenna are discussed, which include the use of dielectric materials to reduce the dimensions (but might increase weight), as well as bandwidth (BW) versus gain trade-offs.

Apart from these electromagnetic (EM) challenges the integration of a slot antenna into an FML panel raises clear structural challenges. Basically, this integration implies the creation of a hole in the skin of an aircraft, by which the strength of the skin is reduced. On top of that, the corners of the slot antennas can cause build-up of stresses. Therefore, the skin needs to be locally reinforced. In this paper, a so-called bookleafing method is proposed to make the transition from a conventional FML layup to a thicker piece of pure glass fibre below the slot antenna, back to conventional FML.

Section 2 discusses the EM design of the antenna, while section 3 covers the structural challenges caused by the integration. Section 4 discusses some important design trade-offs. Section 5 gives results for a demonstrator antenna and conclusions are given in section 6.

2 ELECTROMAGNETIC ANTENNA DESIGN

The proposed VHF antenna consists of three different parts: the slot antenna, the parallel plate resonator and the feed structure. All three are discussed in this section.

2.1 Slot antenna

One of the main advantages of a blade antenna, a monopole type antenna, is its nearly omnidirectional radiation. A slot antenna is the dual of a dipole antenna: a rectangular hole in a metallic ground plane. It radiates efficiently if its length is half a wavelength. Its feed induces currents in the ground plane that are enforced to flow around the slot. This causes radiation in a pattern that is again nearly omnidirectional, with only a null in the longitudinal direction of the slot. This makes a slot antenna very suitable for replacing the blade antenna.

As mentioned, the optimal length of the slot antenna is roughly half a wavelength. This implies that changing the surrounding medium of the slot will also change the optimal length of the slot. When the entire surrounding space is replaced by material of relative permittivity ϵ_r then the length of the slot is reduced by a factor equal to the square root of that permittivity. When part of the surrounding medium is different from air, the optimal length can be found through simulations (in our case the full-wave software Feko was used). The resonance frequency of the slot can be found by simulation with an ideal source at the position where the real part of the slot impedance is maximal and the imaginary part crosses zero. Once the optimal slot length has been found, the PPR is added and its dimensions optimized.

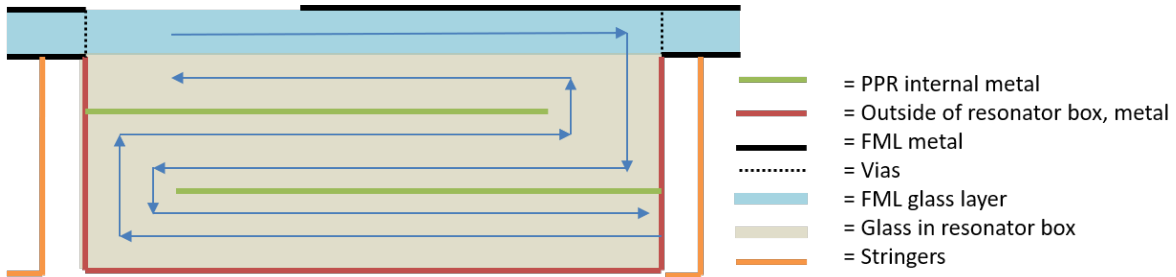


Figure 1: Illustration of a cross-section of a slot antenna integrated in FML, with PPR attached. The FML is in this case illustrated without detailed layer build-up. This will follow in section 3.



Figure 2 Transition from FML to «full glass» GFRP to FML (concept)

2.2 Parallel plate resonator

To prevent radiation of the slot antenna into the aircraft interior, a cavity will need to be attached to the interior side of the slot antenna. To reduce the size of such a cavity a parallel plate resonator is used, of which the concept is explained in detail in [5]. In general, the PPR is a structure in which the required distance of a quarter wavelength from slot to short-circuit is covered in a folded waveguide (see Figure 1). Following the blue arrows in Figure 1 the EM waves entering the PPR travel half a wavelength before returning to the slot, ensuring that these waves leave the slot in phase with the waves that directly radiate to the exterior of the fuselage. Thus, the length of the PPR channel should be equal to a quarter of the wavelength inside the PPR, which is the guided wavelength:

$$\lambda_g = \frac{c}{f} \frac{1}{\sqrt{1 - \left(\frac{c}{2wf}\right)^2}} \quad (1)$$

Here c is the wave velocity in the medium of the PPR, f is the frequency and w is the length of the PPR in the dimension orthogonal to the cross-section shown in Figure 1.

The design of a PPR depends on a large number of parameters, such as the total length of the channel, the height of the channel, material properties, the length of the plates internal to the PPR box and even the dimensions of the slot. In general, the recipe is to first design the proper slot dimensions, after which the PPR dimensions can also be tuned by using an ideal source. Once the slot and PPR are tuned such that the resonance is at the correct frequency, the feed structure should be added to tune the overall antenna behavior.

2.3 Antenna feed

Feeding the slot antenna is done by a microstrip feed that extends over the slot. For optimal matching the correct feed position should be found. For a slot antenna, the impedance is high in the centre of the slot and zero at the end of the slot. The optimal feed position is the position at which the real part of the slot impedance matches the impedance of the microstrip feed. As in [5], here a 50Ω feed and a 100Ω stub is chosen. The stub is the part of the feed

that extends behind the slot. By tuning the length of the stub the imaginary part of the input impedance of the slot will be counteracted. The antenna and feed are well matched if the reflection coefficient of the source is as low as possible, but at least lower than -6 dB. The higher the frequency band over which this condition holds, the higher the bandwidth of the antenna. This bandwidth can be improved by optimizing the feed and stub to introduce a second resonance [6]. By placing this resonance close to the original slot resonance the bandwidth can be enhanced. As a final solution to optimize the bandwidth of the antenna a matching network can be used to improve the matching of the antenna. This matching network is formed by lumped inductances and capacitances and is used to get rid of slight mismatches between the antenna and source impedances.

3 STRUCTURAL REINFORCEMENTS BY BOOKLEAFING PRINCIPLE

The need to create a slot in the metallic layers to act as antenna causes a significant issue for the structural performance of the basic skin material, because it removes about 64% of the load carrying material. The skin is a Glare3-3/2-0.3 material, meaning that it consists of 3 metal layers (interspersed with 2 composite layers: hence 3/2) of 0.3 mm thickness. In Glare 3, each composite layer consists of one 0 and one 90 degrees-oriented glass fibre prepreg ply of 0.127 mm thickness each. Thus, at the slot, the removal of 3 x 0.3mm removes 0.9 mm of the total thickness of 1.4 mm. Such a material “thinning” would result in an unacceptable stress increase degrading the structural performance. To restore the stress level to acceptable levels, additional glass fibre layers are added according to proprietary rules to the existing ones. In a way, this solution is similar to a so-called “patch repair” as commonly used in composite structures. However, in this case the additional “repair” plies are added by a “bookleafing” principle (see Figure 2) thereby avoiding local stress concentrations. Secondly, the “repair” is manufactured using the normal manufacturing process, including autoclave curing and C-scan Ultrasonic quality inspection. Therefore, unlike in a repair situation, the material quality is identical to that of the undisturbed laminate. Further details on the structural aspects of this antenna are discussed in other EMUS2020 papers.

4 DESIGN CHALLENGES

The design of the integrated VHF slot antenna provokes various design challenges, most of which being trade-offs in structural and EM antenna performances. One of the main design criteria is the overall weight of the antenna, including structural reinforcements and PPR. This introduces several trade-offs, for instance when minimizing the thickness (i.e. weight) of the PPR. Reduction of the thickness comes at the cost of the antenna performance, e.g. for a thinner antenna it becomes harder to obtain low S_{11} results over a large bandwidth. Another trade-off that is largely dominated by the weight and overall dimensions of the antenna, is the choice of material for the PPR interior. An air-filled PPR seemed to yield better S_{11} results in simulations. Additionally, its weight will be minimal, however the required size of the slot is higher, giving rise to extra weight in terms of structural reinforcements. Moreover, for a larger PPR it will be more challenging to fit between the frames and stringers of an aircraft. Within the ACASIAS project the choice was made to create two versions of a dielectric filled PPR, a thick and thin one, to demonstrate corresponding weight vs. antenna performance trade-offs.

The feeding structure also introduces tradeoffs. Ideally, the feed is integrated into the PPR.

However, this would make replacing the feed in case of a damage (due to for instance lightning) very hard. Therefore, in the demonstrator discussed in the next section a very thin FlexPCB feed was placed on the outside of the fuselage panel. Finally, also the use of a matching network introduces trade-offs. Such a network can improve the matching, but usually this comes at the cost of gain. However, in this case it is expected that the benefit for bandwidth is much more than the loss of gain.

5 DEMONSTRATOR RESULTS

Based on the theoretical designs obtained by simulations and several trade-off choices that were made in the ACASIAS consortium, a demonstrator integrated VHF antenna was built and measured. A parallel plate resonator was manufactured from PCB material. Two different PPRs were manufactured, named the ‘thick PPR’ and the ‘thin PPR’, the difference being the channel thickness. The overall thickness of the thick PPR is $0.07\lambda_0$ (or 16.8 cm), while for the thin PPR the thickness was $0.014\lambda_0$ (or 35 mm). Both PPRs were made up out of multiple PCB layers of 3.5 mm thickness. The substrate material was FR4, while the parallel plates were formed by copper ground planes on the PCB substrate. GKN Fokker Aerostructures manufactured an FML panel with a slot following the bookleafing principle introduced in section 3. Pictures of the FML panel with slot and the thin PPR are shown in Figure 3.

An Agilent E8386B VNA was used to measure the S_{11} of the FML slot antenna including PPR. FlexPCBs manufactured by Trackwise were used to feed the antenna. Resulting S_{11} for the thick PPR is shown in Figure 4a. This clearly shows the double resonance behavior that is intended to optimize the bandwidth of the antenna. In this case, the -6 dB BW is roughly equal to 13% (120–136.2 MHz). For the thin PPR the measured S_{11} results shown in Figure 4b illustrate that decreasing PPR thickness reduces the antenna matching. The blue line shows higher S_{11} levels than for the thick PPR and the -6 dB bandwidth in this case is only 8.7%. However, the red line indicates what can be obtained when using a matching network. The reflection coefficient is greatly improved, yielding a -6 dB BW of 22% (120.9–148.5 MHz).

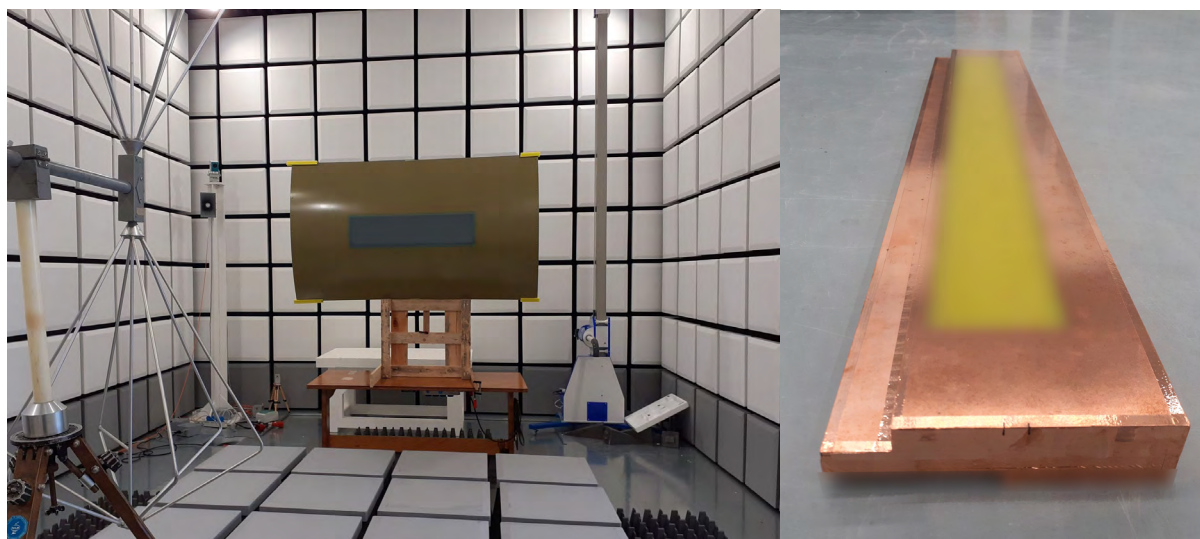


Figure 3: Pictures of (a) (left) the VHF antenna integrated into FML panel in radiation pattern test set-up, and (b) a close-up of the thin PPR manufactured from PCB material (details are blurred due to confidentiality).

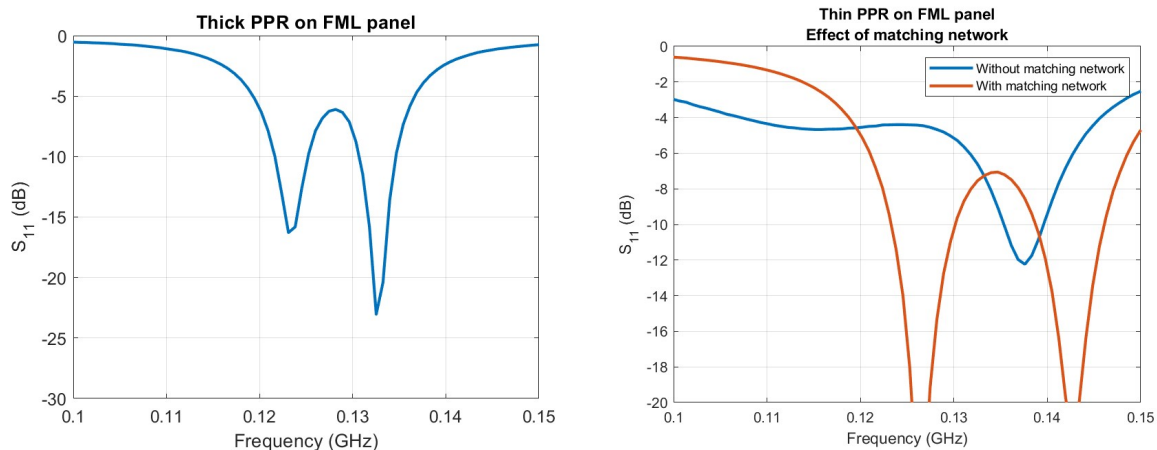


Figure 4: Measured S_{11} for the slot integrated into an FML panel with (a) (left) a thick PPR, and (b) a thin PPR without (blue line) and with (red line) matching network.

6 CONCLUSIONS

This paper presents the design of an integrated VHF slot antenna with parallel plate resonator. The principles of EM design are explained, including slot antenna, microstrip feed and PPR. A bookleafing principle is applied to realize local reinforcements in the area of the slot antenna. This ensures that the structural quality of the FML panel with integrated antenna is not degraded. The antenna design faces several EM and structural trade-offs, of which some of the most important ones are discussed in this paper. Two demonstrator antennas were manufactured, with which some trade-offs can be illustrated. The measured results of these demonstrators show one $0.07\lambda_0$ thick antenna working from 120–136.2 MHz (13% -6 dB BW) and one $0.014\lambda_0$ thick antenna with matching network working from 120.9–148.5 MHz (22% -6 dB BW). This proves the feasibility of the presented integrated VHF slot antenna.

ACKNOWLEDGEMENTS

This project has received funding from the European Union’s Horizon2020 research and innovation programme under grant agreement No.723167.

REFERENCES

- [1] D. Sievenpiper, L. Zhang, R.F. Jimenez Broas, N.G. Alexopoulos, E. Yablonovitch, “High-impedance electromagnetic surfaces with a forbidden frequency band”, *IEEE Trans. on Antennas and Prop.* (1999), **47** (11): 2059-2074.
- [2] J. Joubert, J.C. Vardaxoglou, W.G. Whittow and J.W. Odendaal, “CPW-fed cavity-backed slot radiator loaded with an AMC reflector”, *IEEE Trans. on Antennas and Prop.* (2012), **60** (2): 735-742.
- [3] H. Malekpoor and S. Jam, “Improved radiation performance of low profile printed slot antenna using wideband planar AMC surface”, *IEEE Trans. on Antennas and Prop.* (2016), **64** (11): 4626-4638.
- [4] J. Li, H. Shi and A. Zhang, “Unidirectional circularly polarized slot antenna backed with miniaturized AMC reflector”, *IEEE Int. Symp. on Antennas and Prop. & USNC/URSI*

Nat. Radio Sc. Meeting, Boston, MA, USA, July 2018.

- [5] W. Hong and K. Sarabandi, "Platform embedded slot antenna backed by shielded parallel plate resonator", *IEEE Trans. on Antennas and Prop.* (2010), **58** (9): 2850-2857.
- [6] N. Behdad and K. Sarabandi, "A wide-band slot antenna design employing a fictitious short circuit concept", *IEEE Trans. on Antennas and Prop.* (2005), **53** (1): 475-482.

VHF COMMUNICATION ANTENNA INTEGRATED INTO AN AIRCRAFT WINGLET

EMUS 2020

M. MARTÍNEZ-VÁZQUEZ¹, Z. ŘEZNÍČEK², S. STEEGER³,
P. VRCHOTA⁴, V. LUNGAHO⁵

¹ IMST, GmbH
Carl-Friedrich-Gauß-Str. 2-4
47475 Kamp-Lintfort, Germany
e-mail: Martinez@imst.de, www. www.imst.com

² Evektoř, spol. s r.o.
Engineer. Services Division, Letecká 1008
686 04 Kunovice, Czech Republic
email: zreznicek@evektor.cz, www.evektor.cz

³ INVENT, GmbH
Christian-Pommer-StraÙe 34
38112 Braunschweig, Germany
email: Stefan.Steeger@invent-gmbh.de, www.invent-gmbh.de

⁴ Czech Aerospace Research Centre (VZLU)
Beranovych 130
199 05 Prague, Czech Republic
email: vrchota@vzlu.cz, www.vzlu.cz

⁵ Trackwise Designs plc
1 Ashvale Alexandra Way, Ashchurch, Tewkesbury
Gloucestershire, England
email: victor.lungaho@trackwise.co.uk, www.trackwise.co.uk

Key words: VHF antenna, Computational Electromagnetics, Winglet, Aircraft

Abstract. The article is discussing the final design of a VHF communication antenna integrated in a composite winglet of the EV-55 small transport aircraft. The antenna is designed to operate in the VHF band reserved for civil aviation, 117.975 – 137 MHz with optimal VSWR below 2.5. Compared with a standard vertically polarized monopole antenna, the radiation pattern in the horizontal plane shall not be down more than 6 dB and vary more than 6 dB [2].

1 INTRODUCTION

Designers of modern winglets are trying to introduce more functionalities into a winglet structure nowadays. This is also the case for the ACASIAS project [1], where one of the systems to be developed is a VHF antenna integrated into the winglet.

Such a design usually represents a complex and multidisciplinary task, especially due to specific technical trade-offs and bottlenecks originating from the following three distinctive engineering areas: aerodynamics, stress analysis and electromagnetics [3].

From the antenna point of view, several challenges have been faced during the design: final physical dimensions of the winglet and the VHF antenna are relatively small compared to target wavelengths ($\lambda \approx 2 - 2.5$ m). Integration of the antenna into such a small area may easily become a challenging task focused on finding more spatially effective solutions without sacrificing necessary performance. In addition, some requirements specified for airborne VHF systems are in favour of standard monopole-like solutions installed on top or bottom of an airplane fuselage, where omnidirectional radiation pattern is preferred in horizontal plane. Such a requirement can be discriminating for the antenna situated at the tip of a wing due to obstructions caused by an airplane. In addition, winglet parts tend to attract lightning strikes more easily. Therefore, more stringent protection of the antenna and all related systems should be taken into account.

2 ANTENNA DESIGN

2.1 Winglet with integrated notch antenna

The final geometry of the winglet is depicted on Figure 1. The chosen concept is a notch antenna [4] printed on a thin, flexible PCB sandwiched in the foam filling of the winglet. The open side is tapered for broadband matching. The outer skin of the winglet is made out of Carbon Fibre Reinforced Plastic (CFRP) with an expanded copper foil at the external layer, so that a Glass Fibre Reinforced Plastic (GFRP) “window” was scarfed on the winglet skin to allow the antenna to radiate.

All simulation models discussed in the paper were prepared and analyzed in CST MWS. The protected CFRP material was modelled once as a sheet resistance (FD solver; $RS = 0.05 \Omega/\text{sq}$ at 100 MHz) and once as a multilayered thin panel (TD solver; $\sigma \approx 10\text{k S/m}$, $t = 2$ mm).

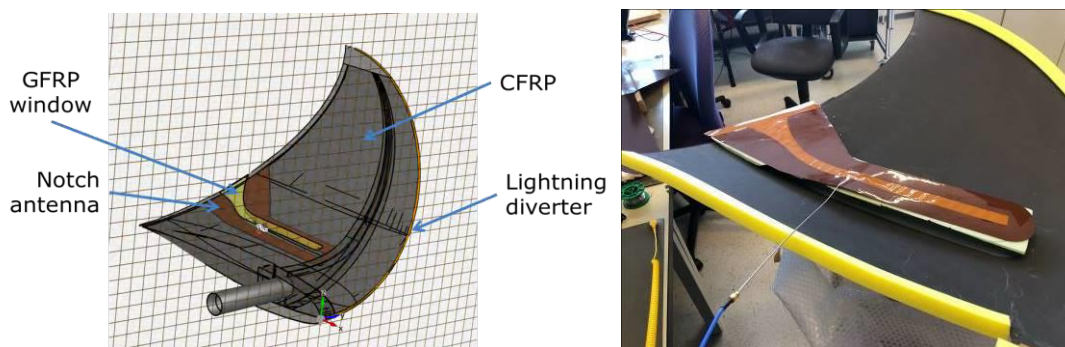


Figure 1: EV55 winglet with integrated notch antenna: structural model (left) and prototype (right)

2.2 Preliminary measurements

A half-opened model of the winglet structure (Figure 1) was used for a preliminary characterization of the integrated notch antenna’s properties. During the measurement, a semi-rigid coaxial cable has been used as a feeding line and the final position of the feeding port was 240 mm from the end of the notch. The measured and simulated reflection coefficients for two different feeding points and computational methods are presented in Figure 2.

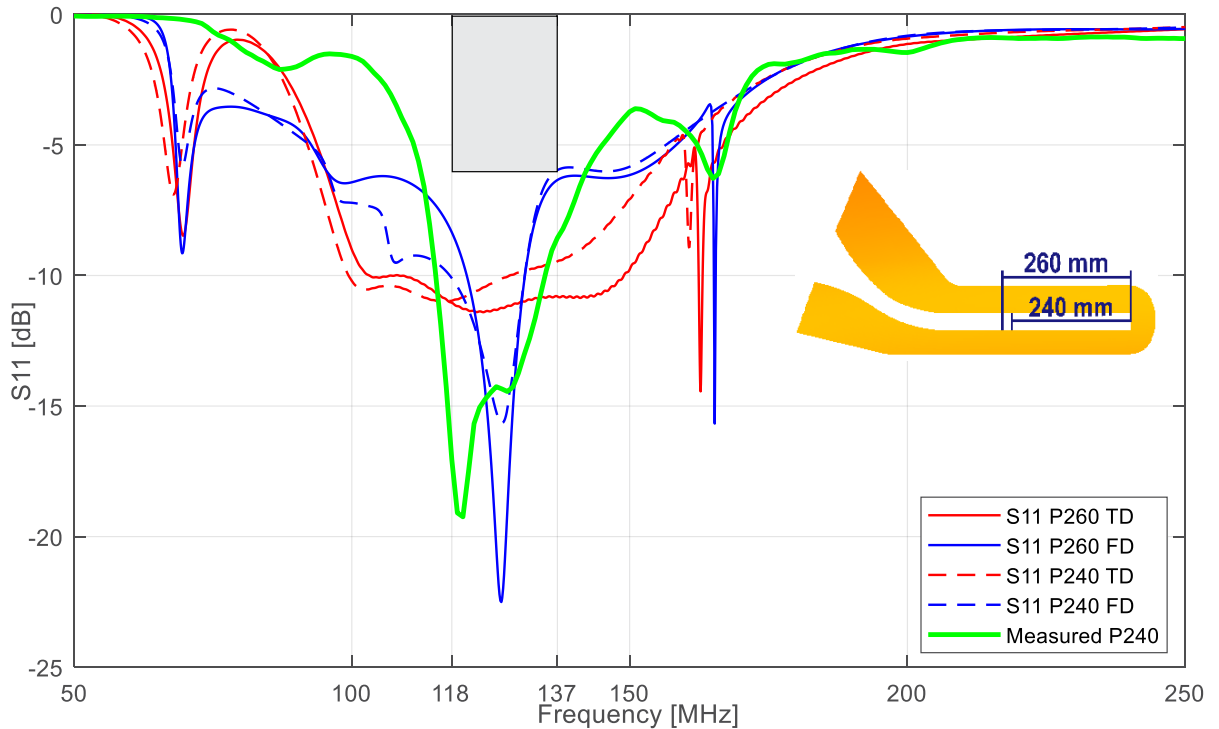


Figure 2: Comparison measured and simulated S11 results

In both cases, good results were obtained concerning the antenna matching and necessary bandwidth. The minimal requirement to $VSWR \leq 3$ is satisfied in all cases. The optimal $VSWR < 2.5$ is fully achieved for the measured prototype and simulation models analyzed in time domain (TD). Differences in material models used in TD and FD models were ruled out as a potential source of S11 discrepancies. It seems that observed deviations in impedance behavior of the antenna are directly related with different computational methods and used types of mesh.

The antenna port position P240 seems to be less optimal than the P260. This is why all simulation models discussed in the following chapter will be related to the P260 position. The final location of the feeding port will be verified by additional measurements to be carried out on a fully enclosed winglet prototype. In any case, the impedance matching of the antenna can be further improved by matching circuits like L-C networks or via a balun.

3 ANTENNA INSTALLED ON EV-55 AIRCRAFT

3.1 Radiation efficiency of installed antenna

According to [2], the field strength of an airborne VHF antenna shall not be down more than 6 dB and vary more than 6 dB in comparison with a standard vertically polarized monopole antenna. Naturally, the radiation pattern of an installed antenna may differ with respect to a specific position on an airplane. Compared to the standard case when an antenna is installed on a fuselage (i.e. relatively uniform and large ground plane), this verification is especially important when it comes to the VHF antenna integrated inside a winglet. Therefore is useful to verify if the antenna is performing well at the place of its installation.

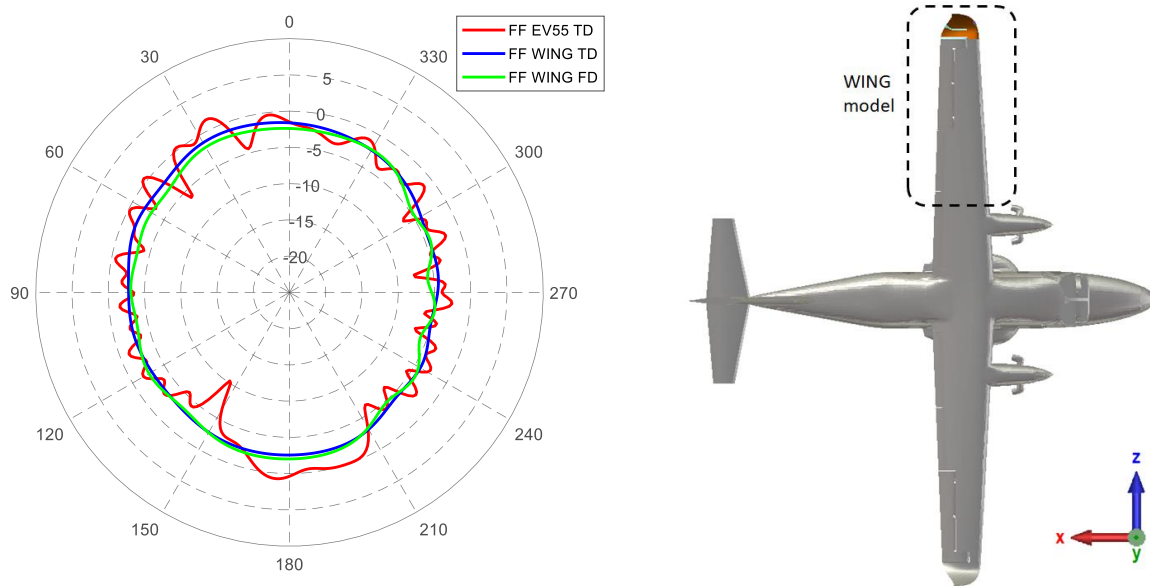


Figure 3: Antenna gain (vertical comp.) for different simulation scenarios ($\Phi = 0^\circ, \Theta = 0^\circ - 360^\circ$)

Table 1: Comparison of resulting gain parameters for different simulation scenarios

Model / solver:	Maximum [dBi]	Average [dBi]	Minimum [dBi]
EV-55 / TD	1.5	-2.3	-10.0
WING / TD	-1.1	-2.7	-5.0
WING / FD	-1.8	-3.1	-5.9

Radiation efficiency of the antenna was analyzed using two different simulation models (full model of EV-55 vs. part of the airplane's wing: *EV-55* vs *WING*) and two different computational methods (TD vs. FD). The main results are depicted on Figure 3 and summarized in table Table 1.

Current results indicates that the antenna is slightly underperforming with respect to the requirements. However such a possibility has been expected considering the fact an ideal monopole antenna has benefit of 3dB due to a large conductive ground plane ($2.19 + 3$ dBi). The requirement for the maximum field strength deviation is usually referred to the antenna prior its final installation on an airplane. Presented results indicate that this requirement can be fulfilled without significant problems (*WING* models).

In addition, further analyses on full-scale EV-55 model indicated that the antennas installed on both wings are decoupled. So it is possible to use diversity strategies to improve the system performance.

3.2 Lightning strike protection

Winglets represent one of the one most probable locations where a lightning strike can hit an airplane during a flight (Zone 1A, 1B). This is why the winglet antenna has to be designed and tested to more critical electromagnetic environments than is usual for ordinary VHF antennas installed on a fuselage (Zone 1A). The main protection against possible direct attachment of a lightning strike to the antenna is provided by the winglet structure and position of the antenna. The winglet has an integrated diverter strip going along the leading edge, from the tip of the winglet to the bottom part, where it is conductively connected to the metallic

structure of a wing (see Figure 1). In addition, an expanded Cu metal foil is integrated into an outer layer of the winglet external CFRP shell to provide both an additional protection to the CFRP structure and to provide better route to a lightning channel passing across the surface during a lightning strike event.

In case of possible indirect effects of lightning, it is essential to determine approximate levels of voltage and current transients induced at the port of the antenna, along the whole VHF route, and neighboring systems that may interfere with the VHF system. In this paper, only U and I transients at the port of the antenna will be discussed (transients induced in cables and other electrical systems can be obtained in a similar way).

The basic concept of a simulation model that can be used for this kind of analyses is presented on Figure 4. The model does not address possible problems due to thermal damage, dielectric breakdown, arcing and sparking events. The EM source is represented by an ideal current source positioned at the tip of the winglet (the end of the diverter strip). The applied current waveform emulates a fist return stroke (Component A). [5]

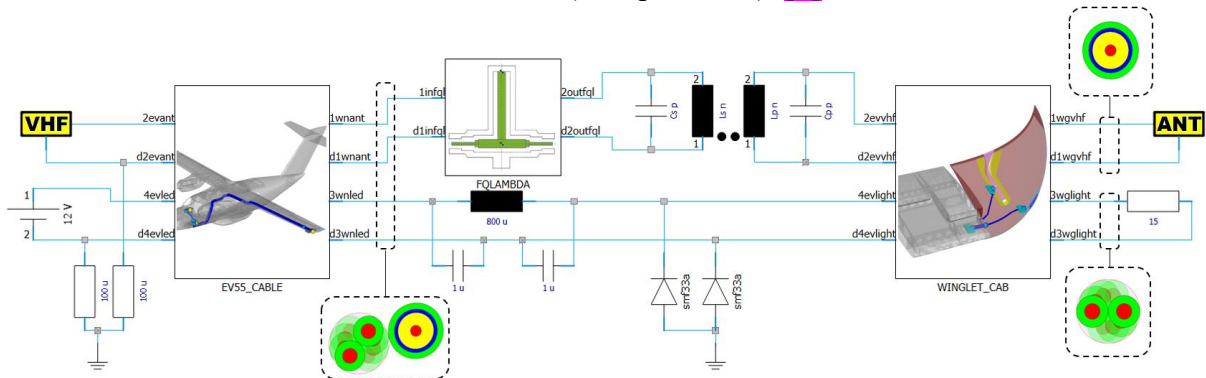


Figure 4: Basic concept of the VHF system simulation model

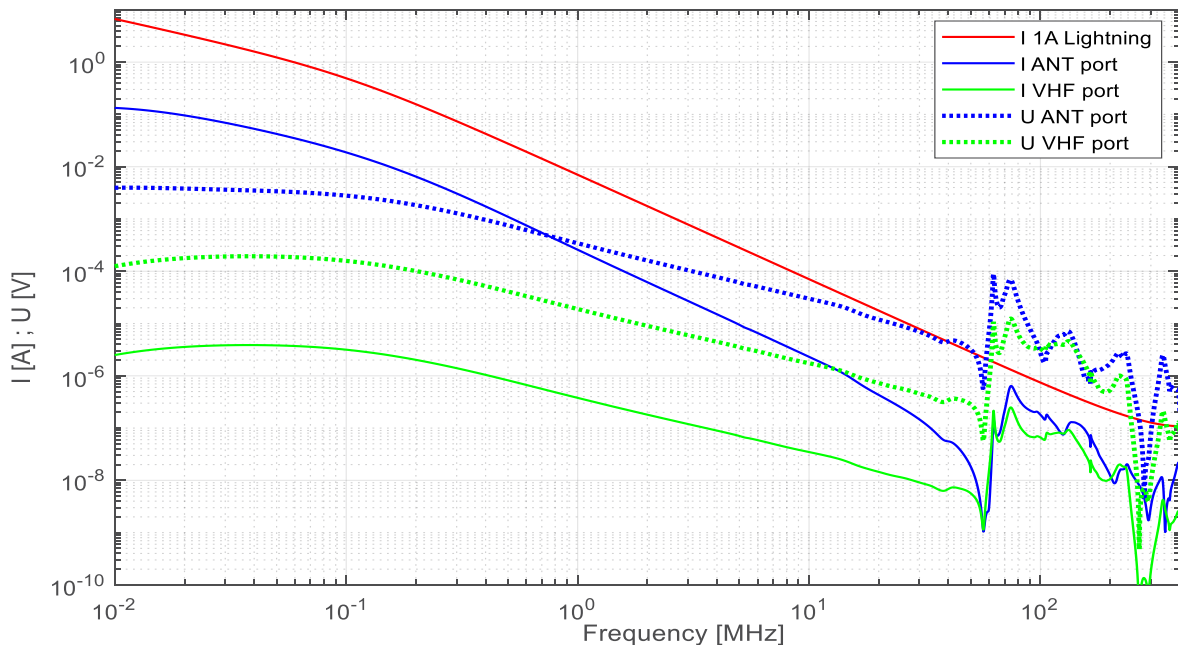


Figure 5: U and I transients at the antenna port and VHF transceiver input produced by lightning currents (current source: component A) passing through the winglet to the EV-55 wing structure

Relatively high levels of currents can be seen at the antenna port at low frequencies (see Figure 5). Character of these disturbances will naturally change at the higher frequencies, where the antenna starts to resonate, thus voltage transients will become dominant due to increasing impedance at the port. Results indicate that lightning transients at the antenna port does not represent a significant problem when considering the basic protective circuitry introduced to the VHF line. Nevertheless, the VHF antenna represents only one part of the problem and other potential sources of EM disturbances have to be analyzed to obtain full picture of the system behavior.

4 SUMMARY

Simulated and measured reflection coefficients of the notch antenna for different scenarios are showing good antenna matching and sufficient bandwidth. Radiation efficiency of the antenna installed on the EV-55 airplane is not fully meeting the general requirements. However the reason is not due to bad performance of the antenna but due to the fact that these requirements are not taking into account similar scenarios / positions for installation of a VHF antenna. The antenna has a good potential for further adjustments with respect to its bandwidth and radiation characteristics. This will give us enough space for final adjustments of the antenna during the final stage of the prototype preparation, or at higher TRLs when solving possible performance deviations due to manufacturing inaccuracies or other changes.

The last part of the paper is discussing basic protection of the winglet with integrated VHF antenna against direct and indirect effects of a lightning strike. We have presented the basic simulation model for more detailed analysis of lightning transients introduced to the VHF line via the antenna element and determined their approximate levels.

Knowledge of resulting transient levels can help us to determine whether the electronic systems are sufficiently protected at the system and sub-system levels and establish the proper lightning requirements for the whole VHF communication system at higher TRLs.

ACKNOWLEDGEMENT

All work described in this paper has received funding from the European Union's Horizon 2020 research and innovation programme under grant agreement No 723167, ACASIAS project.

REFERENCES

- [1] Advanced Concepts for Aero-Structures with Integrated Antennas and Sensors (ACASIAS), <http://www.acasias-project.eu/>
- [2] RTCA DO-186B, Minimum Operational Performance Standards (MOPS) for Airborne Radio Communications Equipment Operating Within the Radio Frequency range 117.975 – 137.000 MHz
- [3] M. Martínez-Vázquez, J. Balcells-Ventura, Z. Řezníček, K. Gonet, S. Steeger, P. Vrchota, V. Lungaho, VHF notch antenna integrated in an aircraft winglet, submitted to IEEE Antennas & Propagation Society Symposium, Atlanta, US, 2019.R.
- [4] A. Burberry, VHF and UHF antennas, IEE Electromagnetic series 36, Peter Peregrinus, 1992.
- [5] SAE ARP5412A, Aircraft Lightning Environment and Related Test Waveforms, 2004

EXPERIMENTAL ANALYSIS OF THE ACASIAS ACTIVE LINING PANEL EMUS 2020

S. ALGERMISSEN* AND M. MISOL*

* German Aerospace Center (DLR)
Institute of Composite Structures and Adaptive Systems
Braunschweig, Germany
e-mail: stephan.algermissen@dlr.de, web page: <http://www.dlr.de>

Key words: acoustic control, active lining, modal testing, thermal testing

Abstract. The participants of the EU-project ACASIAS develop advanced concepts for aero-structures with multifunctional capabilities. Within work package 3 an active system for noise reduction is integrated into a curved lining panel. The objective is the reduction of the interior sound pressure level by increasing the transmission loss of the lining panel. The application scope includes current propeller driven aircraft and future aircraft with counter-rotating open rotor (CROR) engines. The drawback of these CO₂-efficient engines is their high sound emission in the frequency band up to 500 Hz. Active noise reduction systems are able to achieve performance in this frequency band while passive sound insulation materials fall behind. Thus, active systems are the key technology to avoid unacceptably high noise levels for passengers.

During the last period of the project the main experiments are conducted. The active lining with its dimensions of 1300 × 1690 mm² (W × H) is mounted in a setup in the acoustic transmission loss test facility of the DLR. Several tests in different categories are run to characterize the vibration and sound transmission behavior of the lining. In this paper the active lining and its components are briefly introduced and the results of the modal and the thermal testing are presented.

1 INTRODUCTION

The last half year marks the beginning of the experimental phase of ACASIAS work package (WP) 3. In the period before concepts have been developed to take active system for noise reduction in aircraft to the next level. Laboratory equipment is substituted by off-the-shelf components. These components are encapsulated to create a production-friendly integration approach [1]. System maintenance and repair solutions are provided. Control system algorithms are fine tuned to achieve the expected goals [2]. The following sections provide a summary of two selected experiments which are conducted with the ACASIAS active lining in the acoustic transmission loss test facility of DLR. After introducing the active lining, the results of the first experiment, the modal testing, are presented. Accompanying the construction of the lining a detailed Finite Element (FE) model has been setup by the WP 3 partner CIMNE. The objective of this experiment is to provide modal data within a certain bandwidth in order to update the

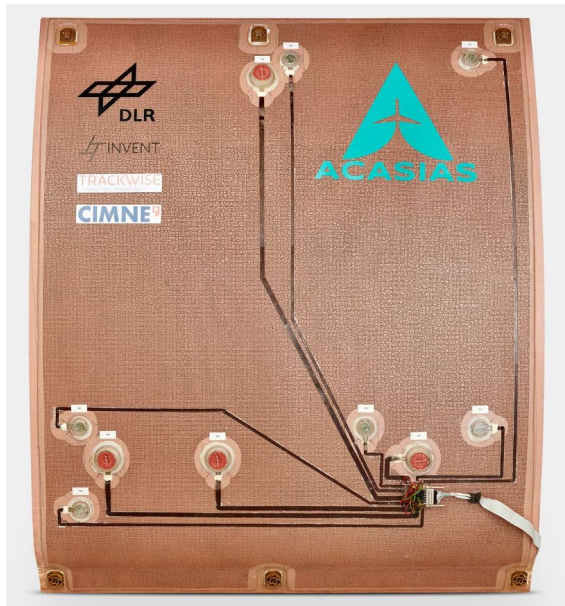


Figure 1: Active lining, backside

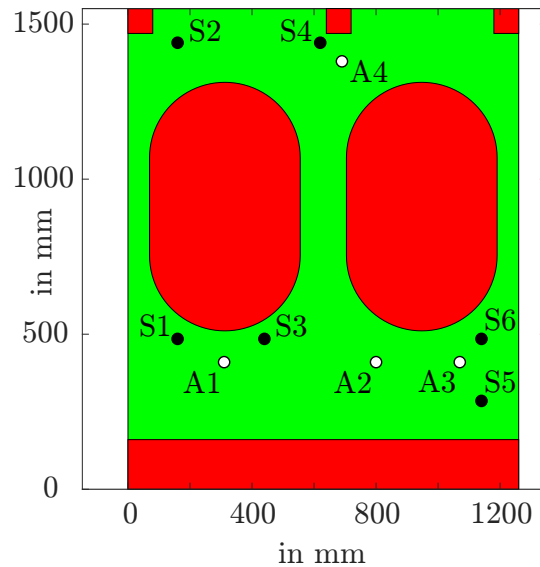


Figure 2: Actuator (A#) and sensor (S#) placement, passenger view

FE model. The second experiment is driven by the question how temperature changes affect the vibration behavior of the lining and how to integrate this in the control loop.

2 ACTIVE LINING

The platform for demonstrating the ACASIAS WP 3 innovations is a curved lining panel, see Figure 1. With its dimensions of $1300 \times 1690 \text{ mm}^2$ (W \times H) it complies to the dimensions of original A350 sidewall panels. The partners agreed to neglect the window cut-outs since the effort and the costs for manufacturing an adequate mold would have exceeded the financial framework. Furthermore, the new technologies can be presented without loss of generality with the given approach.

The lining is designed as a sandwich part. An inner honeycomb core is stabilized by a top layer of glass fiber prepreg on each side. In series production the core is crushed in a press during the curing cycle. Since a press is not available for manufacturing at the partner's site, the active lining is manufactured with an intact honeycomb core. Nevertheless, the final thickness shall comply to the original one. The layup of the lining has been defined together with the industrial advisory board member DIEHL AVIATION. The inner layer is a fine meshed prepreg. It generates a very flat surface that faces the passengers. In series production the surface is equipped with customer-specific coating. On the inner layer a honeycomb core is placed. On top of the core a single layer of very rough and open glass fiber prepreg finalizes the layup. The target thickness of the final lining is approximately 7 mm. At six positions, three at the upper and three at the lower edge, the lining is connected to the fuselage structure using shock mounts. Figure 3 shows the situation in the acoustic lab. For testing the lining is mounted in a

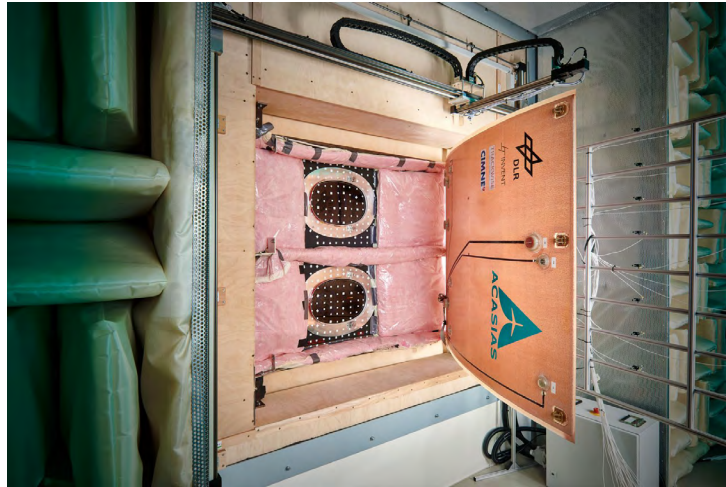


Figure 3: Lining in acoustic lab

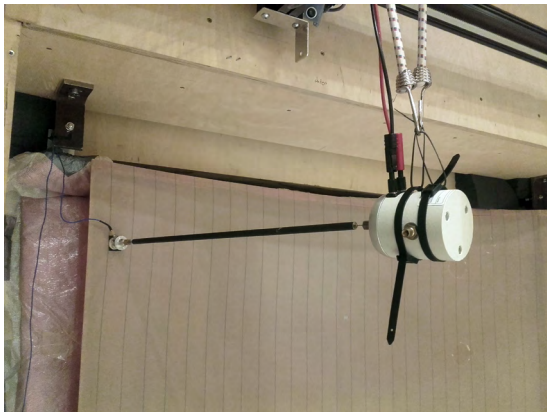


Figure 4: Shaker position 1



Figure 5: Shaker position 2

90° counterclockwise rotated position in front of an A350-like fuselage panel.

The lining panel is made "active" by including sensors, actuators and wiring in order to control its vibrations and therefore its sound radiation into the cabin. The sensors of the lining are accelerometers measuring the normal acceleration at the point of installation. The actuators introduce defined forces into the lining structure. In this project electrodynamic exciters are used instead of piezo actuators to achieve the desired performance at frequencies below 200 Hz.

In a detailed analysis [2] the effect of the number of sensors and actuators on the control performance is investigated. The result leads to six sensors and four actuators which are placed on the lining according to the given criterion. Figure 2 summarizes the final placement of the components. For a transfer of results to a lining from series production, the areas with windows, air condition ducts and mounting points are treated as forbidden (red) with regard to placement and routing. The type of actuators and sensors and their integration technology is described in [1] in detail.

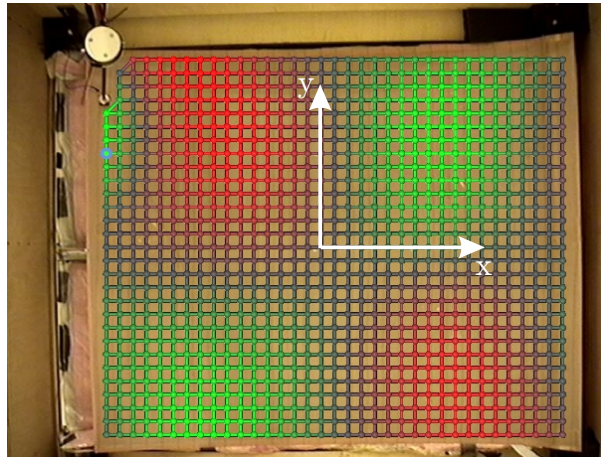


Figure 6: LSV scan point grid with coordinate system

3 MODAL ANALYSIS

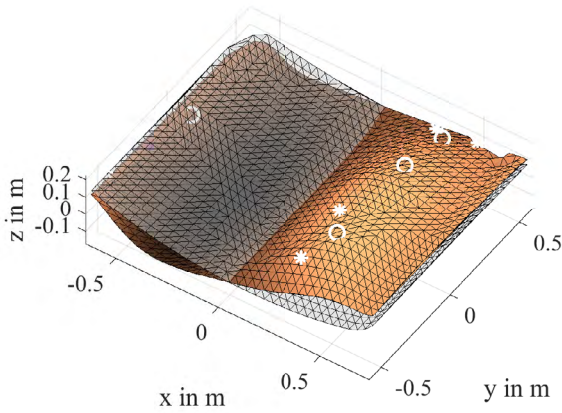
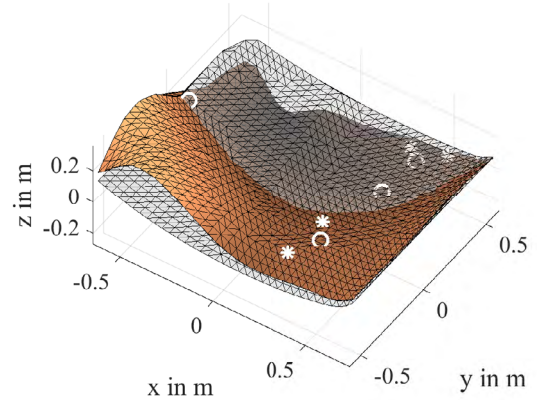
An experimental modal analysis is conducted with the lining panel. The objective is to provide poles and mode shapes for the update of the FE model created within the project. The analysis is divided into two parts. First, the experimental data have to be obtained. Second, these data have to be merged and fed into a modal analysis software to extract the modal data. Beginning with the description of the experimental setup, the entire modal analysis is described in the following sections.

3.1 Setup

Nearly all technical structures vibrate and exhibit modal behavior. In order to describe it, modal parameters are sufficient in most cases. Linearity and causality are assumed for the vibration behavior of the time-invariant structure under test. The input data for the modal analysis are frequency response functions (FRF) from force to displacement measured on a set of selected points of the given structure. Since the inner side of the lining which directs to the passengers is essential for describing the sound emission, a grid of approximately 1,000 points is specified on this surface. Each point has six degrees of freedom (DOF), three translational and three rotational. The relevant DOF for this application is the normal displacement of each surface point. The measurement of displacement at a huge amount of points is challenging. Therefore, a POLYTEC[®] PSV-400 laser scanning vibrometer (LSV) is used to determine the FRF from force input to point velocities. After calculation of the FRF the input unit is changed to displacement by division with $j\omega$.

The input force is generated by a shaker mounted hanging in front of the lining. The force is measured with a sensor of type PCB[®] 208B01 which is bonded on the lining. To achieve modal completeness two different excitation points are selected, see Figure 4 and 5. The points are located at the upper edge of the lining panel with respect to the mounting direction. Position 1 is located 165 mm from the upper and 55 mm from the left edge. Whereas position 2 is 165 mm apart from the upper and the right edge.

Mode number	Undamped eigen-frequency in Hz	Damping ratio in %	Mode number	Undamped eigen-frequency in Hz	Damping ratio in %
1	27.2	2.8	8	98.3	2.6
2	39.8	8.5	9	110.4	1.8
3	44.9	4.1	10	127.6	3.5
4	46.5	5.1	11	152.1	4.7
5	59.5	2.3	12	159.1	3.4
6	67.6	3.4	13	176.8	2.9
7	77.8	3.1	14	197.7	2.7

Table 1: Modal data**Figure 7:** Mode shape #1**Figure 8:** Mode shape #2

3.2 RESULTS

For testing the shaker is driven with a periodic chirp signal from the LSV. The bandwidth for the measurement is set to 1 kHz while 1,600 FFT lines are used which leads to a frequency resolution of 0.625 Hz in the FRF. A three times complex averaging enhances the signal quality. The LSV scan point grid is shown in Figure 6. It is an even rectangular grid with 35 points in x - and 29 points in y -direction with a spacing of app. 40 mm. Five points at the upper left corner are neglected due to their lack of visibility. Therefore, the final grid consists of 1,010 points.

Two measurements are conducted where the shaker is mounted in the positions defined above. The resulting FRF are merged with the modal analysis software XMODAL3. By means of the complex mode indicator function (CMIF) 14 relevant modes are identified in the bandwidth from 20 to 200 Hz. The modal data are summarized in Table 1. The damping ratio lies in the interval from 1.8 to 8.5 %. All identified mode shapes are real-valued and orthogonal to each other. Figures 7-10 show shapes of selected modes. The circles denote the positions of the actuators while the asterisk marks the sensors. It becomes obvious that not all modes are symmetric. This is mainly due to the distribution of actuator and sensor masses.

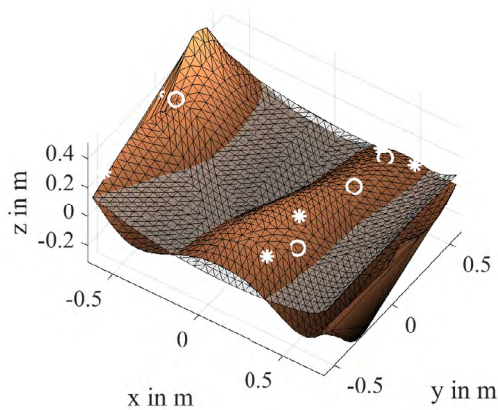


Figure 9: Mode shape #6

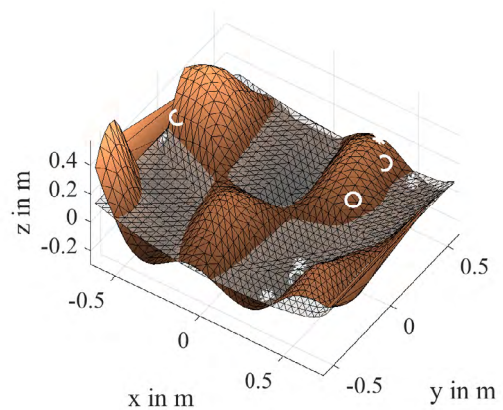


Figure 10: Mode shape #10

4 THERMAL EXPERIMENTS

Lining panels in aircraft are subject to environmental influences such as humidity or temperature in the cabin. Although the climate in a cabin is controlled, the temperature of the lining panels may differ from the air condition set point temperature due to solar radiation for example. Since the material parameters are a function of temperature, the vibration behavior of the lining panel changes with increasing temperatures as well. The active noise reduction system presented in [3] must maintain its performance regardless of the temperature. Therefore, the influence of the temperature on the vibration behavior of the lining needs to be determined. In control, the accuracy of the secondary path model \underline{G} is elementary for the stability of the entire control system. The objective of the experiments presented in the following section is the measurement of the FRF matrix \underline{G} at different temperatures. In a second stage, a temperature dependent model of \underline{G} is formulated based on the results of the experiments.

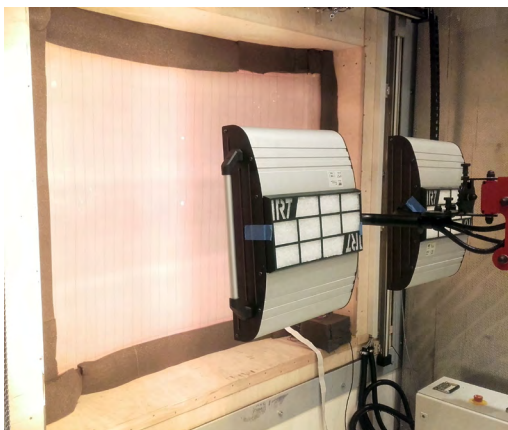


Figure 11: IR dryer in front of lining panel

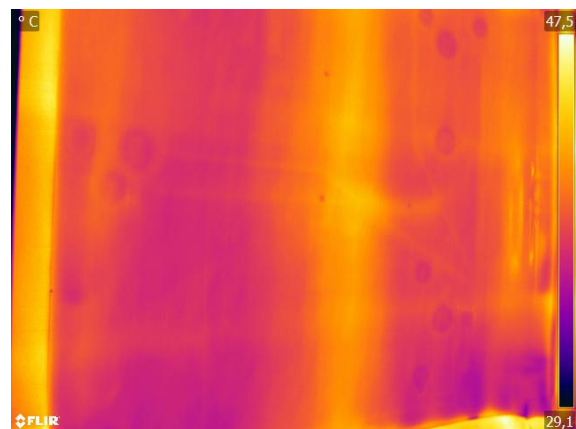


Figure 12: Thermal camera image at set point 35 °C

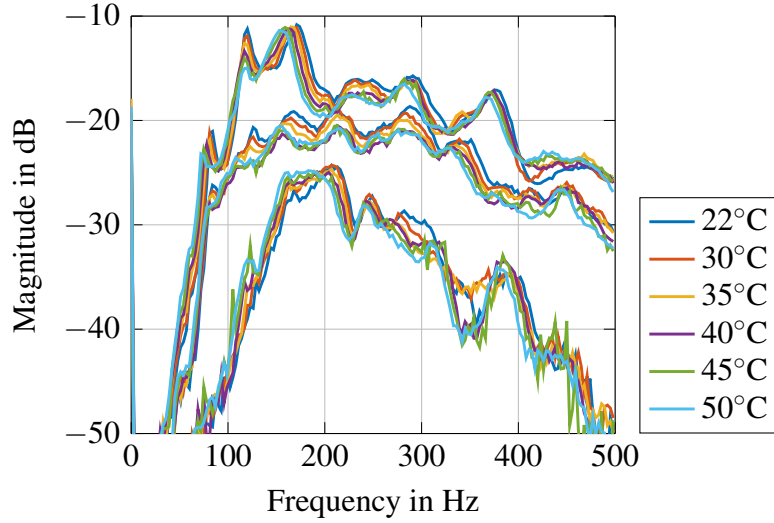


Figure 13: Singular values of \underline{G}_s at temperatures T_s

4.1 Setup

The temperature ranges for airborne equipment are defined in the EUROCAE ED-14G [4] chapter four. Lining panels belong to category A1 for which an operating temperature range from -15°C to $+55^\circ\text{C}$ is defined. The acoustic transmission loss test facility of DLR is not equipped with a cooling system. Therefore, the following experiments focus on the temperature range from ambient 22°C to 50°C .

The thermal experiments are conducted in the same setup as the modal testing and the control experiments. The even heating of the lining's surface is realized with an infrared (IR) dryer of type HEDSON IRT 4-2 PCAUTO. The dryer consists of two heads each equipped with IR lamps with an output power of 6 kW. The temperature of the irradiated surface is controlled by the dryer based on contact-free temperature measurements. To monitor the heating process, an additional temperature probe is mounted on the backside of the lining close to the lower left corner. A thermal imaging camera of type FLIR[®] A615 is used to observe the temperature distribution on the surface of the lining. Figure 11 shows the setup in the lab.

The secondary control path consists of the rapid prototyping control system, the actuators and the sensors of the lining. Additional anti-aliasing and reconstruction filters are placed in the signal paths. The overview of the entire control loop is given in [3]. The number of sensors $n_y = 6$ and actuators $n_u = 4$ define the dimensions of $\underline{G}_{6 \times 4}$.

As set points for the experiments the following temperatures from ambient to 50°C are defined:

$$T_s = [22 \quad 30 \quad 35 \quad 40 \quad 45 \quad 50] \text{ in } ^\circ\text{C}.$$

As temperature reference the probe on the backside is used. The set point of the IR dryer controller is adjusted according to the probe. A steady state with respect to the lining temperature is achieved by a 11 min time span of the heating process at each set point. The temperature distribution is checked with the thermal imaging camera at each set point. Figure 12 gives an impression of the distribution at 35°C . The view axis of the camera is equivalent to the one in

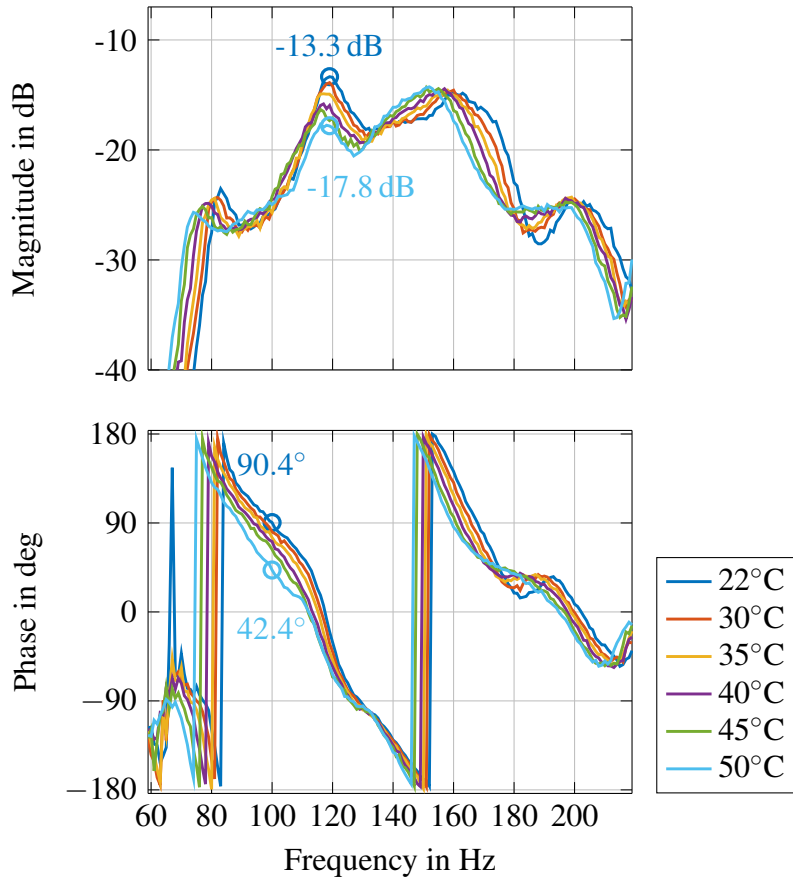


Figure 14: Bode plot of G_{12} at temperatures T_s

Figure 11. The positions of the actuator and sensor inserts can be observed as colder spots on the lining.

4.2 Results

The identification of the secondary path \underline{G} is conducted with the rapid prototyping system. The four actuators are driven with uncorrelated noise signals for 64 s while the six sensors record the lining's responses. The bandwidth of the identification is set to 1000 Hz since the cut-off frequency of the anti-aliasing and reconstruction low-pass filters are set to 500 Hz. The FRF of \underline{G} is calculated with 64 times averaging which results in a frequency resolution of 1 Hz. During the experiment actuator 3 and sensor 6 had a failure at certain temperatures. Therefore, the two signal channels are neglected in the subsequent analysis.

To compare the FRF at temperatures T_s , the singular values of \underline{G} are shown in Figure 13 in the relevant bandwidth. It becomes obvious that \underline{G} is temperature dependent and that in general the eigenfrequencies decrease with increasing temperature. The shift of eigenfrequencies is moderate and smooth. A stepwise change is not observed. In a first, simplified assumption the shift can be explained with a decreasing stiffness of the lining towards higher temperatures.

To quantify the shift, the Bode plot G_{12} from actuator 2 to sensor 1 is considered more closely in Figure 14. In this example the magnitude difference in the eigenfrequency at 119 Hz is

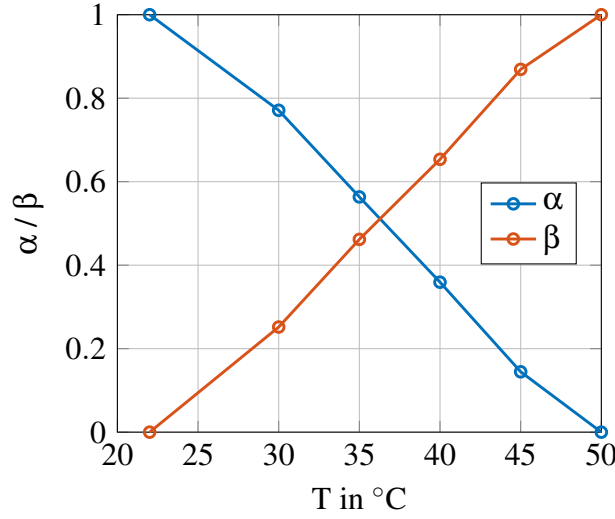


Figure 15: Factors α and β as a function of temperature T

4.5 dB. Due to the shifting eigenfrequency around 80 Hz the phase difference at 100 Hz amounts to 48° while the magnitude remains constant. Magnitude and phase errors in this order may lead to instability of the control loop. These results confirm the assumption that a temperature dependent secondary path model $\underline{\underline{G}}(T)$ is needed for operation of the system in aircraft.

As few measurements as necessary should be accomplished to generate $\underline{\underline{G}}(T)$. Since the shifts of the eigenfrequencies are smooth and continuous, a linear approach is proposed:

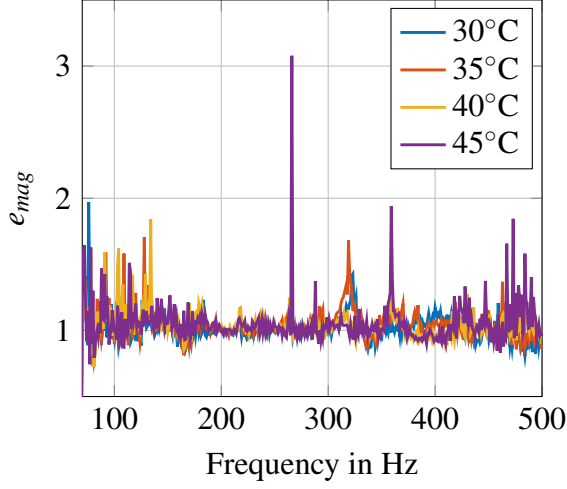
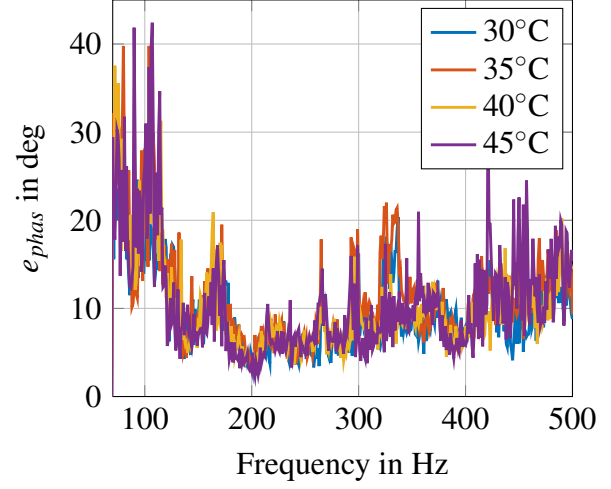
$$\underline{\underline{\tilde{G}}}(T) = \alpha(T)\underline{\underline{G}}(22^\circ\text{C}) + \beta(T)\underline{\underline{G}}(50^\circ\text{C}) \quad (1)$$

The interpolated model $\underline{\underline{\tilde{G}}}$ at temperature T is a linear interpolation of the two boundary models at 22°C and 50°C . The real-valued factors α and β have to be determined by experimental data. Therefore, (1) is rearranged to:

$$\underline{\underline{\tilde{G}}}(T) = \left[\underline{\underline{G}}(22^\circ\text{C}) \quad \underline{\underline{G}}(50^\circ\text{C}) \right] \begin{bmatrix} \alpha(T) \\ \beta(T) \end{bmatrix} \quad (2)$$

Since the FRF are also matrices, functions of frequency ω and complex-valued, Equation (2) expands to:

$$\underbrace{\begin{bmatrix} \Re(G_{11}(\omega_1, T)) \\ \vdots \\ \Re(G_{n_y n_u}(\omega_1, T)) \\ \Im(G_{11}(\omega_1, T)) \\ \vdots \\ \Im(G_{n_y n_u}(\omega_1, T)) \\ \vdots \\ \Im(G_{n_y n_u}(\omega_N, T)) \end{bmatrix}}_{\underline{\underline{A}}} \stackrel{!}{=} \underbrace{\begin{bmatrix} \Re(G_{11}(\omega_1, 22^\circ\text{C})) & \Re(G_{11}(\omega_1, 50^\circ\text{C})) \\ \vdots & \vdots \\ \Re(G_{n_y n_u}(\omega_1, 22^\circ\text{C})) & \Re(G_{n_y n_u}(\omega_1, 50^\circ\text{C})) \\ \Im(G_{11}(\omega_1, 22^\circ\text{C})) & \Im(G_{11}(\omega_1, 50^\circ\text{C})) \\ \vdots & \vdots \\ \Im(G_{n_y n_u}(\omega_1, 22^\circ\text{C})) & \Im(G_{n_y n_u}(\omega_1, 50^\circ\text{C})) \\ \vdots & \vdots \\ \Im(G_{n_y n_u}(\omega_N, 22^\circ\text{C})) & \Im(G_{n_y n_u}(\omega_N, 50^\circ\text{C})) \end{bmatrix}}_{\underline{\underline{B}}} \begin{bmatrix} \alpha(T) \\ \beta(T) \end{bmatrix} \quad (3)$$


Figure 16: Magnitude error

Figure 17: Phase error

Where $\Re()$ and $\Im()$ denote the real and the imaginary part and N the number of frequencies. On the left hand side $\tilde{\underline{G}}(T)$ is substituted by the measured $\underline{G}(T)$ in order to solve the equation system for α and β at each temperature T_s . The solution is found by building the Moore-Penrose pseudoinverse $()^+$:

$$\begin{bmatrix} \alpha(T) \\ \beta(T) \end{bmatrix} = \underline{\underline{B}}^+ \underline{\underline{A}} \quad (4)$$

The values for α and β at the boundaries are set to 0 or 1 according to the definition in (1). The resulting plots for these experiments are shown in Figure 15.

The functions of α and β show a nearly linear behavior over T . Hence, the proposed approach in (1) together with a linear formulation of the factors seems to be suitable for a first approach to model the temperature dependent behavior of the \underline{G} . To validate the benefit of the interpolated model $\tilde{\underline{G}}$ at temperatures T_s , the mean magnitude and phase errors are calculated. Therefore, all single FRF in the transfer matrix of $\tilde{\underline{G}}(\omega, T)$ are divided by the corresponding measured $\underline{G}(\omega, T)$ at temperature T . The frequency dependent mean magnitude and phase errors are calculated by summation:

$$e_{mag}(\omega_n, T) = \frac{1}{n_u n_y} \sum_{u=1}^{n_u} \sum_{y=1}^{n_y} \left| \frac{\tilde{G}_{yu}(\omega_n, T)}{G_{yu}(\omega_n, T)} \right| \quad (5)$$

$$e_{phas}(\omega_n, T) = \frac{1}{n_u n_y} \sum_{u=1}^{n_u} \sum_{y=1}^{n_y} \left| \angle \left(\frac{\tilde{G}_{yu}(\omega_n, T)}{G_{yu}(\omega_n, T)} \right) \right| \quad (6)$$

Applied to the experimental data, the plots in Figures 16 and 17 result. Despite some peaks, the values for e_{mag} are closely located to the desired value of 1. The phase error e_{phas} exceeds 20° below 120 Hz while it remains under 20° for nearly all frequencies up to 500 Hz. To put the errors into a context, a second error calculation is performed. It is considered the case that only the base model $\underline{G}(22^\circ\text{C})$ exists. The lining is heated up to 40°C and the secondary path

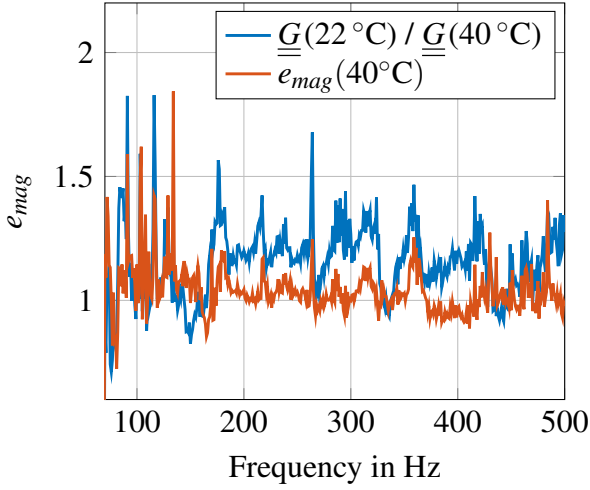


Figure 18: Magnitude error

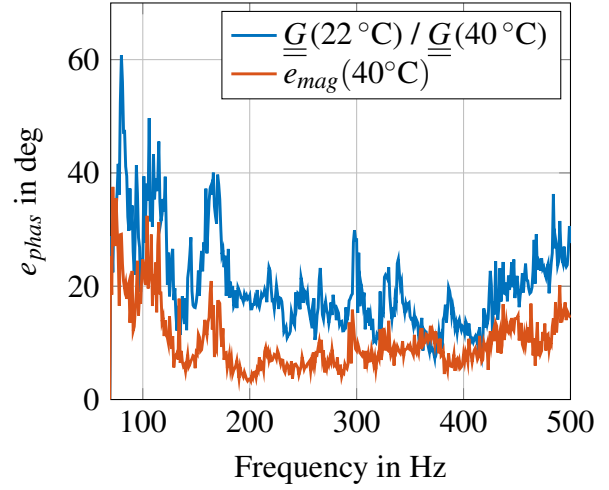


Figure 19: Phase error

model behaves like $\underline{G}(40^\circ\text{C})$. The error that occurs is calculated with (5) and (6) while \tilde{G} is substituted by $\underline{G}(22^\circ\text{C})$. Figure 18 and 19 compare this error to $e_{mag}(40^\circ\text{C})$ and $e_{phas}(40^\circ\text{C})$.

It is obvious that the interpolated model \tilde{G} significantly reduces the error in nearly all relevant frequencies in the control bandwidth. Thus, the use of the interpolated model instead of the exclusive use of the base model $\underline{G}(22^\circ\text{C})$ is preferred. To set up the interpolated model, only a single extra measurement at 50°C has to be conducted in this case.

5 CONCLUSIONS & OUTLOOK

The realizations and the results of two main experiments of the last phase of the ACASIAS WP 3 are presented. Within the modal analysis 14 modes in the bandwidth from 20 to 200 Hz could be determined. Real modes and realistic damping ratios are identified. The modal data now serve as a base for the model updating procedure of the lining's FE model. Beyond that, the effects of different ambient temperatures on the secondary path of the control loop are quantified in a second experiment. It has been shown that the effects cannot be neglected when the noise reduction system becomes operational. An approach is proposed to describe the temperature dependency by a linear combination of two boundary models. This approach enables a simple tracking of the varying vibration behavior in order to adjust the controller and to optimize its performance over a wider temperature span. Future work will concentrate on the implementation of these results in the controller software.

6 ACKNOWLEDGMENTS



This project has received funding from the European Union's Horizon 2020 research and innovation programme under grant agreement No. 723167.

The authors gratefully acknowledge the support of the industrial advisory board member DIEHL AVIATION, Laupheim, Germany.

REFERENCES

- [1] S. Algermissen, M. Misol, A. Kokott, T. Haase, K. Gonet, and V. Lungaho, “Towards a lining integrated active structural acoustic control system,” in *Proc. of European Conference on Multifunctional Structures (EMuS)*, X. Martinez and H. Schippers, Eds., Juni 2019, pp. 30–37. [Online]. Available: <https://elib.dlr.de/127884/>
- [2] M. Misol and S. Algermissen, “Remote sensing for a lining integrated structural acoustic control system,” in *Proc. of European Conference on Multifunctional Structures (EMuS)*, X. Martinez and H. Schippers, Eds., Barcelona, Spain, 2019. [Online]. Available: <https://elib.dlr.de/128067/>
- [3] ———, “Noise reduction results of the ACASIAS active lining panel,” in *Proc. of European Conference on Multifunctional Structures (EMuS)*, X. Martinez and H. Schippers, Eds., 2020.
- [4] European Organisation for Civil Aviation Equipment (EUROCAE), *EUROCAE ED-14G: Environmental Conditions and Test Procedures for Airborne Equipment*. EUROCAE, 2011.

NOISE REDUCTION RESULTS OF THE ACASIAS ACTIVE LINING PANEL

EMUS 2020

M. MISOL*, S. ALGERMISSEN*

* German Aerospace Center (DLR)
Institute of Composite Structures and Adaptive Systems, Braunschweig, Germany
e-mail: malte.misol@dlr.de, web page: www.dlr.de/fa/en

Key words: Active Noise Reduction, ANC, ASAC, Interior Noise, Aircraft, CROR

Abstract. Advanced concepts for aero-structures with multifunctional capabilities are investigated within the EU-project ACASIAS. In work package 3 of ACASIAS, components of an active noise reduction system are structurally integrated into a curved sandwich panel by means of 3D printed inserts. This so-called smart lining is intended for application in aircraft as a modular and lightweight interior noise treatment in propeller-driven aircraft. The broad application scenario of smart linings ranges from retro-fitting of current regional aircraft such as ATR 42, ATR 72, DHC-8 Q400 to the application in new short-range aircraft with energy efficient counter rotating open rotor (CROR) engines or with distributed electric propellers. A key feature of the smart lining with integrated active components is its modularity, facilitating a flexible application in the aircraft cabin. This requires a fully self-contained sensing mechanism based on structurally integrated accelerometers. Using the normal surface vibration data from the integrated sensors, the smart lining is able to predict the sound field in front of it. The so-called virtual microphone method with remote sensors and observer filter allows to get rid of real microphones and wiring in the aircraft cabin. This makes retro-fitting easier because it reduces wiring effort and costs which is beneficial for future aircraft as well. However, the use of virtual instead of real microphones might deteriorate the performance or even the stability of the active noise reduction system because it relies on accurate plant models. Laboratory experiments in a sound transmission loss facility are conducted to assess the behavior of the smart lining with virtual microphones and compare it to a smart lining with real microphones. The sensitivity of the smart lining to environmental changes and the noise reduction performance and control system stability are investigated in this study.

1 INTRODUCTION

Active noise control is able to reduce cabin noise in propeller driven aircraft. Different approaches are pursued since the late 1980s. One approach followed by Elliott et al. [1] uses loudspeakers to generate anti-sound which destructively interferes with the cabin noise. An alternative approach is the active structural acoustic control (ASAC). The ASAC method requires structural actuators and sensors to control the sound radiating structural vibration of surfaces.

Early results of ASAC are published by Fuller and Jones [2]. One realization of an ASAC system uses actuators and sensors applied to the sidewall panels (linings). Early experiments with such active linings are documented in Lyle and Silcox [3]. Active linings with electrodynamic exciters as actuators are successfully realized by Misol et al. [4] and by Misol [5]. In [4] tests of an active lining in a sound transmission loss facility and in [5], full-scale tests of two active lining modules mounted in the cabin of a Dornier Do728 aircraft are reported.

The active noise control systems mentioned so far have in common that they use microphones as error sensors. However, the requirement of having distributed and closely adjacent microphones in the whole cabin is undesirable because it requires additional wiring and prevents flexible cabin layouts. The so-called smart lining concept proposed by Misol et al. [4] tries to overcome these drawbacks by modular active linings with structurally integrated actuators, sensors and control. This concept requires a substitution of the physical error microphones by virtual error microphones. One applicable method is the remote microphone technique for active control proposed by Roure and Albarazzin [6]. In this technique the error microphones are substituted by remote microphones and an observer filter. In a similar approach, Cheer and Daley [7] replace the remote microphones by accelerometers mounted on the radiating structure. This approach is adopted for the smart lining concept.

The present contribution focuses on the performance and robustness of the ACASIAS active lining panel in the case of imperfect secondary path models. The analysis is based on measurement data and identified frequency response function (FRF) models.

2 Experiments

The experiments are done in the sound transmission loss facility of the German Aerospace Center (DLR). The experimental setup is shown in Fig. 1. The ACASIAS active lining panel (L) is attached to the fuselage structure (F) which itself is mounted in the test opening of the facility. The fuselage is acoustically excited from the reverberation room by means of a loudspeaker array. The excitation sound field is typical for a counter rotating open rotor (CROR) engine. It contains the first five harmonics at 119.4 Hz, 149.2 Hz, 268.6 Hz, 387.5 Hz and 417.9 Hz. The transmitted sound is measured in the semi-anechoic room by means of a microphone array with 24 microphones. Measurements are repeated for ten different distances between microphone plane and lining. The reference signal x is used to assemble the signals from the sequential measurements correctly. The hardware used for data sampling and real-time control is a MicroLabBox from dSPACE (DSP). The sampling rate is set to 2000 Hz. All analog input and output signals are bandlimited to 500 Hz using low-pass filters (LPF). The control signals are amplified with a power amplifier (AMP). A detailed description of the smart lining and the actuator and sensor locations is given in Algermissen and Misol. [8]. The signals from the accelerometers \mathbf{d}_s , microphones \mathbf{d}_a and the reference signal x are used as inputs for the control plant shown in Fig. 2.

3 Simulations

A block diagram of the control plant is shown in Figure 2. The green blocks are input signals and the blue blocks are FRF models both obtained from experiments. The grey blocks perform

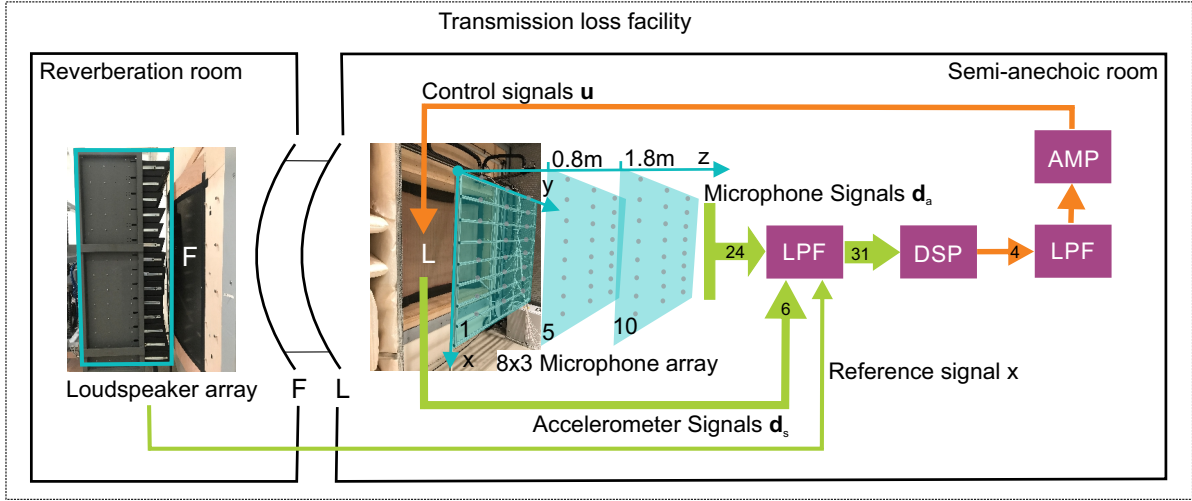


Figure 1: Experimental setup in the sound transmission loss facility.

linear operations on the signals. A detailed description of the control plant and its blocks can be found in Misol [9]. The observer filter \mathbf{O} is defined in [9, Eq. 2] and the adaptation law for the control filter weights is given in [9, Eq. 5]. However, in [9] the actuator feedback on the remote sensors is assumed to be fully compensated by a perfect structural secondary path model $\hat{\mathbf{G}}_s$. The present contribution rejects this assumption and investigates the robustness and the noise reduction performance of the active lining in the case of an imperfect structural secondary path model. This requires the inclusion of the block $\Delta\hat{\mathbf{G}}_s$ into the control plant. If $\Delta\hat{\mathbf{G}}_s \neq 0$ the actuator feedback leads to a distortion of the remote sensor signals \mathbf{D}_s by the control signals \mathbf{U} . It is shown in Algermissen et al. [8] that the structural secondary path \mathbf{G}_s is temperature dependent. Hence, if $\hat{\mathbf{G}}_s$ is identified at temperature T_1 and the real-time control is performed at temperature T_2 , it must be analyzed how the temperature induced inaccuracy of the structural secondary path model affects the control performance.

Equation 1 reveals how the estimated acoustic error signal $\hat{\mathbf{E}}_a$ is influenced by uncompensated actuator feedback.

$$\hat{\mathbf{E}}_a = \mathbf{O}\mathbf{D}_s + \overbrace{(\hat{\mathbf{G}}_a + \mathbf{O}\Delta\hat{\mathbf{G}}_s)}^{\tilde{\mathbf{G}}_a} \mathbf{U} \quad (1)$$

It is assumed that the structural secondary path is identified at temperature T_2 but real-time control is performed at T_1 . In this case $\Delta\hat{\mathbf{G}}_s = \hat{\mathbf{G}}_s^{T_1} - \hat{\mathbf{G}}_s^{T_2}$ describes the difference between the structural secondary path models at temperatures T_1 and T_2 . It is further assumed that the acoustic secondary path \mathbf{G}_a is constant over temperature and is accurately modelled by the acoustic secondary path model $\hat{\mathbf{G}}_a$. If $T_1 \neq T_2 \rightarrow \Delta\hat{\mathbf{G}}_s \neq 0$ and the effective acoustic secondary path is $\tilde{\mathbf{G}}_a = \hat{\mathbf{G}}_a + \mathbf{O}\Delta\hat{\mathbf{G}}_s$. According to Elliott [10, p.201], the adaptive controller is only stable if all eigenvalues λ of the matrix $[\hat{\mathbf{G}}_a^H \tilde{\mathbf{G}}_a + \beta \mathbf{I}]$ are positive. \mathbf{I} is the identity matrix of proper dimension. A nonzero effort weighting factor β can be used to stabilize the system. The gained robustness by a nonzero β is however at the expense of a reduced noise reduction

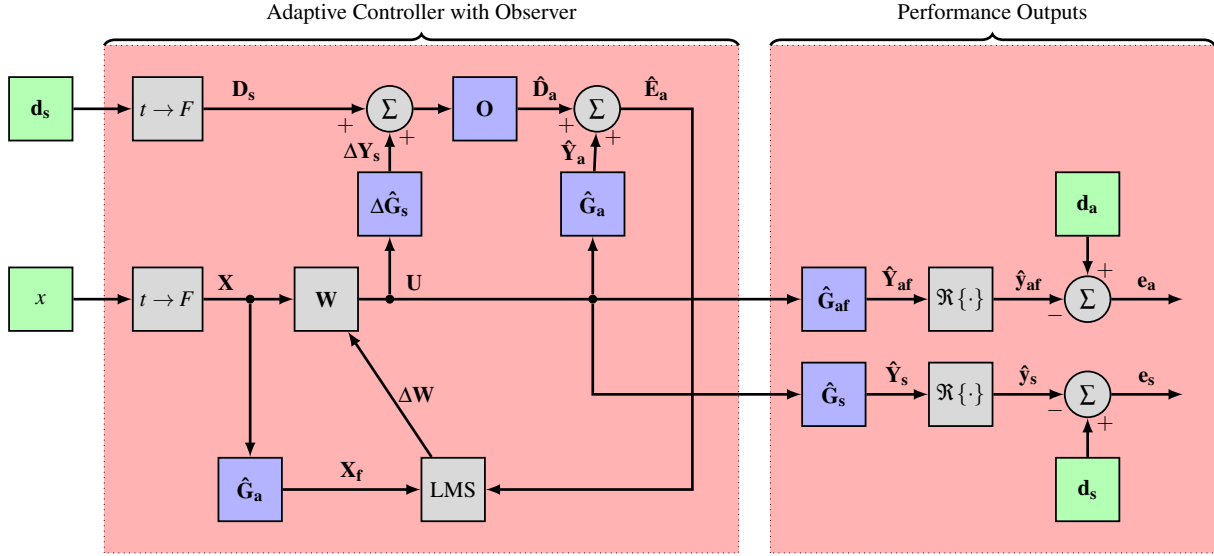


Figure 2: Block diagram of the control plant.

performance. It will be shown in the following Section that a nonzero β is required to stabilize certain harmonics if temperature variations occur.

4 Results

Figure 3 shows the sound pressure level (SPL) distribution on the microphone planes 1, 5 and 10 (see Fig. 1) for the uncontrolled case (a) and for three different temperature scenarios (b), (c) and (d). The other microphone planes are omitted for reasons of clarity. This is possible because the SPL distribution between the planes 1, 5, and 10 is continuous and smooth. The locations of the virtual microphones are indicated by red dots. The underlying data of Fig. 3 is from the performance output e_a in Fig. 2. The sound pressure reductions are calculated relative to the measured disturbance sound pressures d_a . In the uncontrolled case (a), a decrease of the sound pressure level can be seen with increasing distance (z) from the lining. Scenario (b) represents the ideal control scenario with $\Delta \hat{G}_s = 0$. This means either constant temperature conditions or perfect (temperature dependent) secondary path modeling. In this scenario a mean SPL reduction of 10 dB and 5.9 dB(A) is achieved on plane 1 ($z = 0$) and a mean SPL reduction of 8 dB and 5.7 dB(A) is achieved on planes 1–10 (240 virtual microphones). In scenario (c) it is assumed that the structural secondary path model $\hat{G}_s^{T_2}$ is identified for $T_2 = 30^\circ\text{C}$ and the temperature during real-time control is $T_1 = 22^\circ\text{C}$ (or vice versa). This means $\Delta \hat{G}_s \neq 0$ corresponding to an imperfect compensation of the actuator feedback on the remote sensors (accelerometers). In this scenario all eigenvalues λ are positive, but the smallest eigenvalue associated with the frequency of the second harmonic is close to zero and must be stabilized by taking $\beta = 0.0366$. The implications on control performance are visible in Fig. 3 (c). A mean SPL reduction of 4.5 dB and 3.2 dB(A) is achieved on plane 1 ($z = 0$) and a mean SPL reduction of 4.8 dB and 3.9 dB(A) is achieved on planes 1–10. A further degradation of control performance occurs in scenario (d) where it is assumed that the structural secondary path model

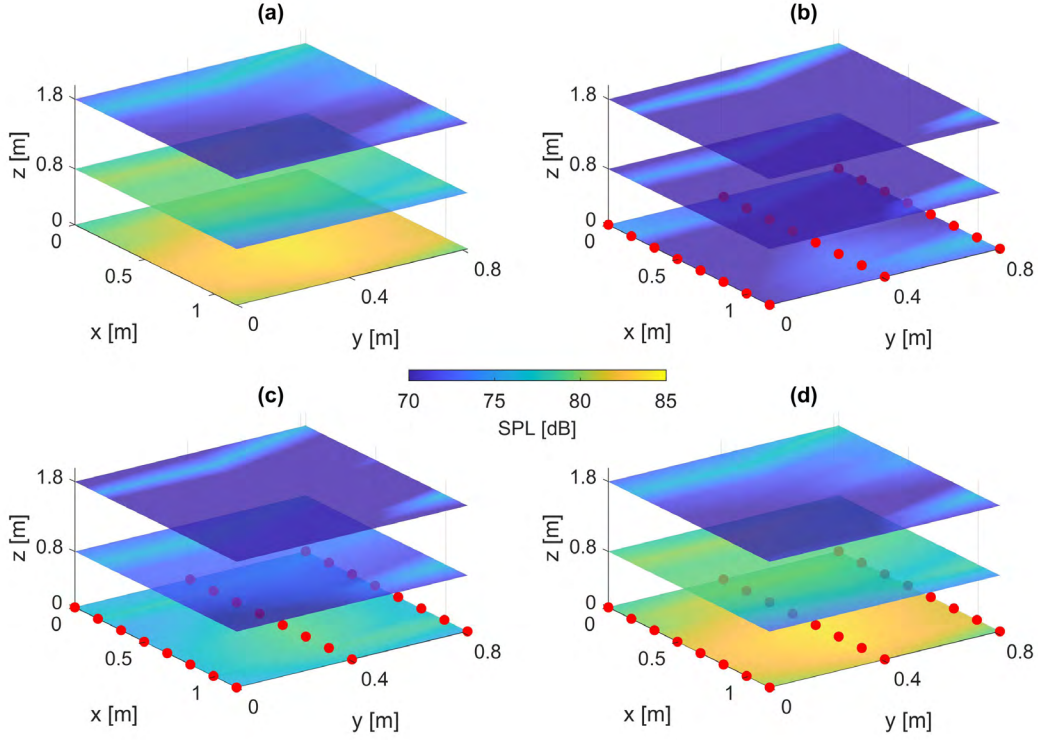


Figure 3: SPL distribution on three planes in front of the lining for the uncontrolled case (a) and for three different temperature scenarios (b)–(d).

$\hat{\mathbf{G}}_s^{T_2}$ is identified for $T_2 = 35^\circ\text{C}$ and the temperature during real-time control is $T_1 = 22^\circ\text{C}$ (or vice versa). In this scenario the smallest eigenvalues associated with the frequencies of the first and the second harmonic are negative and must be stabilized by taking $\beta = 3.2764$ for the first and $\beta = 2.0947$ for the second harmonic. Such strong control weighting implies that the SPL at the first two harmonics will not be affected by the active controller. Since these two harmonics dominate the SPL, Fig. 3 (a) and (d) are very similar. In scenario (d) a mean SPL reduction of 0.14 dB and 0.13 dB(A) is achieved on plane 1 ($z = 0$) and a mean SPL reduction of 0.11 dB and 0.013 dB(A) is achieved on planes 1–10. The results clearly underline that a temperature compensation of the secondary path model is useful and might be necessary. However, it is unclear how much the temperature of the lining actually varies during flight since, as an interior part, it is thermally coupled to the cabin and isolated from the fuselage by an air gap filled with glass fiber insulation bags. Furthermore, the variation of the acoustic secondary path \mathbf{G}_a due to changes in temperature, seat occupation and other factors will have a negative influence on the noise reduction performance as well. But it will not affect the stability of the control system since the acoustic secondary path model $\hat{\mathbf{G}}_a$ is an integral part of the adaptive controller with virtual microphones (see Fig. 2). It remains a future task to assess the implications of imperfect acoustic secondary path models on the control performance.

5 ACKNOWLEDGEMENTS



This project has received funding from the European Union’s Horizon 2020 research and innovation programme under grant agreement No. 723167.

The authors gratefully acknowledge the support of Florian Hesselbach, Alexander Rehmman, Markus Klingseis and Dr. Dietmar Vökle from DIEHL Aviation Laupheim.

REFERENCES

- [1] S. J. Elliott, P. A. Nelson, I. M. Stothers, and C. C. Boucher, “In-flight experiments on the active control of propeller-induced cabin noise,” *Journal of Sound and Vibration*, vol. 140, no. 2, pp. 219–238, 1990.
- [2] C. R. Fuller and J. D. Jones, “Experiments on reduction of propeller induced interior noise by active control of cylinder vibration,” *Journal of Sound and Vibration*, vol. 112, no. 2, pp. 389–395, Jan. 1987.
- [3] K. H. Lyle and R. J. Silcox, “A study of active trim panels for interior noise reduction in an aircraft fuselage,” in *SAE Technical Paper*. SAE International, 05 1995. [Online]. Available: <https://doi.org/10.4271/951179>
- [4] M. Misol, S. Algermissen, M. Rose, and H. P. Monner, “Aircraft lining panels with low-cost hardware for active noise reduction,” in *Joint Conference ACOUSTICS 2018*, 2018. [Online]. Available: <https://elib.dlr.de/122049/>
- [5] M. Misol, “Full-scale experiments on the reduction of propeller-induced aircraft interior noise with active trim panels,” *Applied Acoustics*, vol. 159, p. 107086, 2020. [Online]. Available: <https://elib.dlr.de/129910/>
- [6] A. Roure and A. Albarrazin, “The remote microphone technique for active noise control,” in *PROCEEDINGS OF ACTIVE 99: THE INTERNATIONAL SYMPOSIUM ON ACTIVE CONTROL OF SOUND AND VIBRATION, VOLS 1 & 2*, 1999, pp. 1233–1244.
- [7] J. Cheer and S. Daley, “Active structural acoustic control using the remote sensor method,” *Journal of Physics: Conference Series*, vol. 744, no. 1, 2016.
- [8] S. Algermissen and M. Misol, “Experimental Analysis of the ACASIAS Active Lining Panel,” in *Proc. of European Conference on Multifunctional Structures (EMuS)*, X. Martinez and H. Schippers, Eds., 2020, online event, November 17–18.
- [9] M. Misol, “Active Sidewall Panels with Virtual Microphones for Aircraft Interior Noise Reduction,” *Applied Sciences*, vol. 10, no. 6828, pp. 1–13, 2020. [Online]. Available: <https://elib.dlr.de/136353/>
- [10] S. J. Elliott, *Signal Processing for Active Control*. London: Academic Press, 2001.

A TECHNOLOGY TO (RE-)CONNECT OPTICAL FIBRES EMBEDDED IN COMPOSITE STRUCTURES

EMUS 2020

J. WINDELS¹, J. MISSINNE², E. VOET¹, G. VAN STEENBERGE², G. LUYCKX¹

Com&Sens BV

Begoniastraat 17 PB2 B-9810 Eke Belgium
gbeauduin@com-sens.eu www.com-sens.eu

Keywords: Fiber Bragg Gratings, Optic Fibers, Structural Health Monitoring

Abstract. Optical fibre Bragg grating (FBG) sensors are commonly used for structural health monitoring in composite materials, since their small dimensions, high sensitivity and multiplexing capacity are a good match with the structures to be monitored. We present a method for making a low-loss connection to an FBG optical fibre sensor that is integrated in a fibre reinforced composite structure. The method allows to both manufacture composite structure without taking special precautions to prevent damage to the connecting fibre and (if needed) to repair the connecting fibre, while optimizing the optical connection efficiency even if both fibres have dissimilar mode field diameters.

1. INTRODUCTION

Optical Fibre Bragg grating sensor technology (FBG) is the most promising technology to implement self-sensing features in composite materials. By integrating these sensors inside the composite material (as opposed to sensors that are placed on the surface), they allows in-situ measuring of material deformations and monitoring of the integrity of the structure. At the same time, integrating the sensors inside the composite material will protect the FBG from the potentially harsh environment. However, despite these clear advantages, the industry adoption of these FBG sensors in the production and monitoring of composite structures has been lagging due to a practical concern: the location where the fibre enters the composite material, the so called ‘in- or egress’ point, is fragile, and complicates the production process of the composite structure. Typically, once the optical fibre is fractured at the egress point, the connection can not be repaired and the functionality of the embedded FBG sensors is lost. Attempts to make the fibre more robust at the egress point, such as adding tubing or incorporating a discrete optical connector at the composite edge all have their drawbacks[1,2,3]. Typically, they require adaptations to the mould to lead out the fibre or protect the connector, do not allow for trimming of excess material after the composite production and tend to have an impact on the mechanical properties of the resulting composite structure. To tackle these challenges, we present a low-

loss optical connection method that has no impact on the composite production process or mould design, and can be performed after the composite production is complete (including trimming if desired).

1.1 Fibre Bragg grating sensors

The fibre optic sensors applied in this paper are embedded fibre Bragg gratings (FBGs) used for strain measurements in the composite laminate. An FBG is a periodic change of the refractive index of an optical fibre over a certain length (typically 1 to 10 mm). In one single fibre, a large number of sensor points can be multiplexed when multiple FBGs are present in the fibre at different positions. The measuring principle is shown in

Figure 1. When light containing multiple wavelengths is coupled into the optical fibre, only one wavelength of the light is reflected (depending on the effective refractive index and the period of the grating, Λ). When the FBG is elongated the reflected wavelength increases, vice versa when the FBG is compressed the wavelength decreases (a one on one relation exists with the deformation of the FBG). The sensors used in this work are Draw Tower Gratings (DTG[®], [4]).

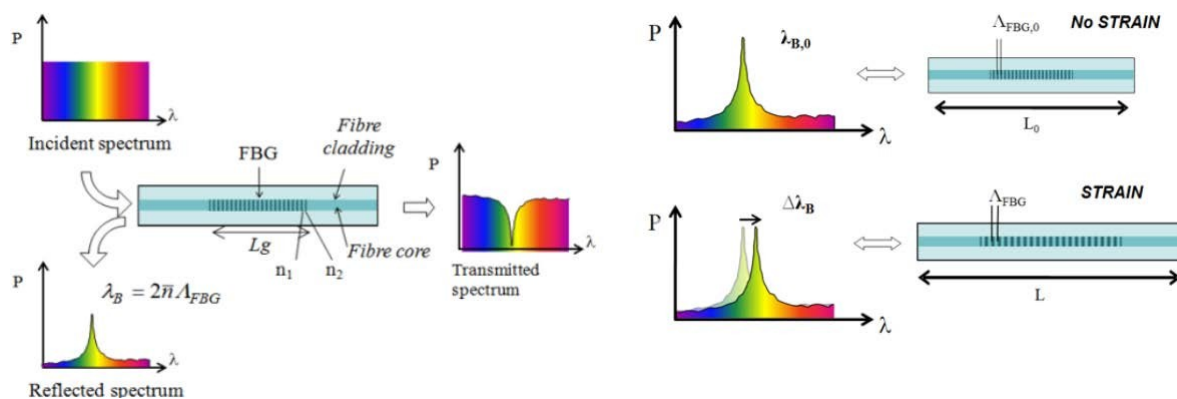


Figure 1 left principle of an FBG sensor, right refracted wavelength of the FBG in unstrained and strained condition (FBGS INT.).

2. PROBLEM DEFINITION AND STATE OF THE ART

2.1 State of the art

Optical fibre sensors embedded in composite materials are of great interest for measuring in-situ material deformations of composite structures. However, because the current fibre optic connection solutions have drawbacks with respect to ease of application, time occupation, installation cost, reparability, and compatibility with the composite production process (distortion), there is still a lack of industry uptake of this technology. The most relevant existing solutions are illustrated in Figure 1 and described below.

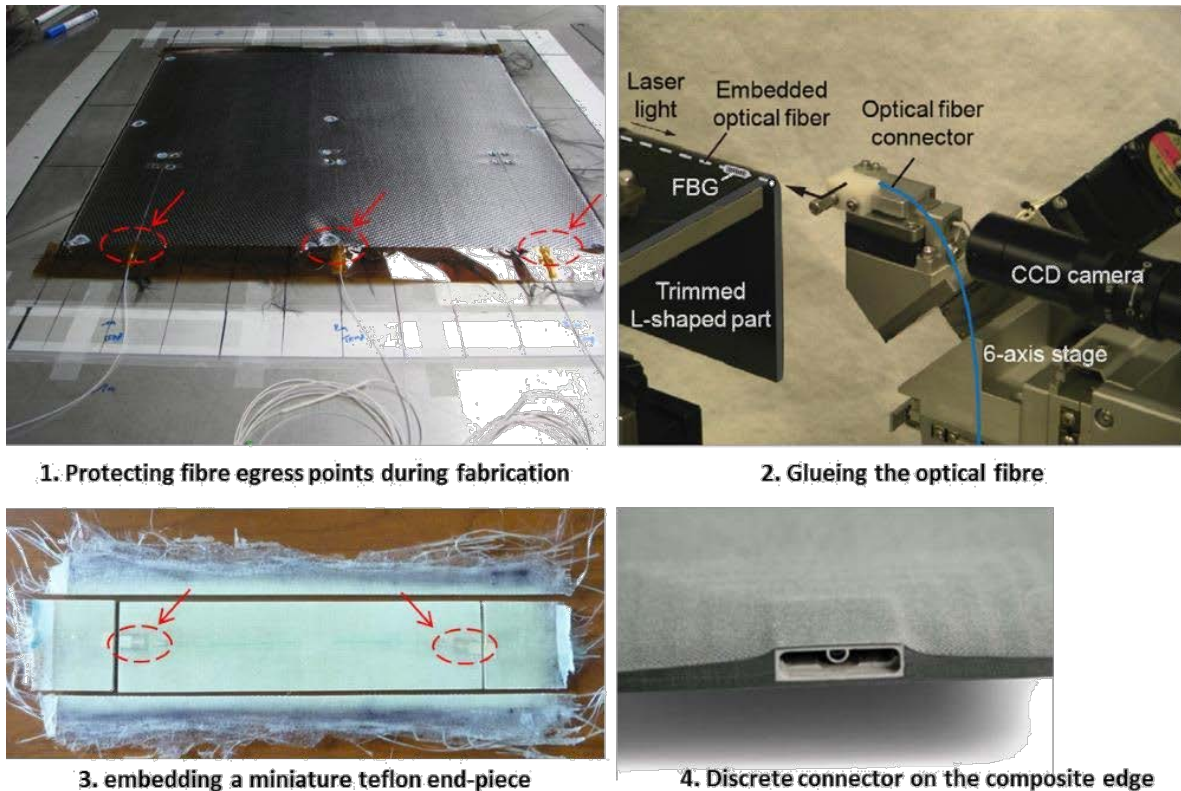


Figure 1. Overview of existing solutions for connecting fibre sensors embedded in composite material.

An overview is given of the existing optical fibre in/egress solutions out of which the challenges for developing a repairable and reliable connection method are defined. The advantages and shortcomings of each method will be discussed.

- Existing solution 1 consists of protecting the entry points with a more rigid material (tube, foil or silicone). This option is cumbersome in terms of production and not all orientations or positions of the embedded fibre are possible. In addition, when using closed mould composite technologies, an adaptation of the mould is needed. Furthermore, it is hardly possible to trim edges.
- Existing solution 2¹ consists of glueing the optical fibre to the composite. An index-matching glue is used to make the connection. Although this method allows for edge trimming of composite and is compatible with the composite production process, the downsides are high fibre coupling losses (in the order of dBs) and the technique is restricted to connecting a fibre normal to the edge of the composite part.
- Existing solution 3² consists of embedding a miniature Teflon end-piece in the composite [4]. This end-piece should exactly be placed in the composite at the position of the edge trimming (small tolerances). The method only allows entry points at the sides of the composite, and although miniature, still distorts the composite at its edges. A previous, bigger version of this technique has already been presented in 2000, see Sjogren, SMS 2000³.

- Existing solution 4 consists of placing discrete connectors on the side or on top of the composite laminate. An overview of these techniques is shown in Green_SMS_1999⁴. There are some recent connectors developed by Deutsch connector⁵. Because of the size of the connectors, there always is undesired distortion of the composite and the method clearly involves extra production steps during the application of the connector (extra reinforcement layers, adaption of moulds,...). Furthermore, only limited edge trimming is allowed not to damage the connectors.

Main challenges of the connection of an embedded fibre sensor and novelty content of the current concept:

- challenge #1: When fabricating composite laminates, pieces or real structures, often the edges of that structure are trimmed prior to use. By trimming the edges, all embedded fibres will normally be cut as well and left without connector. Novelty content: With the method proposed in this document, (re-) connecting of these embedded sensors is possible.
- challenge #2: Ingress/egress techniques existing are mainly based on feed through designs and external fibre coupling. This may involve mould modifications which is not preferred. Novelty content: The method described here will be able to couple the fibre directly at the edge or surface of the composite and allows connecting or repairing of the connection at any time.
- challenge #3: Optical fibre sensors are normally fusion-spliced to so-called “pig tails” which connect the sensor with its read-out device. This typically needs 10 cm of fibre starting from the edge of the composite. Splicing as such is no option when the fibre is broken at the edge of the composite. Novelty content: The proposed method allows “splicing” without needing the fibre to protrude from the composite edge.

2.1 Composite edge-connect

To tackle the above-mentioned challenges, a novel concept is described in this letter which is based on a low-loss optical ‘splice’, which is packaged to ensure mechanical robustness. The technique does not require changes to the composite production process: after production, the embedded fiber is exposed by making a cross-sectional cut, the external fiber is aligned with it and then a direct optical splice is made.

During production of the composite structure, one or more FBG sensor fibres (DTG® technology, from FBGS International) are included at the desired location in the lay-up of the composite structure. The diameter of these DTG sensor fibres is 125 µm, and they are factory-supplied with an Ormocer® coating, leading to total diameter of 195 µm.

After production of the composite structure, the embedded FBG sensor is exposed by making a cross-sectional cut perpendicular to the sensor fibre. The surface is then locally polished using P2400 and P4000 abrasive papers. Then, an external readout fibre, which typically will be a low-cost standard single mode telecom fibre, is actively aligned with the embedded sensor fibre, and a direct ‘optical splice’ is made. Since the numerical aperture and mode field diameter of both types of fibres are different, coupling losses are present when these are directly coupled to each other. The ‘optical splice’ is implemented using an intermediate self-written waveguide (SWW), which connects the 2 fibres. This SWW is formed by launching UV light through the readout fibre while the intermediate space between the sensor fibre and readout fibre is filled

with an appropriate UV curable resin. Due to an increase in refractive index upon polymerization, which starts at the tip of the fibre where the intensity is the highest, a lens-like structure is formed at the end of the fibre tip. This lens-like structure then concentrates the UV light in front of the fibre tip, leading to a progressively growing polymerized region with increased refractive index in front of the fibre forming a waveguide structure.[5] After the formation of the SWW, the assembly is mechanically fixated by gluing a bracket around the edge of the composite, which also provides strain relief to the splice.

3. EXPERIMENTATION AND RESULTS

3.1 Alignment

As mentioned in the introduction, the sensor fibre and connection fibre are actively aligned with each-other using a precision optical stage. The alignment can be either fully manual or be semi-automated. In the case of automated alignment, there is a first coarse manual alignment to bring both fibres within the range of motion of a precision optical stage, which is typically only a few mm. If a redundant connection to the integrated sensor fibre is available, which was ensured during the experimental work below, but is far from guaranteed in practical situations, this coarse alignment can be assisted by shining visible (e.g. red) light through the redundant connection and aligning the beam with the readout fibre. This can be easily accomplished using a low cost USB microscope camera, as shown in **Figure 2**.

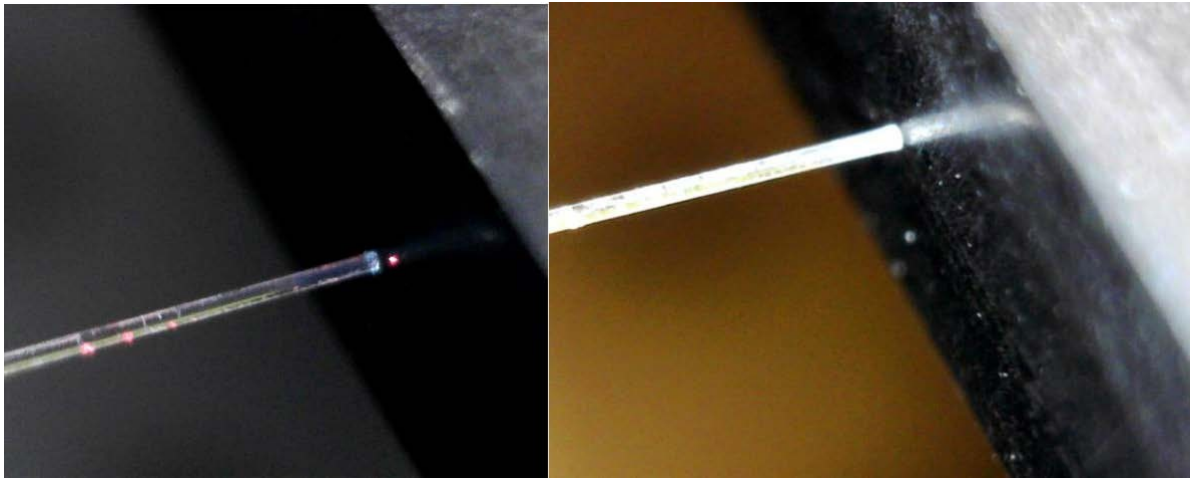


Figure 2 Coarse alignment of readout fibre to sensor fibre integrated in CFRP using visible light from redundant connection(left.) The readout fibre has been stripped and cleaved and has a diameter of 125 μm . When the visible laser is turned off, finding the location of the sensor fibre becomes challenging (right.)

However, when no redundant connection is available, it is fairly difficult to distinguish the 195 μm diameter integrated DTG sensor fibre from the GFRP or CFRP using the USB microscope. This is mainly due to a practical consideration: the camera needs to be placed at an angle, since the readout fibre is blocking the camera from being perpendicular to the cross section. Fortunately, the presence of the readout fibre enables us to locate the embedded fibre. A first potential approach is by taking advantage of the difference in reflectivity between the embedded fibre and the surrounding GFRP or CFRP by measuring the reflected power. An

alternative approach consists of detecting the Bragg peaks in the reflected spectrum. The first approach using the reflected power provides a relatively straightforward measure for the location of the fibre: while scanning an area for the presence of an embedded fibre, each location corresponds with a single value: a measure of the reflected optical power, which does not need to be calibrated and can be easily interpreted by software. This does require the presence of a way to measure the reflected power, such as a circulator combined with a power meter or a fibre coupled photodiode. A second approach is inspecting the reflected spectrum for the presence of Bragg reflection peaks, using an optical spectrum analyzer or a commercial fibre interrogator. This allows for aligning the core of the readout fibre with the core of the sensor fibre using the same hardware that will already be present to interrogate the sensors, but is not as straightforward as it may appear at first. During the alignment process, an air gap is present between the readout fibre and the sensor fibre, which creates a Fabry-Pérot cavity. Because of this, the typical Bragg spectrum peak(s) are superimposed on an interference pattern related to the wavelength and distance between the two end-facets, as shown in **Figure 3**. This somewhat complicates the automation of the alignment, although we are currently having good initial first results with a discrete wavelet-based Bragg peak detection algorithm.

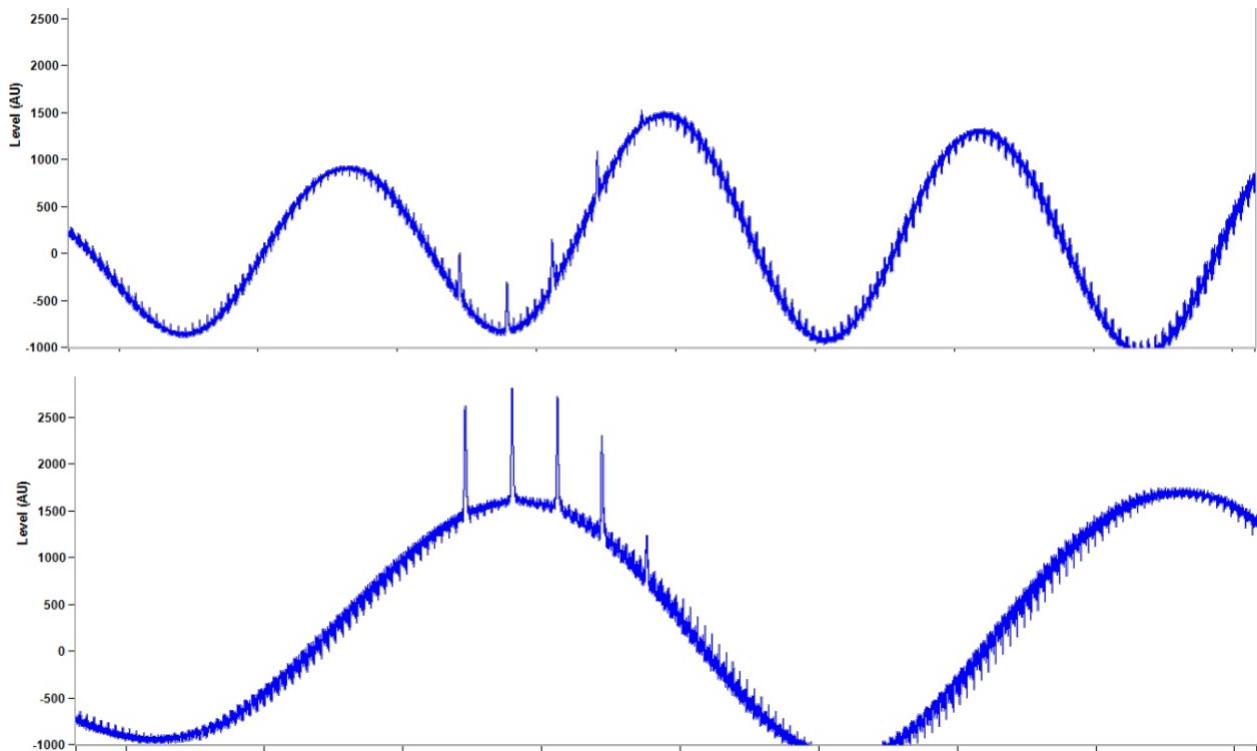


Figure 3 Five Bragg reflection peaks superimposed on Fabry-Perót reflection spectrum for perfectly aligned sensor and readout fibres, with 50 μm separation(top) and in near-contact (bottom)

An example of a reflection signature of an embedded DTG fibre in a composite structure is shown in **Figure 4**(left), while **Figure 4**(right) shows the signature of the wavelet-based Bragg

peak reflection. Note the difference in scale: if the Bragg reflection peaks are used for alignment, only the location of the core is detected instead of the location of the entire fibre.

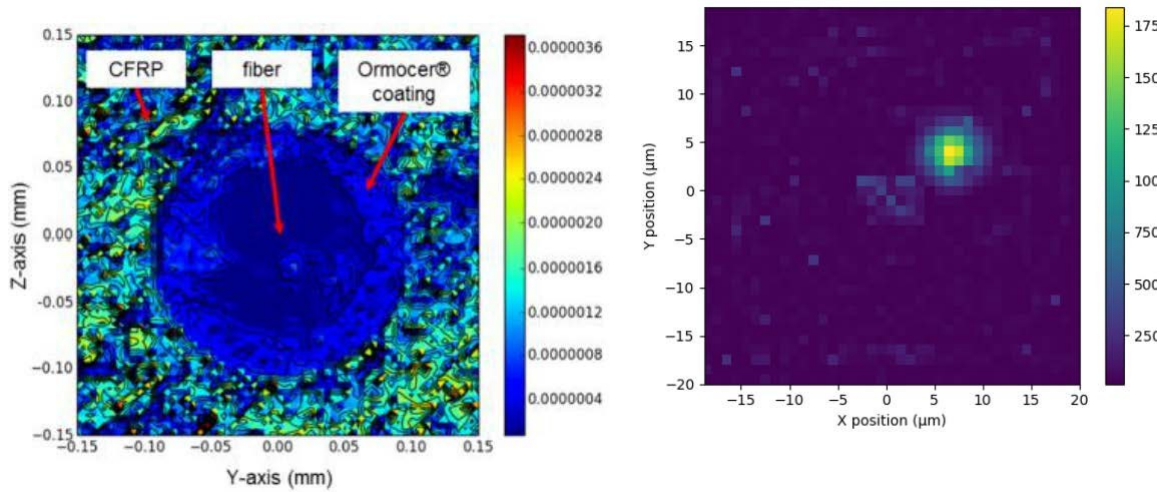


Figure 4 Signature of reflected power (arbitrary units) from scanning over an area containing a DTG fibre (left), signature of sensor fibre core location detection using wavelet based detection algorithm of the Bragg peaks(right). Units are arbitrary, and not comparable between the 2 methods.

3.2 Design and material choice

A certain gap is maintained between both fibres which is filled with a photocurable resin. Experimentally, 50 μm separation was chosen as a good trade-off between quality of the SWW and providing a good optical matching structure between the 2 dissimilar fibre types. During optimization in lab conditions and to monitor the process in real-time, we ensured the presence of a redundant connection to the embedded fibre. This allows for measuring the power that transmitted power instead of just being able to monitor the reflected spectrum.

3.3 Simulations

Using Finite Difference Time Domain (FDTD) simulations with an empirical model of graded-index SWWs, we simulated the ideal SWW RI profile. The correct RI profile is crucial in achieving maximum transmission of the signal between the 2 dissimilar fibres. This is documented in a previous publication[6], and is illustrated in Figure 5. The simulated maximum efficiency corresponds with 0.42dB ($T = 90.7\%$) loss for a 50 μm long SWW, while direct butt-coupling of the 2 fibres leads to a loss of almost 1 dB. In theory, it is possible to increase the transmission to 94.4 % using a 90 μm long SWW, but experimentally this lead to lower quality of the fabricated SWW structures.

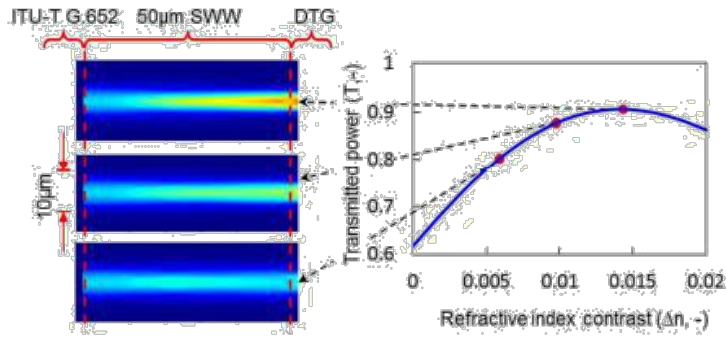


Figure 5 Simulated fraction of transmitted power between connection fibre-SWW (50 μm long)-DTG fibre connection as a function of the refractive index contrast in the SWW. The 2D color plots show the power distribution in a longitudinal cross-section

3.4 Fabrication and measurements

The fabrication parameters of the SWW (illumination power and time) were optimized by evaluating the transmitted power during fabrication (by ensuring the other side of the DTG fibre was accessible and connected to a power meter). Maximum transmission for a 50 μm long SWW was achieved using a 30s illumination time using the fibre coupled laser diode at a power of 20 μW (measured at the tip of the connection fibre), while simultaneously performing a flood exposure from the outside at $5\text{mW}/\text{cm}^2$. To verify the formation of a SWW, the insertion loss was monitored as a function of the illumination time. The reference for this measurement is with both fibres being perfectly aligned with minimal separation (near contact/butt coupling) in the presence of uncured photocurable resin. The initial 1.5 dB at $t=0$ in the graph corresponds with a separation of 50 μm between the 2 fibres, with the gap being filled with photocurable resin. As soon as the illumination is started, the insertion loss rapidly decreases, which confirms the formation of a SWW. Because the energy density of the UV laser light that is coupled through the fibre is much higher than the bulk flood exposure, the SWW is formed before the bulk begins to cure. Initially, this SWW is surrounded by the still-liquid uncured cladding material and has a sufficiently high RI contrast, which allows for the transition between the 2 fibre types to work as it does in simulation. It can be seen that the insertion loss decreases to less than 0 dB, demonstrating the improvement over direct butt-coupling. Unfortunately, in a later phase ($t > 10$ s), the loss increases again, due to the cladding material starting to polymerize with the flood UV exposure, which reduces the RI contrast again. This is an inherent limitation of using the same polymer for core and cladding, as the maximum RI contrast is limited. It is possible to achieve higher contrast by using a 2-polymer approach, where the unexposed and uncured cladding material is removed in a development step and a second type of polymer is applied and cured as the final cladding. However, in practice this approach is not desirable due to the fragile nature of the SWW when the cladding is not present. Even if the minimum theoretical loss cannot be achieved in reality with the photocurable resin we used, the final insertion loss after 30 s illumination is still 0.5 dB lower than the case of direct butt-coupling (i.e. the reference value). Furthermore, the use of an intermediate SWW allows greater connection flexibility. For example, in case the embedded fibre is not cut perpendicularly, the free space region between its end-face and that of the external fibre can be bridged by the SWW.

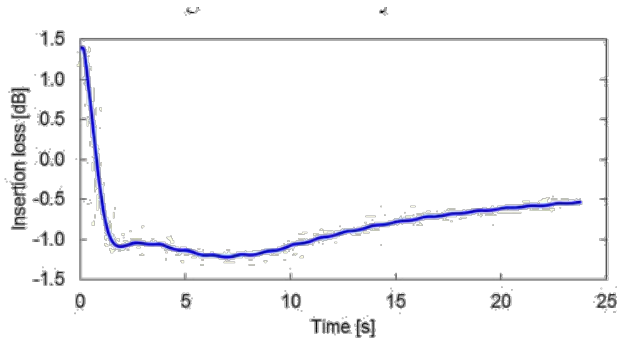


Fig. 4. Insertion loss through an ITU-T G.652 - 50 µm long SWW - DTG fiber connection during SWW fabrication compared to the reference (fibers at 0 µm separation, with uncured NOA68 material in between).

Figure 6 Measured insertion loss during fabrication of SWW

To make the connection between the composite test-piece with the embedded FBG sensors mechanically stable and to provide strain relief, the SWW assembly is protected by a 3D printed bracket.

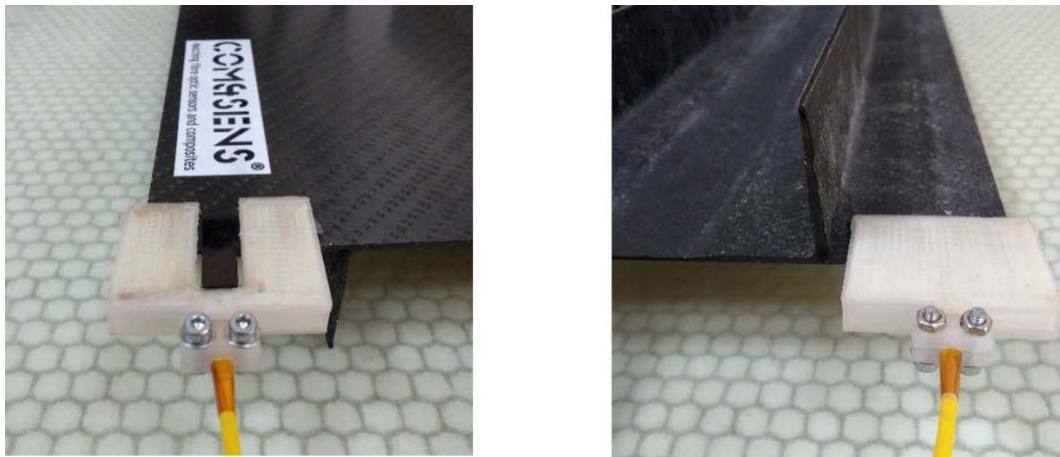


Figure 7 Camera images of a 3d printed bracket to reinforce the SWW connection on a CFRP test-piece with embedded sensors

4. CONCLUSIONS

In this paper, we discussed a method that allows connecting an external read-out fibre to a sensor fibre that is embedded in a composite structure, without requiring any special precautions or modifications during the composite manufacturing process. By using an intermediate SWW between the read-out fibre and the sensor fibre, it is possible to optimize the coupling between these 2 dissimilar fibre types compared to direct butt-coupling. Despite not achieving the theoretically possible connection loss due to limitations of the SWW materials that were used in this work, we have demonstrated that it is possible to produce a high quality optical connection that allows for tracking the signal from the FBG sensors with a commercial interrogator.

5. ACKNOWLEDGEMENTS

This work was supported by the European Space Agency (ESA), under contract nr. 4000114365/15/NL/CBi/GM.

This research was carried out within the project “QUALIFY – Enabling Qualification of Hybrid Joints for Lightweight and Safe Maritime Transport”, co-funded by the INTERREG 2SeasMers Zeeën programme <http://www.interreg2seas.eu/qualify>



6. REFERENCES

1. Kang, H. K., Park, J. W., Ryu, C. Y., Hong, C. S., & Kim, C. G. (2000). Development of fibre optic ingress/egress methods for smart composite structures. *Smart Materials and Structures*, 9(2), 149.
2. Sjögren, A. (2000). Manufacturing technique for embedding detachable fiber-optic connections in aircraft composite components. *Smart materials and structures*, 9(6), 855.
3. Green, A. K., & Shafir, E. (1999). Termination and connection methods for optical fibres embedded in aerospace composite components. *Smart materials and structures*, 8(2), 269.
4. <http://www.fbgs.com/technology/dtg-technology/>
5. Kagami, M., Yamashita, T. & Ito, H. (2001), Light-induced self-written three-dimensional optical waveguide, *Appl. Phys. Lett.*, vol. 79, no. 8, pp. 1079-1081.
6. Missinne, J., Luyckx, G., Voet, E. & Van Steenberge, G. (2017) Low-Loss Connection of Embedded Optical Fibre Sensors Using a Self-Written Waveguide. *IEEE Photonics Technology Letters* 29(20) 1731-1734. 10.1109/LPT.2017.2747630

SYSTEM DEVELOPMENT OF TRANSMITTING CONFORMAL SATCOM ARRAY ANTENNA STRUCTURES(CSAAS)

EMUS 2020

M.-S. KIM^{*}, J.-W. SEO[†]

^{*} Agency for Defense Development (ADD)
Yuseong-gu, Daejeonshi, 34186, South Korea
e-mail: castle@add.re.kr, <http://add.re.kr>

[†] e-mail: jwseo@add.re.kr, <http://add.re.kr>

Key words: Tile Antenna, Housing, Radome, CSAAS

Abstract. This study presents the development results of Conformal SATCOM Array Antenna Structure(CSAAS) for transmitting. Tile Type antenna with 8x8 antenna element array has been developed instead of reflector antenna. 8x8 tile antennas are arrayed on the curved surface with one directional curvature to simulate aircraft skin configuration. Housing has the grid structure to minimize out-of-plane deformation that affects the antenna performances. Tile antennas are attached to the surfaces between grids. Radome is designed as an A-sandwich type to carry some distributed skin load and glass epoxy material with lowest dielectric constant and loss tangent was used for the best electromagnetic performance. One tile antenna is designed with a separate data control and power connection for vertical and horizontal polarization. The static structural strength of the housing and impact strength of the radome were verified by the analysis and tests. Beam pattern test, beam control test and beam steering test are performed in an anechoic chamber for the transmitting CSAAS. The results of structural and electromagnetic tests showed that the design objects met the goal successfully.

1 INTRODUCTION

SATCOM antenna installed on the global hawk, which is the reflector antenna, causes a huge front radome to protect SATCOM antenna. Whereas SATCOM antenna installed on B-2 stealth bomber is a conformal array antenna. Essential planar antenna to compose a stealth aircraft gives a little volume to the aircraft which results in aerodynamic drag reduction, operational efficiency increase and easy structural design, etc. But we barely find the applied aircraft planar SATCOM antenna because the level of difficulties of array antenna design is very high. SATCOM antenna uses geostationary satellite and the distance from geostationary satellite to Korea is 37,000 km which is very long distance to make it consider the area of the planar antenna important.

This study designed and manufactured transmitting conformal SATCOM array antenna structures to verify ground to satellite communication. The structure and the antennas are integrated into one system and the antenna performance test, beam steering test was done in

an anechoic chamber.

The location of the antenna was selected on x-47 based aircraft and the aerodynamic loads were induced. Static structural tests were performed to verify the structural strength of the CSAAS and impact load were applied to verify the impact strength.

2 DEVELOPMENT OF CSAAS

2.1 Requirements

The design objectives of CSAAS are summarized in table 1.

Table 1. Design Object

No.	Item	Design Objective
1	Structural Strength	Carry aircraft skin load
2	Stiffened Structure	Design stiffened grid
3	Antenna Frequency	Ku-band
4	Antenna Type	Tile Type
5	Antenna Performance	45 dBW(EIRP)

※EIRP: Equivalent Isotropically Radiated Power

2.2 Structures

2.2.1 Design

The structure is made of radome and housing as shown in Figure 1. The material of the radome was selected as glass epoxy composite with low dielectric constant and low loss tangent. The electromagnetic wave loss analysis was done for the structure and structural cross section and the distance from radome to the antenna skin with minimum loss was selected. Strength analysis was performed to derive stacking sequence and angles to satisfy impact strength and static strength. The tile antennas are installed into housing using screws and the connectors are attached to the backside of the housing to support data and power. The angle of side structure is decided considering physical interference when the electronic beam steers. Ventilation air holes are provisioned on the side of the housing for cooling the activating the tile antennas.

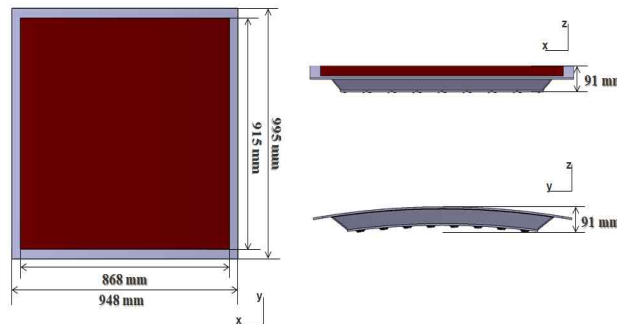


Figure 1. Conformal Array Antenna Structure

2.2.2 Fabrication

Array antenna structures are fabricated using autoclave curing process that includes grids and substructure together. The grids are cut following the grid shape before the curing process and stacked after substructure stacking.

2.2.3 Verification

Structural strength tests are performed for the array antenna structures. Out-of-plane directional deflection tests are performed to derive maximum allowable deflection of Tension/Compression/Shear loads. Figure 2 shows shear load strength test for the array antenna structures. Radome and substructure are integrated and fixed to beam structures. One actuator is connected from the bottom for a shear load and strain gages and displacement gages attached on the radome surface. Structural behaviors of the test are compared with simulation results.



Figure 2. Shear load test setup.

2.3 Antenna

2.3.1 Tile Antenna

Transmitting tile antenna has one PCB(Printed Circuit Board) and four MLBs(Multi-Layer Board) stacked under antenna board. The PCB has 22 layered Rogers substrates and core-chips, power dividers, band path filters and MCU(Main Control Units)s are distributed on it. Transmitting tiles has vertical and horizontal polarizations. Antenna board has core-chips for dual polarization as shown in Figure 3 and LNA(Low Noise Amplifier)s, PS(Phase Shifter)s, and DA(Driving Amplifier)s are located in each core-chips. The tile has 128 core-chips and 8 MCUs that has 1:16 divider.

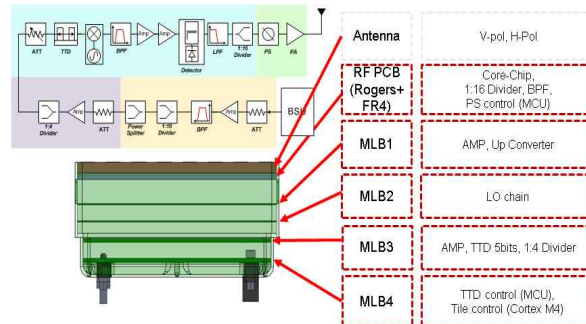


Figure 3. Multi-layered Structure of Transmitting Tile

2.3.2 Array Antenna

Transmitting satellite communication antenna is using Ku-band frequency. The band width is 500 MHz. Figure 4 shows transmitting array antenna system consisted of antenna element, cell, tiles and sectors. Four cell of one tile antenna has L-band frequency transferred from Ku-band. After going through TTD(True Time Delay) and 4:1 power divider the signal goes to sector.

Transmitting signal input starts from analog interface and BSU-T divides after going through ADC(Analog to Digital Converter) as digital signal. DDC/DUC and weighting determines sector level path compensation and polarization direction of transmitting signal. IF analog signals are sent out to sectors.

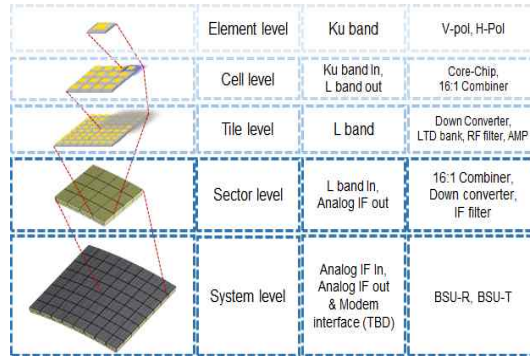


Figure 4. Hierarchical Diagram of Transmitting Antenna

2.3.3 Beam forming simulation

Transmitting array antenna has TTD as beam steering control method. Figure 5 shows simulated contour polarization patterns when the scanning range of antenna steers to several different directions. Main beams to the steered directions are well positioned. The rise of sidelobe level appears to the elevation and azimuth angle direction and makes yellow strand in Figure 5.

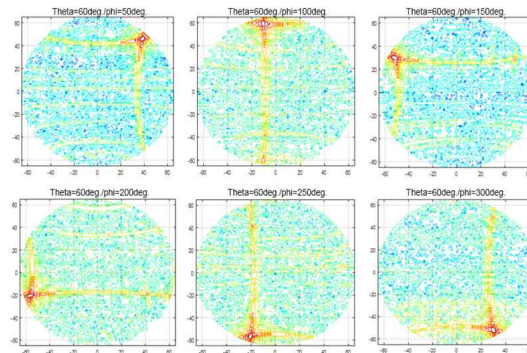


Figure 5. Polarization patterns according to steered main beam direction

2.3.4 Beam Forming Network

The use of simple PS(Phase Shifter) to steer beam direction makes beam difference for the frequencies as shown in Figure 6. That's because phase difference between tile antennas depend upon physical distance between tile antennas. Actually the phase difference for the

physical distance varies according to the operating frequencies. To compensate the time delay of phase path between antennas, TTD(True time delay) device should be used.

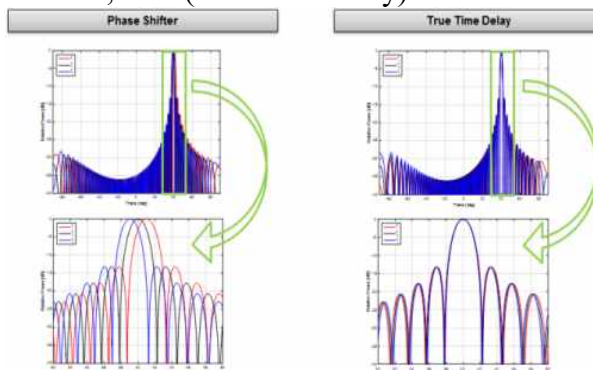
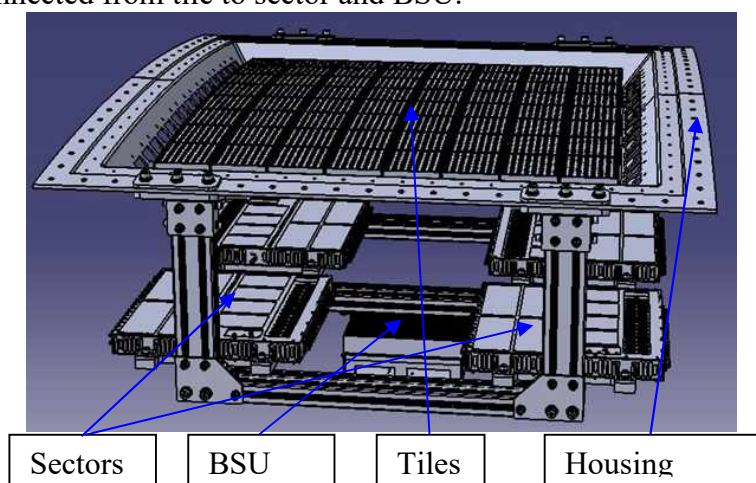


Figure 6. Beam squint comparison for PS and TTD devices

2.4 CSAAS Integration

2.4.1 Mechanical Integration

Transmitting tile antennas are installed into the bottom of housings. 64 transmitting tiles are fixed using screws and connectors are hooked to the sectors and BSU. Signal cables and power cable are connected from tile to sector and BSU.



2.4.2 Antenna System Calibration

After calibration of each 64 tile antenna, one calibration for one phase of 64 tile antenna system is performed. Phase control devices are applied for the tile level because the calibration of the core-chip in the tiles are finished.

2.4.3 Antenna System Performance

Figure 9 shows RF block diagram from tile to element antenna. RF signal from sector goes to 64 tiles and each tile has 1:4 power divider before cell. One cell has polarization signal 1:16 power distributor after TTD, amp, frequency converter and filter and signal goes to antenna element through core-chip. Transmitting array antenna has 4,096 antenna elements,

8,192 core-chips and 512 frequency converter. The test result for EIRP in an anechoic chamber shows 68 dBW. Figure 10 shows far-field horizontal polarization pattern for Azimuth angle 0° and elevation angle 60°. Figure 11 shows far-field vertical polarization pattern for Azimuth angle 0° and elevation angle 30°.

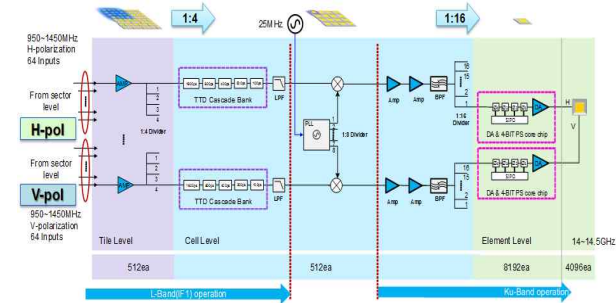


Figure 9. RF Block diagram from Tile Input to Patch Antenna

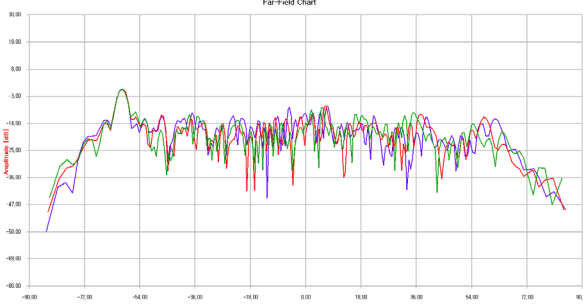


Fig. 10. Horizontal Pattern for Azi. 0°, Elev. 60°

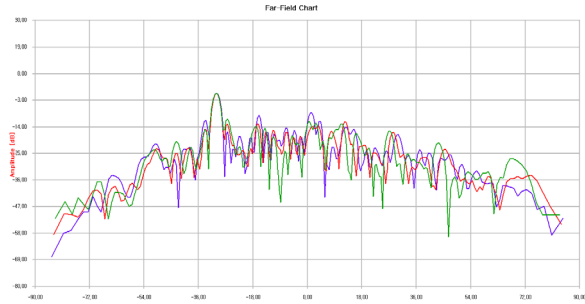


Fig. 11. Vertical Pattern for Azi. 0°, Elev. 30°

3. Conclusion

Conformal SATCOM array antenna structures are designed, fabricated and integrated into a transmitting conformal array antenna structures that can be installed into an aircraft. Mechanical performances are satisfied by designing housing as orthogrid structure and mechanical/electromagnetic performance are satisfied by installing tile antennas between grids. Impact strength is satisfied by designing radome as a-sandwich structures. Transmitting antenna can actively steer the beam from 0° to 60° maintaining beam-width. We verified all the requirements of CSAAS are met by tests.

REFERENCES

- [1] Baek, S.M., Go, M.G., Kim, M.S. and Joo, Y.S. *Structural Design of conformal load-bearing array antenna structures(CLAAS)*. Advanced Composite Materials, Vol. 25, (2017):29-42.
- [2] Mackenzie, Anne I., *Electromagnetic Modeling for the Conformal Lightweight Antenna System for Aeronautical Communications Technologies(CLAS-ACT) Program: Final Report. NASA/TM-2019-220293, NASA Langley,(2019).*

DEVELOPMENT OF A NUMERICAL FRAMEWORK FOR VIRTUAL TESTING TO SUPPORT DESIGN OF A NEXT GENERATION THERMOPLASTIC MULTIFUNCTIONAL FUSELAGE

EMUS 2020

B.H.A.H. TIJS*[†], K.S. VAN DOOREN[†] AND C. BISAGNI[†]

* GKN Aerospace Fokker
Industrieweg 4, 3351 LB Papendrecht, The Netherlands
e-mail: bas.tijs@fokker.com, web page: <https://www.gknaerospace.com/>

[†] Faculty of Aerospace Engineering, Aerospace Structures and Computational Mechanics
Delft University of Technology
Kluyverweg 1, 2629 HS Delft, The Netherlands
Web page: <https://www.tudelft.nl/en/ae/>

Key words: Numerical framework, Thermoplastic Composites, Virtual Testing, Welded Joints, Design

Abstract. This work summarizes the recent developments of a numerical framework to predict the mechanical behaviour of thermoplastic composites. It supports the design of a next generation thermoplastic multi-functional fuselage which uses advanced joining techniques such as thermoplastic welding to reduce both weight and cost by limiting the amount of mechanical fasteners required. At the lower end of the testing pyramid the framework is able to accurately predict typical preliminary design allowables such as laminate, open-hole and welded joints strength through a high-fidelity modelling approach. This information is then passed on to the structural level in a validated building-block approach to efficiently virtual test the compression strength of fuselage panels during post-buckling while also taking into account the influence of damages at the skin-stiffener interface.

1 INTRODUCTION

A numerical framework is currently in development to accurately predict matrix-dominated failure of thermoplastic composites and welded joints. It supports the design of a next generation thermoplastic multi-functional fuselage which uses advanced joining techniques such as thermoplastic welding to reduce both weight and cost by limiting the amount of mechanical fasteners required. However, using new thermoplastic composite materials and aiming for fastener-free joints also introduces new challenges. The strength of the highly loaded welded joints rely on the performance of the matrix and this matrix is strongly influenced by the manufacturing process. Furthermore, the state-of-the-art in modelling techniques is mostly developed and validated on thermoset composites, which show a more brittle failure behaviour [1]. The methodology to tackle these challenges is taking into account the constitutive material behavior of thermoplastic composites and accounts for the appropriate failure mechanisms

through the different scales of the conventional physical testing pyramid (Figure 1). At the lower end of the testing pyramid, simulations take into account the physical mechanisms of damage and nonlinearity at the lamina level through a high-fidelity modelling approach. Modelling of the coupons is automated by means of Python scripting to allow for rapid generation of virtual allowables. Higher up the testing pyramid, at structural detail and panel level, it is not computationally efficient to model the composite structure in full detail. At this scale the emphasis is at global structural behaviour, for example during (post)buckling, and the performance of critical interfaces such as the welded skin-stiffener interface are of high importance. Separation of the welded skin-stiffener interface is modelled by the use of the Virtual Crack Closure Technique, both for damaged and pristine interfaces, allowing for large mesh sizes [3]. This allows for efficient modelling of skin-stiffener separation, even at the component level. Use is made of a virtual building block approach to ensure the validity of the methodology at each scale and corresponding critical failure mode.

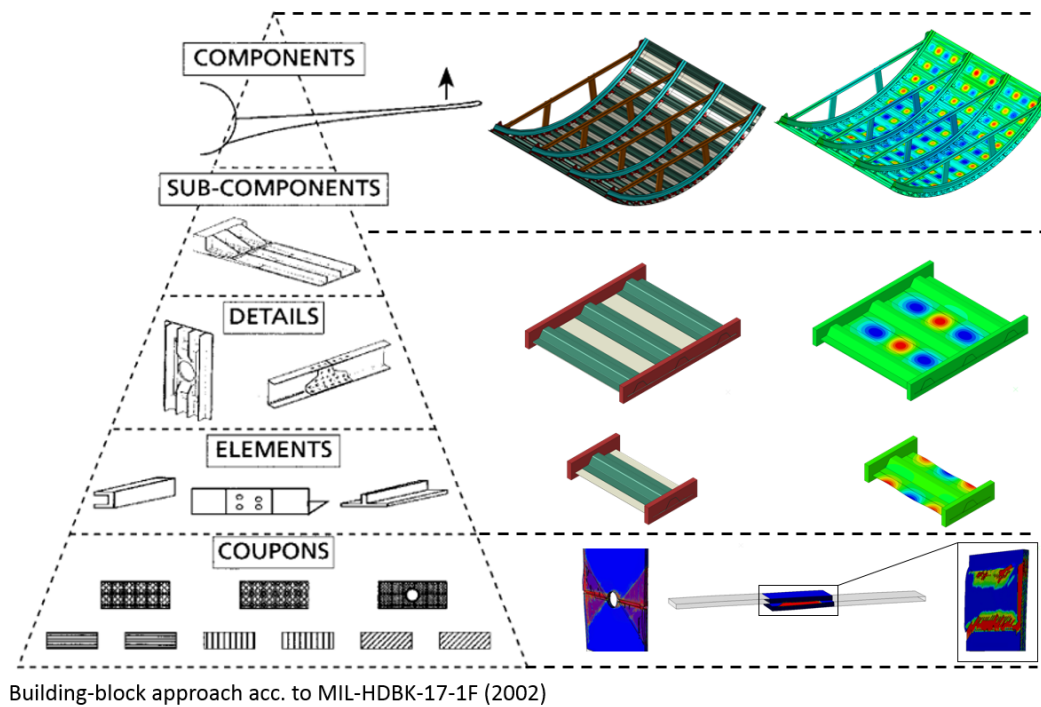


Figure 1: Virtual testing building block approach for thermoplastic composites

2 NUMERICAL FRAMEWORK FOR VIRTUAL COUPON TESTING

The numerical framework for Virtual Coupon Testing has been implemented through the use of the programming language Python using ABAQUS scripting commands to automatically generate coupon tests according to a given test matrix. This test matrix contains all user-defined input such as the test standard, specimen geometry and material data. The ABAQUS/Explicit finite element solver is selected for the coupon simulation, as it involves solving a highly nonlinear dynamic problem. This includes large displacements, non-linear material behavior including

damage and complex contact interaction with damage and frictional behavior. The high-fidelity modelling approach and constitutive material model for thermoplastic composites is briefly explained in the next sections.

2.1 High-fidelity modelling approach

The modelling of the coupons follows a high-fidelity approach where each ply is discretized using a fiber aligned meshing technique [1] that behaves according to the constitutive material models briefly explained below. The plies are therefore modelled as separate parts and surface based general contact is used to facilitate the non-conformal meshes of each part as shown in Figure 2. The boundary conditions are applied by means of a velocity amplitude profile imposed at the top and bottom surfaces in the case of standard uni-axial loading.

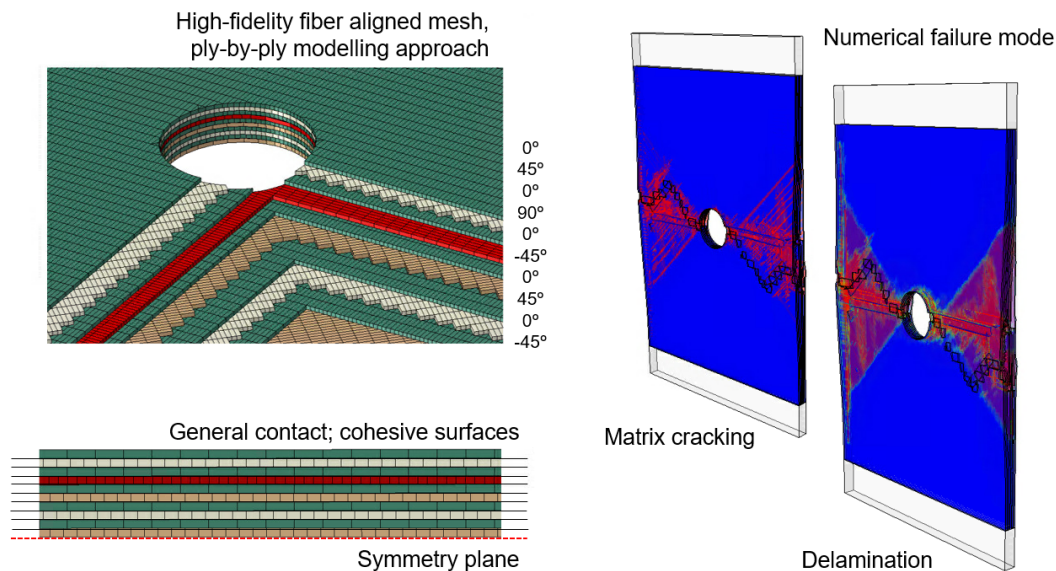


Figure 2: High-fidelity modelling approach and predicted open-hole failure mode

2.2 Constitutive material model for thermoplastic composites

The constitutive material model for thermoplastic composites consists is implemented in a user-defined subroutine "VUMAT" as a Continuum Damage Model. The model takes into account three-dimensional stress states and is based on the deformation gradient to account for large shear deformations within the failure modes. This is important for accurate prediction of matrix dominated failure modes such as ply splits [2] as can be observed in the results shown in Figure 2. The laminate compliance tensor is affected by the damage variables in each orthotropic direction and is associated with the damage evolution laws for each failure mode. Exponential softening laws are used to ensure physically correct dissipation of fracture energy for each failure mode. Nonlinear elastic-plastic behavior of the matrix is modelled for both in-plane and out-plane shear response based on Ramberg-Osgood laws [1].

The interlaminar behavior is modelled by means of the build-in ABAQUS/Explicit general contact algorithm which takes care of the kinematics of surface contact, frictional and cohesive behavior. Damage initiation is predicted by using a quadratic nominal stress failure criteria. Once damage is initiated, the cohesive zone model allows for the correct dissipating of fracture energy corresponding to the specific mixed-mode opening mode. Frictional effects of the delaminations are also considered.

2.3 Experimental validation

Virtual test were performed and compared to a large variety of experimental results that include plain material strength, open-hole strength and single-lap shear joint strength of welded joints. Both the progressive failure mechanisms and the failure load are predicted with high accuracy with respect to the results obtained experimentally. Figure 2 shows the predicted matrix cracking and delaminations in an open-hole tensile test and Figure 3 demonstrates the progressive failure of a thermoplastic welded joint. The joint strength is highly influenced by the failure mechanisms of not only the welded interface but also the back-up plies which is important to consider when modelling simplifications are made at the structural level.

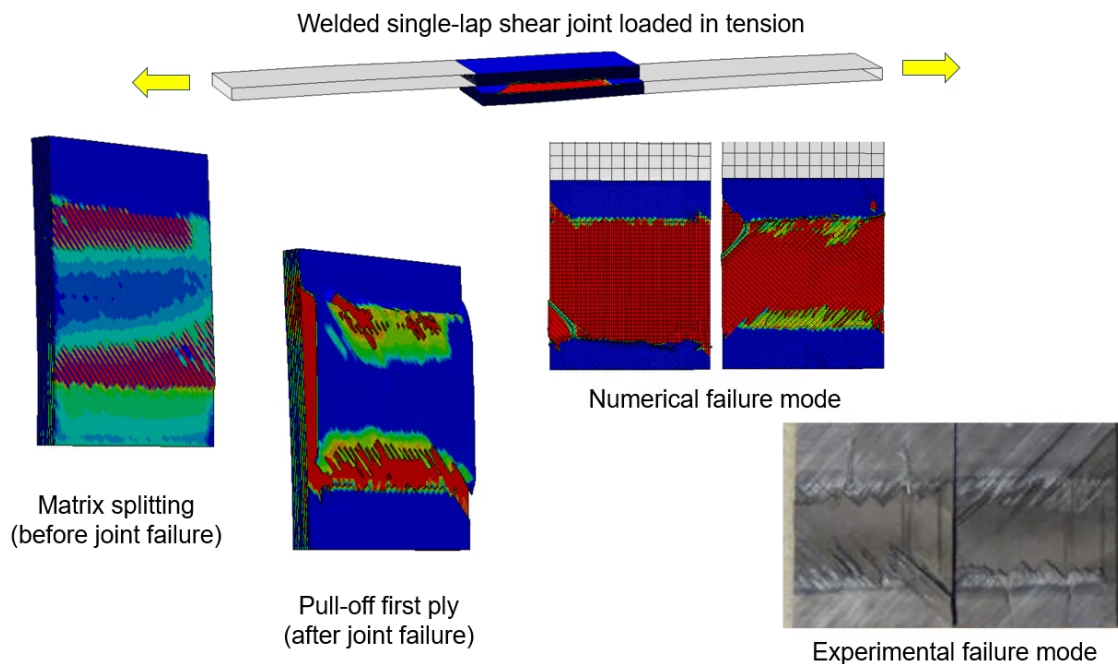


Figure 3: Virtual Coupon Test results of welded single-lap shear joint

3 VIRTUAL STRUCTURAL TESTING

The numerical framework for Virtual Structural Testing covers the structural detail, element and (sub)component level as shown in Figure 1. At this scale, the emphasis is on predicting the resulting (post)buckling strength due to compression loading and the failure behavior of the welded skin-stringer interface. The framework utilizes the ABAQUS/implicit dynamic solver

for the finite element analysis and python coding is used to account for measured geometrical imperfections.

3.1 Modelling approach to predict skin-stringer separation of welded joints

Skin-stringer separation is modelled by means of the Virtual Crack Closure Technique (VCCT) in combination with the Benzeggagh Kenane criteria for mixed mode interface behavior. The use of VCCT allows for a coarser mesh compared to other interface methods, which is a major advantage when modelling large structures. The restriction of VCCT is its requirement for a pre-crack, which normally prevents it from being used for pristine structures. However, the unwelded areas on both sides of the welded joint can be modelled as a pre-crack to limit this restriction (Figure 4a). Furthermore, information on the material strength of the skin and stringer may be taken from predictions at the lower scale in order to avoid computationally expensive analyses at the structural level.

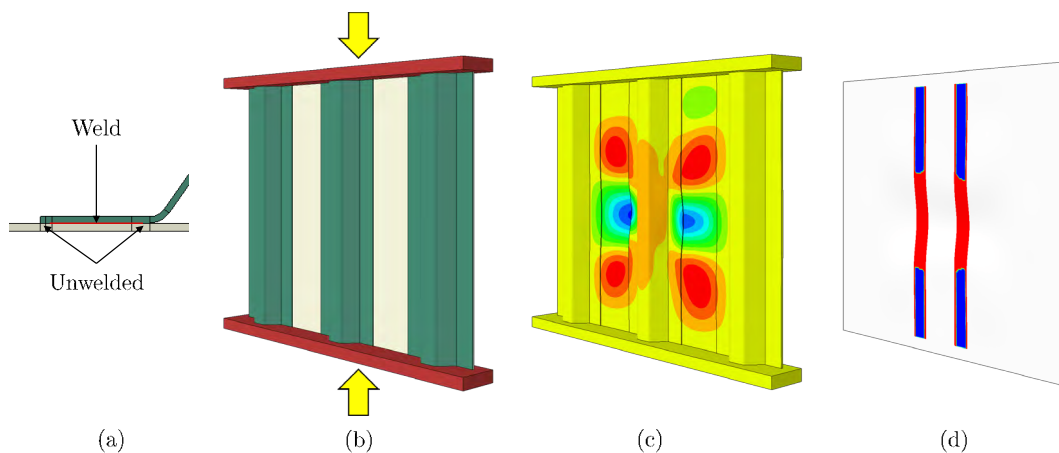


Figure 4: (a) Modelling strategy for welded interface; (b) Multi-stringer panel under compression; (c) Opening of skin-stringer interface; (d) Interface failure.

3.2 Design support of the Next Generation Thermoplastic Multifunctional Fuselage

The new numerical framework for Virtual Testing may be used to form the basic building-blocks early on the design process when new materials and design concepts are used. In the case of the Next Generation Thermoplastic Multifunctional Fuselage, this involves both thermoplastic composites and welded joints. Developing the simulation strategy to virtual test structural (sub)components such as compression panels of a new product follows both a top-down and bottom-up strategy. At the top level, the loading conditions and design requirements are defined and simulations at the component level provide input about the expected mechanical behavior at the (sub)structural level. For the case of the new fuselage, which consists of a lightweight thermoplastic composite stiffened structure that is joined with welding, the main concerns are related to the strength of these joints during complex loading conditions such as (post)buckling and the capability of the structure to be tolerant to damages at these interfaces. Knowledge from the bottom-up material design allowables and failure modes is therefore linked with the

top-down requirements to design structural detail and elements that will cover these loading and damage scenarios. Examples of virtual structural tests that may be designed are single- and multi-stiffener compression panels that could also include damages at the welded interface based on impact scenarios. Example of these models are shown in Figure 1 and 4. The aim of this strategy is to verify and validate the analysis methods at the lower scale and predict the effect of damage at the higher scale under various loading or damage conditions, as physical testing every possible configuration is too expensive. Through this strategy the efficiency of new joining techniques and material behavior can be explored while at the same time it may reduce the risks of introducing new design concepts early on in the design phase. This rapidly increases the design knowledge and allows for a smarter design of the physical tests.

4 CONCLUSIONS

It is demonstrated that the new numerical framework for Virtual Testing can support accurate predictions of the failure of thermoplastic composites and welded joints through the different scales of the physical testing pyramid. It can provide the basic design building-blocks when availability of experimental data and design knowledge is limited and allows for a smarter design of the physical tests later on in the design process.

5 ACKNOWLEDGEMENTS

This work is part of the STUNNING project and has received co-funding from the Clean Sky 2 Joint Undertaking (JU) under grant agreement No 776455. The JU receives support from the European Union's Horizon 2020 research and innovation programme and the Clean Sky 2 JU members other than the Union.

6 DISCLAIMER

The results, opinions, conclusions, etc. presented in this work are those of the author(s) only and do not necessarily represent the position of the JU; the JU is not responsible for any use made of the information contained herein.

REFERENCES

- [1] Falcó, O., Ávila, R.L., Tijs, B. and Lopes, C.S. Modelling and simulation methodology for unidirectional composite laminates in a Virtual Test Lab framework. *Composite Structures* (2018) **190**:137–159.
- [2] Tijs, B.H.A.H., Turon, A. and Bisagni, C. The importance of accounting for large shear deformation on modelling matrix failure of thermoplastic and thermoset composites. *Proceedings of the 7th ECCOMAS Thematic Conference on the Mechanical Response of Composites (COMPOSITES 2019), Girona, Spain, Sept. 18-20 (2019)*.
- [3] van Dooren, K.S., Labans, E., Tijs, B.H.A.H., Waleson, J.E.A., and Bisagni, C. Analysis and testing of a thermoplastic composite stiffened panel under compression. *Proceedings of the 22nd International Conference on Composite Materials (ICCM22), Melbourne, AU, Aug. 11-16 (2019)*.

INFLUENCE OF THE ANGLE BETWEEN ADHERENDS ON ULTRASONIC WELDING OF THERMOPLASTIC COMPOSITES

EMUS 2020

C. B. G. BRITO*, J. TEUWEN*, C. DRANSFELD* AND I. FERNANDEZ VILLEGAS*

* Aerospace Structures and Materials Department, Faculty of Aerospace Engineering
Delft University of Technology
Kluyverweg 1, 2629 HD Delft, the Netherlands
e-mail: C.Brito@tudelft.nl

Key words: Misalignment, Manufacturing, Joining, Tolerances, Strength

Abstract. Research on ultrasonic welding of composites has focused mostly on studying parameters that are inputs for the process or material-related parameters, but almost no attention has been given on the effect of manufacturing tolerances. In this work, we investigated how an angle between adherends impacts the welding process and the weld quality. By increasing the angle between top and bottom adherends, it was found that the duration of the process increased while the power consumed, the weld uniformity and the weld strength decreased. However, by increasing the clamping distance, which increased the compliance of the adherends and hence their ability to deform under the applied welding force, the effect of the misalignment on both the welding process and weld quality could be substantially reduced.

1 INTRODUCTION

Ultrasonic welding is a fusion bonding method that uses high-frequency low-amplitude vibrations to generate heat in the interface to be bonded. It is well known how processing parameters such as welding force and amplitude of vibration affect the process [1,2], but almost no attention has been given to the influence that manufacturing tolerances can have on it, such as a misalignment between adherends, which could cause uneven heating of the overlap [5], potentially leading to a heterogeneous melting of the overlap area and impacting the final quality of the joint. Although the need of parallelism between adherends is usually mentioned [3,4], no further investigation has been found in literature until this point. Understanding the influence of a misalignment between the adherends is essential to allow the industrialization of this process, such as for its use on the Multifunctional Fuselage Demonstrator of the Clean Sky 2 project [6].

In this work, we investigate the influence that an angle between adherends may have on the ultrasonic welding process. A clamping jig composed by two metal bars as clamps and flat energy directors (ED) were used. The distance from the clamps to the sonotrode and the thickness of the base under the top adherend were varied in order to obtain a variety of angles between adherends, which was quantified using side-view pictures of the welds. The effects on the welding process were assessed by analysing the consumed power and the vertical displacement of the sonotrode during welding. Single-lap shear strength tests and fracture surfaces were used to evaluate the homogeneity and quality of the welds.

2 METHODOLOGY

The material used to manufacture the specimens was Toray Cetex® TC1200 carbon 5-harness satin fabric reinforced polyetheretherketone (C/PEEK) from TenCate Advanced Composites (the Netherlands) (*T300JB 3K Carbon 280gsm FAW 5HS Woven Fabric Reinforced Laminate 42% RC*). The laminate stacking sequence was $[(0/90)_3]_s$, consolidated in a hot platen press at 385°C and 10bar for 30min, resulting in a final nominal thickness of 1.9mm. Single lap shear coupons of 25.4mm x 101.6mm were cut with a water-cooled diamond blade from the consolidated laminates. The apparent main orientation of fibers was kept parallel to the longitudinal direction of these coupons. A 0.25mm thick flat film of pure PEEK was used as ED.

The specimens were welded with a 20kHz Herrmann Ultraschall ultrasonic welder machine with 1:2 booster and 1:1.7 sonotrode. Amplitude of vibration was 86.2µm peak-to-peak. The static welding force was 500N and consolidation force was 500N for 4s. Displacement control was used, i.e. the duration of the vibration was defined by the downward displacement of the sonotrode. The consumed power and vertical displacement of the sonotrode during the vibration phase were given by the welding machine as outputs at the end of the process. The in-situ monitoring method described by Villegas [1] was used to define the onset of flow and the optimum displacements. Figure 1 shows the jig used to hold the samples during the welding process. The distance between sonotrode and top clamp (*clamping distance*, CD) was either 5mm or 50mm and five supporting base thicknesses (BT) were tested. The nomenclature CD (mm)/BT (mm) is used when mentioning the different clamping configurations. Pictures perpendicular to the center of the overlap were taken with a high resolution camera. ImageJ was used to measure the angle between top and bottom adherends (Figure 2).

Single-lap shear strength (LSS) tests were performed with a Zwick/Roell 250kN universal testing machine and a cross-head speed of 1.3mm/min. Naked-eye fractographic analysis was performed after testing. When needed, cross section microscopic analysis of as-welded samples was performed using a Keyence VH-100UR digital microscope.

3 RESULTS




Varying CD and BT resulted in a misalignment between top and bottom adherends, which was quantified as the angle between the top and bottom adherends after the sonotrode applied the static force of 500N (Figure 3). For the shorter CD (5mm), one can see that the angles are higher and the rate in which the angles increase with decreasing BT is higher than for 50mm CD.

Typical power curves stopped at the onset of the ED squeeze flow are shown in Figure 4. When decreasing BT, a general increase in the time required for the ED to start flowing (*time to flow*) and a decrease in the maximum consumed power (*power peak*) occurred. These two effects are more pronounced for 5mm CD. Decreasing BT from 2.15 to 1.25mm increased the time to flow more than 10 times and decreased the power peak more than 75% for 5mm CD. However, a change in BT from 2.15mm to 0.00mm increased time to flow only 5 times and caused a 50% decrease in the power peak for 50mm CD.

The cross-sectional micrograph in Figure 5 corresponds to the onset of the flow of the 1.25/5 configuration. One can see that the state of the weld and of the adherends is highly non uniform from edge to edge of the welding overlap. At one edge, intact ED is seen while at the opposite edge the ED cannot be identified anymore and severe squeeze flow and porosity can be seen in the adherends. The transition between those two opposite edges shows a gradual increase in the number of voids in both adherends.

Finally, Table 1 shows the fracture surfaces and the results of the LSS tests for welds made with 50mm CD and different BT. Decreasing BT from 1.90mm to 1.50mm led to a decrease in LSS of 5%, while further decreasing BT to 0mm decreased LSS by 16%. All fracture surfaces were fairly uniform. Both the optimum sonotrode displacement and the corresponding vibration time were affected by the angle, which consistently increased with decreasing BT.

Table 1: Fracture surfaces, single-lap shear strength test results, optimum displacement (d_{opt}) and total duration of the process for welds with 50mm CD and different BT.

Fracture surfaces			
Case	1.90/50	1.50/50	0.00/50
Angle [°]	0.20 ± 0.08	0.58 ± 0.02	2.00 ± 0.04
LSS [MPa]	50.81 ± 2.25	48.04 ± 1.48	42.56 ± 1.76
d_{opt} [mm]	0.10	0.07	0.03
Time [ms]	994.33 ± 28.43	857.00 ± 1.41	2206 ± 259.93

4 DISCUSSION

Figure 6 plots time to flow and power peak versus angle. A general trend is observed, where time to flow increases and power peak decreases with increasing angle. However the fitting seems to be sensitive to the CD. This is believed to be a result of the fact that the angle measured outside of the overlap does not take into account the effect of the CD on the deformation of the adherend within the overlap. Indeed, the portion of the top adherend that is under the sonotrode will deflect (δ) according to Equation 1, where P is the applied force (500N), l is the arm length (i.e. CD), E the Young's modulus and I the second moment of area:

$$\delta = \frac{Pl^3}{3(EI)} \quad (1)$$

The misalignment between top and bottom adherends is believed to result in part of the amplitude of vibration being invested in closing the angle between top adherend and ED that remains after the welding force is applied. This loss in the amplitude will decrease the cyclic strain the ED is subjected to during the welding process. Decreasing the cyclic strain results in lower friction and viscoelastic heating rates [7,8], which will consequently increase the time required to take the ED to its melting temperature (time to flow) and decrease the power consumed by the process. However, according to Equation 1, a larger deflection will occur for longer CD, resulting in the top adherend having a higher compliance and, hence, better conforming to the ED and bottom adherend. Thus, a case with longer CD will potentially present higher intimate contact and a smaller angle between top adherend and ED, which leads to a smaller portion of the amplitude of vibration invested in closing the remaining angle. The fact that both the 1.90/5 and the 0.00/50 configurations featured similar time to flow and power peak despite significant different angles (0.95° and 2.00° , respectively, see Figure 6) supports this reasoning. It is believed that under the static force applied by the sonotrode, the top adherend in

the 0.00/50 configuration deflects more than the adherend in the 1.90/5 configuration, compensating for the initial larger angle and resulting in a similar remaining angle.

Additionally, the micrograph in Figure 5 shows highly non-uniform heating within the overlap at 5mm CD. At the onset of the flow, one edge showed signs of overheating while the opposite edge had intact ED. Thus, one can expect that optimum welds cannot be achieved for such cases. Contrarily, the fracture surfaces corresponding to different BT at 50mm CD (Table 1) presented an uniform aspect. Neither unwelded areas nor fibre distortions and voids could be observed on the fracture surfaces. Accordingly, the welds featured high single-lap shear strength values. These results seem to indicate that increasing CD not only reduces the impact of an angle between adherends on the process, but also on the weld uniformity and strength.

5 CONCLUSIONS

In this paper, the influence of the angle between adherends on ultrasonic welding of CF/PEEK adherends with flat energy directors (ED) was investigated. The position of the top clamp and the thickness of the supporting base in the welding jig were varied in order to obtain a wide range of angles. The main observations were that with increasing angle the time needed for the ED to start flowing increased while the maximum consumed power and the uniformity at the weld interface decreased. Apart from the angle, the clamping distance had an effect on these results since it influences the compliance of the top adherend and consequently the actual amplitude transmitted to the ED and which is invested in heat generation. A clamping distance of 50mm was enough to diminish the misalignment effects, providing high weld strength and uniform weld quality even under significant adherends misalignment, which shows that ultrasonic welding is a promising method for aerospace applications such as in the Multifunctional Fuselage Demonstrator from Clean Sky 2 project.

ACKNOWLEDGEMENT

The work presented in this paper is carried out as part of a project, which has received funding from the Clean Sky 2 Joint Undertaking (JU) under the European Union's Horizon 2020 research and innovation programme under grant agreement No 776455.

DISCLAIMER

The results, opinions, conclusions, etc. presented in this work are those of the author(s) only and do not necessarily represent the position of the JU; the JU is not responsible for any use made of the information contained herein.

REFERENCES

- [1] Villegas, I.F. In situ monitoring of ultrasonic welding of thermoplastic composites through power and displacement data. *J. Thermoplast. Compos. Mater.* (2015) 28(1):66-85.
- [2] Villegas, I.F. Strength development versus process data in ultrasonic welding of thermoplastic composites with flat energy directors and its application to the definition of optimum processing parameters. *Compos. Part A.* (2014)65:27-37.
- [3] Palardy, G. et al. A study on amplitude transmission in ultrasonic welding of thermoplastic composites. *Compos. Part A.* (2018)113:339-349.

- [4] Zhao, T. et al Towards robust sequential ultrasonic spot welding of thermoplastic composites: Welding process control strategy for consistent weld quality. *Compos. Part A.*(2018)109:355-367.
- [5] Eveno, E.C. and Gillespie, J.W. Jr. Experimental investigation of ultrasonic welding of graphite reinforced polyetheretherketone composites. *Proceedings of the National SAMPE Technical Conference, Atlantic City, NJ, USA* (1989).
- [6] S.L. Veldman et al., "Development of a multifunctional fuselage demonstrator", *Aerospace Europe Conference*, Bordeaux (2020).
- [7] Tutunjian, S. et al. A control method for the ultrasonic spot welding of fiber-reinforced thermoplastic laminates through the weld-power time derivative. *J. Manuf. Mater. Process.* (2018)3(1).
- [8] Levy, A. et al. Modeling of the heating phenomena in ultrasonic welding of thermoplastic composites with flat energy directors. *J. Mater. Process. Technol.* (2014)214:1361-1371.

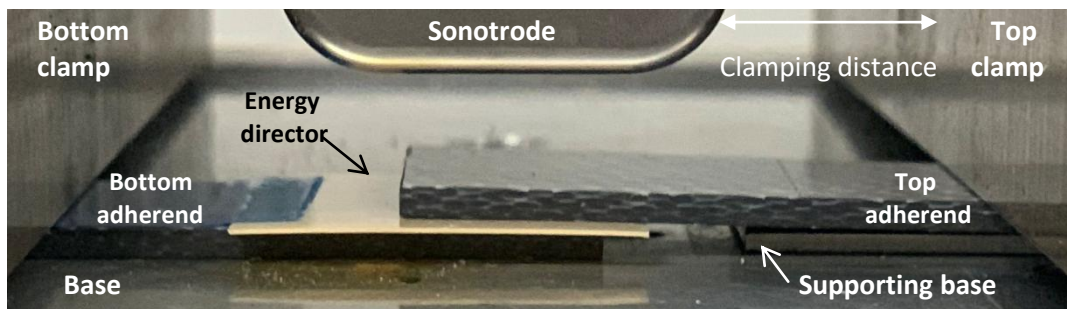


Figure 1: Setup of static ultrasonic welding process.

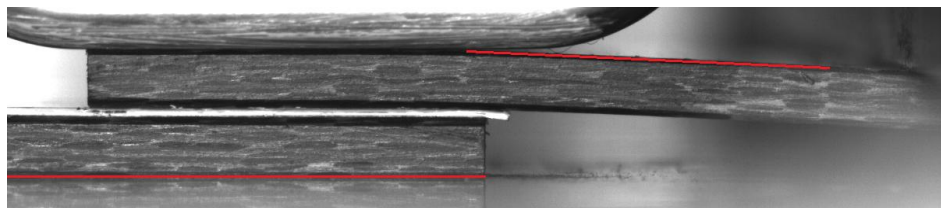


Figure 2: Side view of overlap with sonotrode applying the static force. Red lines indicate the two arms that compose the angle to be measured.

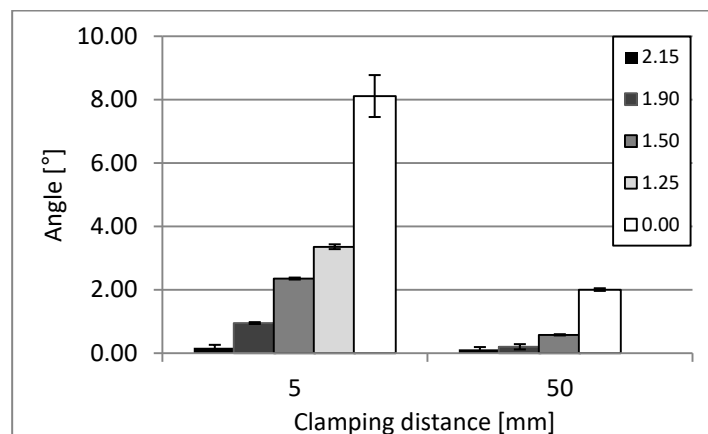


Figure 3: Angle between adherends versus clamping distance for different thicknesses of supporting base (2.15mm, 1.90mm, 1.50mm, 1.25mm, and 0.00mm) with 500N welding force being applied.

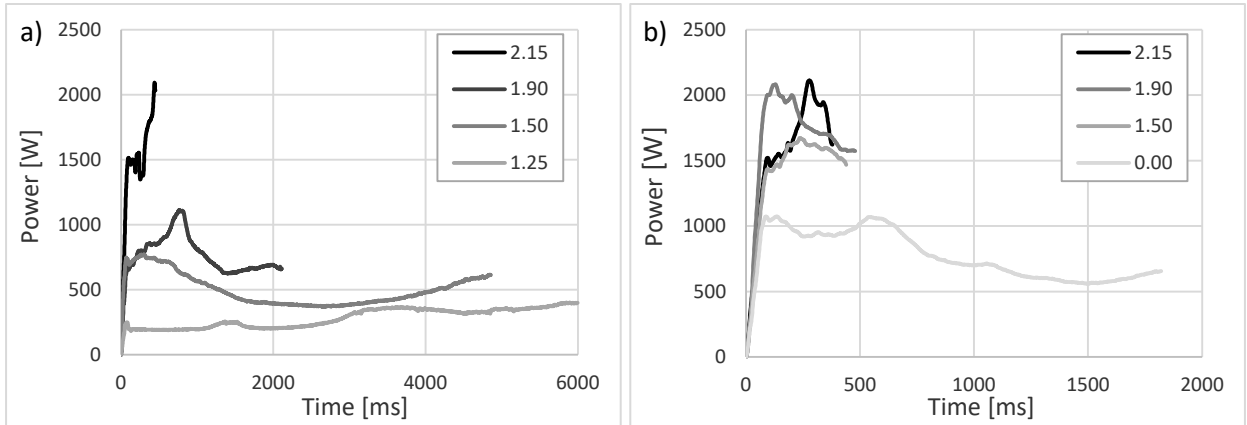


Figure 4: Power consumed until onset of flow for different supporting bases thicknesses and clamping distance of a) 5mm and b) 50mm.

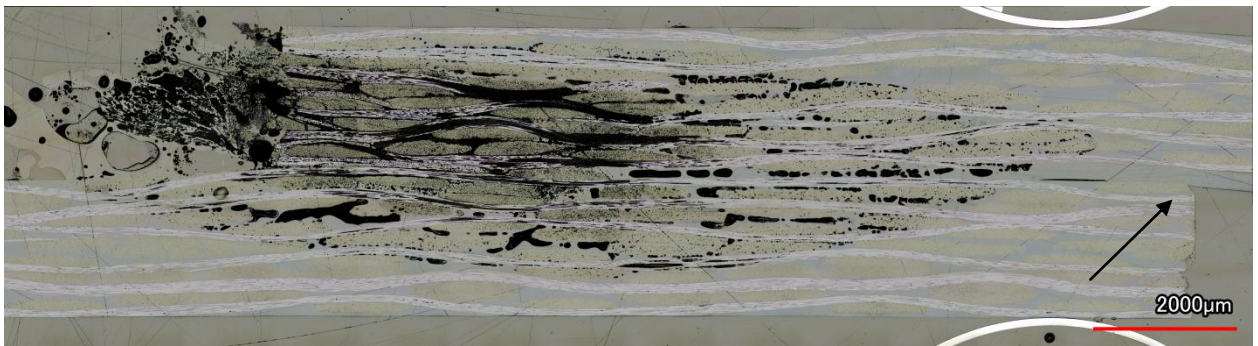


Figure 5: Cross-section microscopy of weld representative of case 1.25/5 stopped at the onset of flow (0.03mm). Black arrow indicates intact ED.

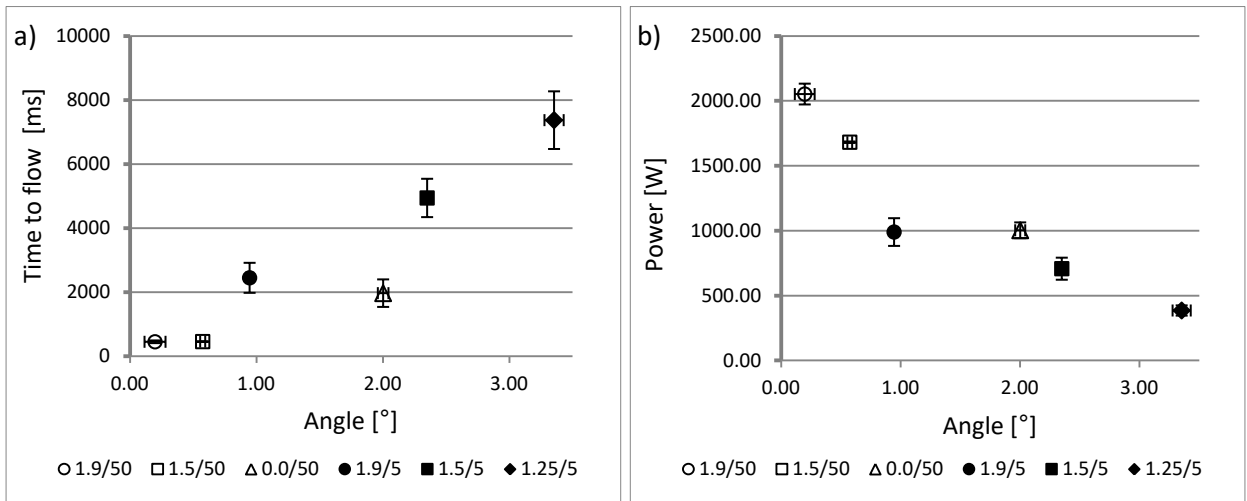


Figure 6: a) Time to flow and b) Power peak versus angle between adherends.

MULTIFUNCTIONAL FUSELAGE DEMONSTRATOR: THERMOPLASTIC COMPOSITE SKIN MANUFACTURING DEVELOPMENTS

EMUS 2020

W.M. VAN DEN BRINK⁽¹⁾, W.J. VANKAN⁽¹⁾, J. DE KRUIJK⁽¹⁾, S.L. VELDMAN⁽²⁾, R.
HERRMANN⁽³⁾

⁽¹⁾ Royal Netherlands Aerospace Centre (NLR), Anthony Fokkerweg 2, Amsterdam, The Netherlands,
Wouter.van.den.Brink@nlr.nl, Jos.Vankan@nlr.nl

⁽²⁾ GKN-Fokker, Industrieweg 4, Papendrecht, The Netherlands, Bas.Veldman@fokker.com,

⁽³⁾ Airbus Operations GmbH, Airbus allee 1, Bremen, Germany, Ralf.Herrmann@airbus.com

Key words: Computational Methods, Modular assembly, Innovative Manufacturing, Virtual Manufacturing Structure,

Abstract. Within Clean Sky 2 the design and manufacturing of the fuselage of new single aisle aircraft is investigated through a large, multi-functional fuselage demonstrator, see Figure 1. The main objectives of this demonstrator are to enable high production rates with a minimum of 60 aircraft per month and to reduce structural weight and recurring cost. The envisaged demonstrator shall validate high potential multi-functional combinations of airframe structures, systems, cargo and cabin technology concepts for the next generation fuselage and cabin, using advanced materials and innovative design principles.

One of the key innovations for the multi-functional fuselage demonstrator is the modular assembly of pre-equipped sub-assemblies, see reference [1] and [4]. To make a step in the design and manufacturing of such integrated multi-disciplinary fuselage sub-assemblies, including components of structures, systems, cabin and cargo, advanced materials and manufacturing methods are required. Thermoplastic composites and their highly automated fibre placement production techniques and advanced joining methods, offer the flexibility and efficiency that is needed for the production of much more pre-equipped sub-assemblies to enable the modular assembly process for the future aircraft production supply chain.

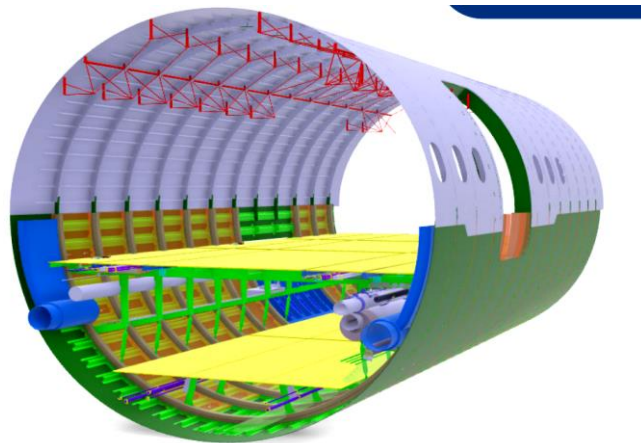


Figure 1: CAD model of the full fuselage.

This paper presents investigations on the development of several innovative manufacturing methods for the full-scale single aisle skin component for the lower fuselage. Because of the complexity of the considered multi-functional structures, the risk for manufacturing of the demonstrator and the level of detail that is required for the high level of manufacturing accuracy, detailed 3D modelling and analyses are necessary for predictions of the manufacturing processes. The results presented in the paper will include the modelling steps for manufacturing of the thermoplastic skin part from the laminate conversion from CAD (composite modeller) to automated fibre placement manufacturing simulation (explicit) and dynamic handling of the thin skin section and draping process (implicit and explicit simulations). The modelling results support the specification of manufacturing tools and processes, which are currently further developed.

1 INTRODUCTION

To deliver a double-digit fuel burn reduction for the Large Passenger Aircraft (LPA) segment next generation fuselage structure concepts are needed in which cabin, cargo and physical system elements are integrated. The three main overarching objectives for future fully equipped Single Aisle Aircraft fuselages compared to the state of the art are:

- Enable a High Rate Production (HRP) of minimum 60 shipsets per month
- Reduce a total fuselage weight by 10%
- Reduce the recurring cost by 20%

For this purpose a full scale fuselage section will be developed, manufactured and delivered as manufacturing demonstrator. The lower half of this section is 180° full scale multi-functional integrated thermoplastic fuselage shell, incl. cabin and cargo floor structure and relevant main interior and system elements. Advanced design principles, innovative system architecture, advanced materials and processes to generate high potential solutions for next generation fuselages will be used. One of these advanced design principles enabling the multifunctional structures is the use of virtual process technologies.

During the last five years the virtual process simulations using physical behaviour has received increased attention. The benefit of virtual process simulations are to gain insight in the behaviour and influence of process parameters, before the actual manufacturing, , thus reducing the risk by mitigating actions. Manufacturing experience, trials, and small size demonstrators can therefore be assisted by powerful simulation tools. A nice overview of virtual processing tools is shown in references [2], [3] and [5].

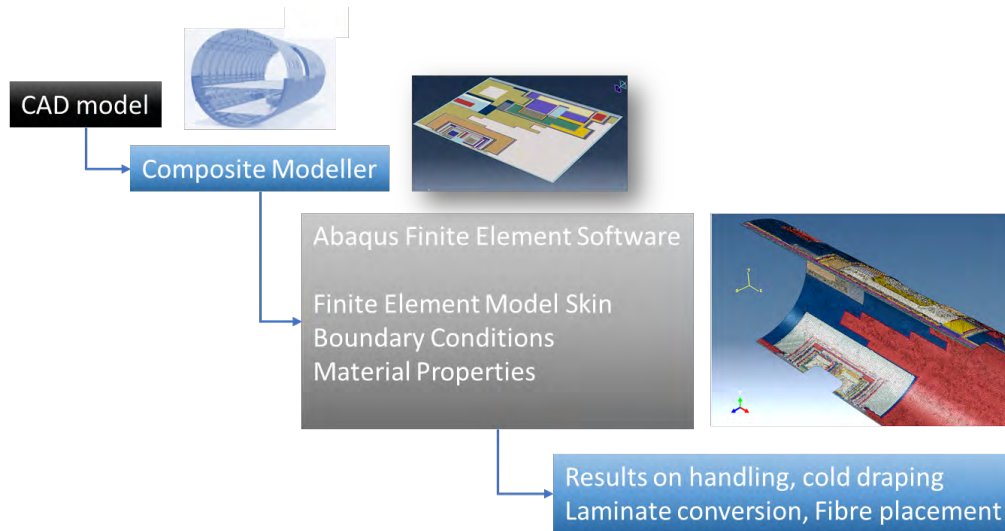


Figure 2: Workflow from CAD model to Finite Element Analyses results

Several innovative manufacturing methods for the full-scale single aisle fuselage skin component are investigated, see Figure 2. Because of the complexity of the considered large multi-functional structures, the risk for industrial manufacturing and for the manufacturing of the demonstrator, and the level of detail that is required for the high level of manufacturing accuracy, detailed 3D modelling and analyses are necessary for predictions of the manufacturing processes. The results presented in the paper will include the modelling steps for manufacturing of the thermoplastic skin part from the laminate conversion from CAD (composite modeller) to automated fibre placement manufacturing simulation (explicit) and dynamic handling of the thin skin section and draping process (implicit and explicit simulations).

2 METHODS AND MODELS

In this section of the paper the methods used to enable multifunctional structures will be presented. The topics are composite modeller, handling simulation and draping and fibre placement simulations.

2.1 Composite modeller

The composite skin consists of many layers and ply drops that are defined in the CAD files (Catia). Correct transfer of geometrical and composite data into the finite element software can be very challenging. Furthermore the detailed translation from the curved fuselage skin

defined in CAD to the flat skin model needed for the manufacturing simulation introduces additional challenges. Therefore the fibre orientation of the layer and normal directions of the laminate need to be accounted for. To perform this translation the composite modeller is used which has the beforementioned mapping with high accuracy. Composites Modeler for Abaqus/CAE extends the ply modelling features in Abaqus by providing fibre simulation capabilities.

2.2 Fibre placement simulation

The composite layer deposition is performed using a fibre placement machine, also known as advanced fibre placement AFP. To gain insight in the behaviour and dynamics of this production process a simulation using dynamic explicit is performed on the fibre placement. This approach allows for assessing the influence of tackiness to the mould, bending and cutting using material damage parameters of the composite fibres/tows. The virtual fibre placement head can deposit 8 composite tows simultaneously. In contrast to most AFP simulations this included the physical effects.

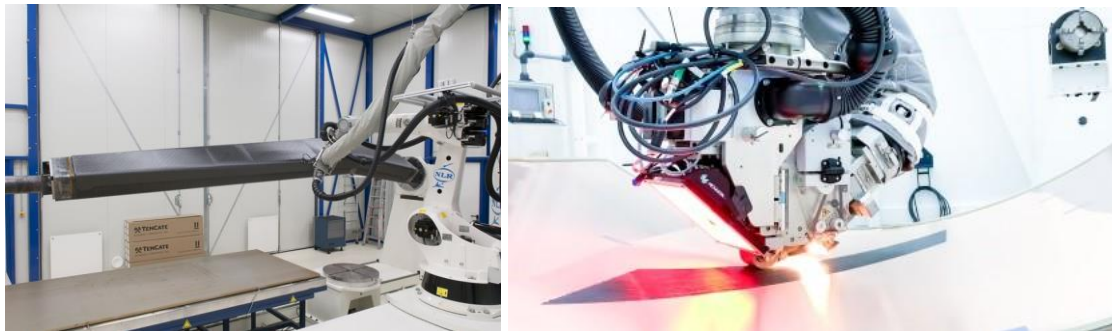


Figure 3: Fibre placement technology which is used for the manufacturing of the skin. [6, 7]

2.3 Handling simulation an Draping simulation

The manufacturing process foreseen for the large skin section includes the handling and draping of several sub-laminates into the consolidation mould. To gain insight in the dynamic behaviour of these quite large and thin and flexible skin sub-laminate structures, dynamic explicit simulations are performed. The skin is picked up using suction cups and then carefully placed into the curved mould.

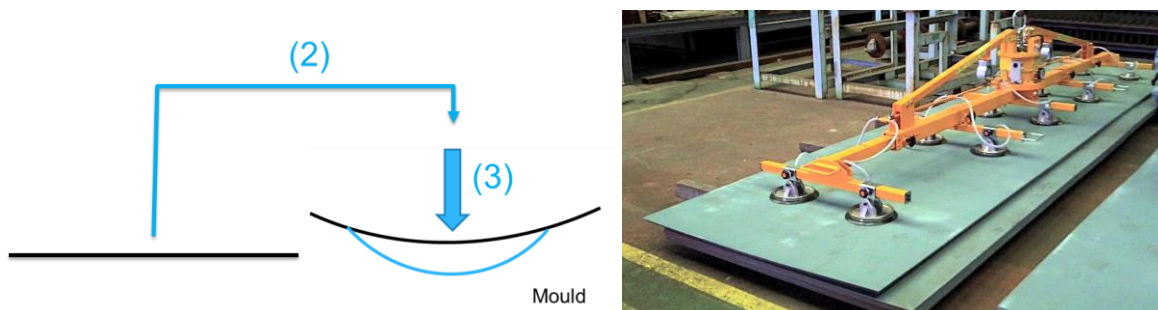


Figure 4: Schematic of the skin after fibre placement to the mould involving a shape transition from flat to curved and on the right an image of a vacuum lifting device [8]

The method used for modelling enables variation of laminate thickness, number of suction cups and their distribution over the skin. The main aim of these simulations is to analyse in detail behaviour of these large and thin laminates during the transition to avoid that the skin gets damaged during this transport to the mould. The requirements are set on maximum suction cup load is 200 N and interlaminar shear stress (ILSS) due to bending of the preform laminate of 6 MPa.

3 RESULTS

In this section the results for the several topics related to the manufacturing of the multifunctional fuselage demonstrator skin is discussed.

3.1 Composite modeller

As described in section 2.1 the composite modeller is used for creating the skin finite element model. The ply book design of the skin for the demonstrator contains over 120 detailed ply definitions. These definitions are active in different regions over the skin in order to create a balanced and as-designed skin. To do this manually would be too big an effort so therefore the composite modeller is used. This uses the CAD Catia file and Abaqus finite element mesh as input to map the laminate to the mesh. Two designs were made, a coarse design with 50.000 elements and one with 500.000 elements (S4R shells). For the second design also the mesh was more structured to enable correct mapping of the ramp zone details using elements with average size of 10 mm.

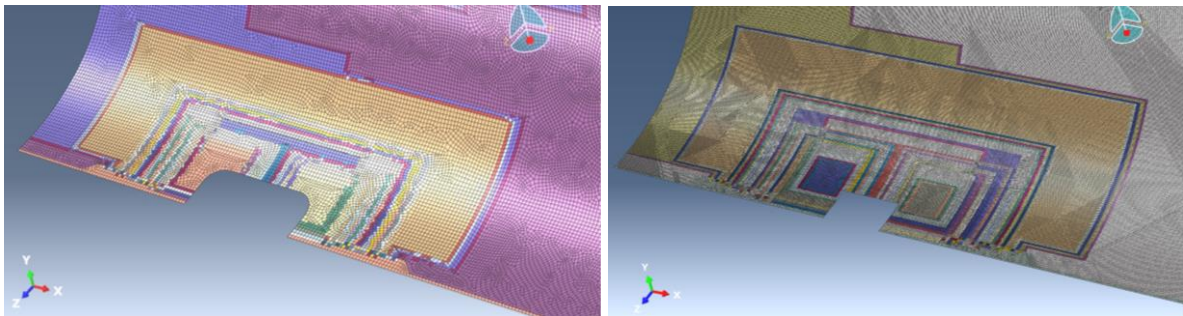


Figure 5: Composite modeller mapping of the skin

The mapping of the laminate from CAD to the finite element model was performed successfully. The overall computational performance proved to be challenging due to the large amount of ply definitions and sections. The result of the mapped finite element skin model was used for the handling and draping simulations described in section 3.3.

3.2 Fibre placement simulation

As described in section 2.2 the fibre placement simulation is used. For the manufacturing of the skin the fibre placement manufacturing is used. In order to gain understanding of the

process a simulation was created using Abaqus Explicit, so-called virtual FPM. This consists of the following parts, which are shown in see Figure 6: the metal mould (white), the fibre placement head and tow guides (blue), the individual tows (8 in total), cutting knives, roller (blue). The mould, cutting knives and fibre placement head are rigid parts. The carbon fibre reinforced plastic tows are elastic and have damage modelling and cohesive interaction (tack) with the mould. The roller is also elastic with rubber properties.

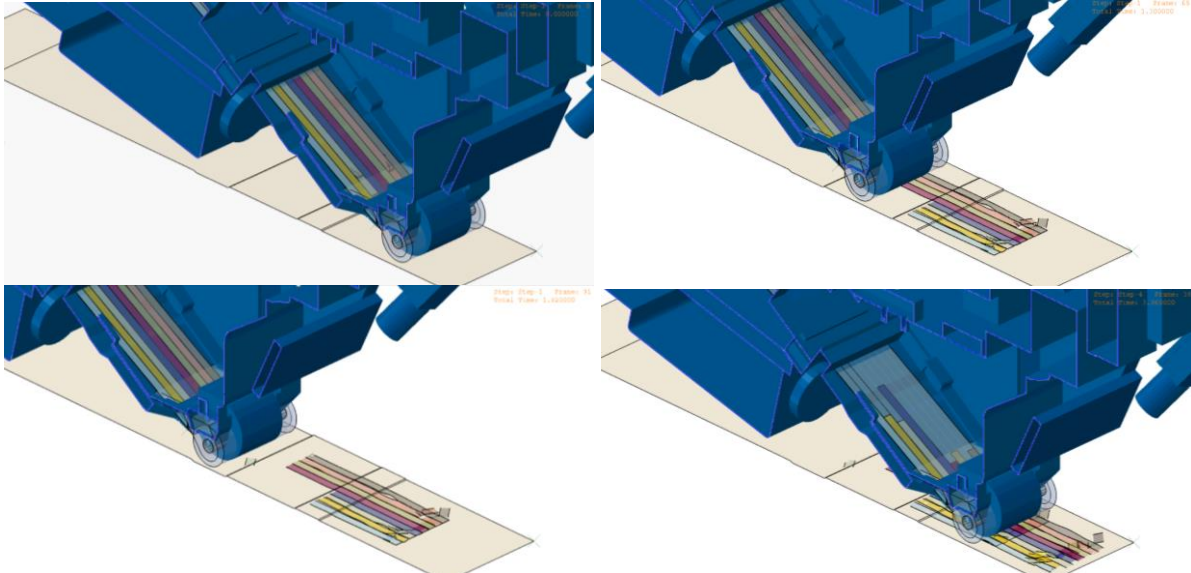


Figure 6: Fibre placement simulation (Virtual FPM)

The results of the simulation are shown Figure 6 where two layers are deposited using the intermediate cutting. The simulation results are satisfying in a qualitative respect with good correspondence with fibre placement tow behaviour in reality using visual comparison. The computational effort is significant with 2 hours of calculation time on 8 CPU's. It gives valuable insight in the sensitivities and speed of the process. The approach will be used for the skin to investigate challenging areas. At this point it is not feasible to have the entire skin part simulated using this approach because of computational limitation. Further work also involves the combination with thermal simulation and laser heating followed by a cooldown distortion simulation and validation using actual measurements.

3.3 Handling simulation and Draping simulation

As described in section 2.3 the manufacturing process foreseen for the large lower skin of the demonstrator includes several fibre placed sub-laminates, handling and draping into the consolidation mould, see Figure 7. Several models are created with different suction cup supports. The thinnest -and therefore the most flexible- skin sub-laminate is selected as worst case for the analyses and consists of 6 plies.

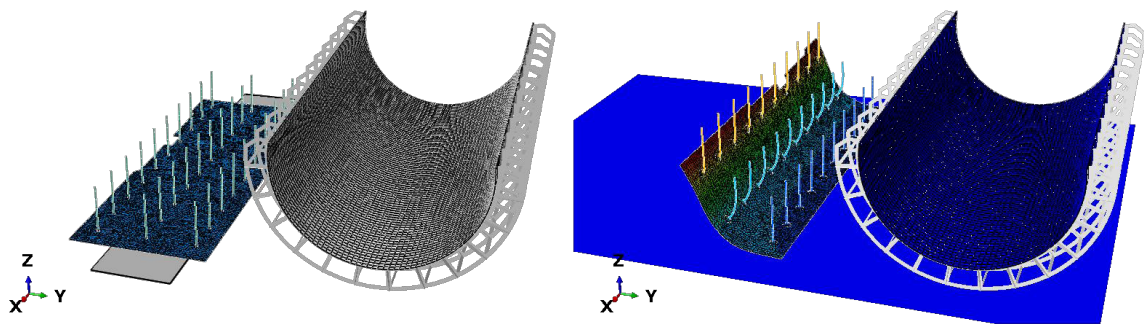


Figure 7: Model and result of the skin transport using suction cups. On the left in blue the flat placed skin and the curved mould. On the right the pick up of the flat skin using suction cups and chains towards the mould.

The dynamic handling and draping finite element simulation gives very good insight in the behaviour of the flexible thermoplastic skin. Too little supporting suction cups will give considerable bending and interlaminar shear stress, high suction cup loading and possible damage to the unconsolidated thermoplastic skin. A suction cup arrangement of 3 x 10 gives satisfactory results and normal and shear loading of the suction cups within the safety limits of 200 N loading. Also the bending is limited and shows low ILSS values of 1 – 2.4 MPa. This option is chosen for the manufacturing and transport process.

4 CONCLUSIONS AND RECOMMENDATIONS

In this paper the investigations on the development of several innovative manufacturing methods for the full-scale single aisle fuselage skin component are presented. The complexity of the envisaged multi-functional structures has benefits but also poses a risk for both the industrial manufacturing and the manufacturing of the demonstrator and increases the level of detail that is required for the high level of manufacturing accuracy. Therefore the detailed 3D modelling and analyses are necessary for risk-mitigating predictions of the manufacturing processes.

The presented modelling steps for manufacturing of the thermoplastic skin part are the laminate conversion from CAD (composite modeller), the fibre placement manufacturing simulation (explicit), and the dynamic handling of the thin skin section and draping process (implicit and explicit simulations). The simulation results have given valuable insight in the behaviour. This insight is used for improving the manufacturing of multi-functional structures and obtain first time right parts.

ACKNOWLEDGEMENT

This project has received funding from the Clean Sky 2 Joint Undertaking (JU) under grant agreements Nos 807097 and 945583. The JU receives support from the European Union's Horizon 2020 research and innovation programme and the Clean Sky 2 JU members other than the Union.

The work and support of C.P. Groenendijk from NLR is kindly acknowledged.

DISCLAIMER

The results, opinions, conclusions, etc. presented in this work are those of the author(s) only and do not necessarily represent the position of the JU; the JU is not responsible for any use made of the information contained herein.



REFERENCES

- [1] S.L. Veldman, P.J. Kortbeek, P.C. Wölcken, R. Herrmann, J. Kos, I. Fernandez Villegas, Development of a multifunctional fuselage demonstrator, Proceedings of Aerospace Europe Conference, Bordeaux, France, 25 February 2020 to 28 February 2020
- [2] D. Otten, T.A. Weber, J.C. Arent, Manufacturing Process Simulation – On Its Way to Industrial Application, International Journal of Aviation, Aeronautics, and Aerospace Volume 5 Issue 2
- [3] Dörr, Dominik & Brymerski, Wojciech & Ropers, Steffen & Leutz, D. & Joppich, T. & Kärger, Luise & Henning, Frank. (2017). A Benchmark Study of Finite Element Codes for Forming Simulation of Thermoplastic UD-Tapes. Procedia CIRP. 66. 101-106. 10.1016/j.procir.2017.03.223
- [4] W.M. van den Brink, J. Kos, W.J. Vankan, A.J. de Wit, Large carbon fibre reinforced thermoplastic fuselage manufacturing supported by virtual processing, NLR-TP-2020-393, 7th Aircraft Structural Design Conference, 2020
- [5] L. Paletti, W.M. van den Brink, Virtual manufacturing for composites, overview and status, Presented at the ISCM 2018, November 2018, Marknesse, Netherlands, NLR-TP-2019-367
- [6] Website: <https://www.compositesworld.com/articles/thermoplastic-composite-demonstrators-eu-roadmap-for-future-airframes->, G. Gardiner, Thermoplastic composite demonstrators - EU roadmap for future airframes
- [7] Website: <https://www.sucohs-project.eu/news/sucohs-newsletter-no-3>, SUCOHS EU project newsletter 3
- [8] Website: <https://www.vacuumlift.jp/eng/vac/m6075.html>, VD M-6075 Fukoku Corp. Japan

AUTHORS INDEX

Algermissen, S.	56, 68	Missinne, J.	74
Bisagni, C.	90	Otero, F.	29
Brito, C.B.G.	96	Řezníček, Z.	50
de Freitas, J.	35	Seo, J.-W.	84
de Kruijk, J.	102	Steege, S.	50
Dransfeld, C.	96	Teuwen, J.	96
Fernandez Villegas, I.	96	Tijs, B.H.A.H.	90
Herrmann, R.	102	Turon, F.	29
Heuts, C.	17, 43	van den Brink, W.M.	102
Homola, P.	35	van Dooren, K.S.	90
Hulzinga, A.	23	van Hengel, C.	17, 35, 43
Kim, M.-S.	84	van Steenberg, G.	74
Konter, Y.	17	Vankan, W.J.	102
Lansink Rotgerink, J.	43	Veldman, S.L.	102
Leiss, J.	23	Verpoorte, J.	17, 23, 43
Lungaho, V.	50	Voet, E.	74
Luyckx, G.	74	Vrchota, P.	50
Martinez, X.	29	Willemsen, M.	23
Martínez-Vázquez, M.	23, 50	Windels, J.	74
Misol, M.	56, 68		



Funded by the Horizon 2020
Framework Programme of the
European Union